Multilayer Energy Discriminating Detector for Medical X-ray Imaging Applications

by

Nicholas Allec

A thesis
presented to the University of Waterloo
in fulfillment of the
thesis requirement for the degree of
Doctor of Philosophy
in
Electrical and Computer Engineering

Waterloo, Ontario, Canada, 2012

I hereby declare that I am the sole author of this thesis. This is a true copy of the thesis, including any required final revisions, as accepted by my examiners.

I understand that my thesis may be made electronically available to the public.

Abstract

Contrast-enhanced mammography (CEM) relies on visualizing the growth of new blood vessels (i.e. tumor angiogenesis) to provide sufficient materials for cell proliferation during the development of cancer. Since cancers will accumulate an injected contrast agent more than other tissues, it is possible to use one of several methods to enhance the area of lesions in the x-ray image and remove the contrast of normal tissue. Large area flat panel detectors may be used for CEM wherein the subtraction of two acquired images is used to create the resulting enhanced image. There exist several methods to acquire the images to be subtracted, which include temporal subtraction (pre- and post-contrast images) and dual-energy subtraction (low- and high-energy images), however these methods suffer from artifacts due to patient motion between image acquisitions.

In this research the use of a multilayer flat panel detector is examined for CEM that is designed to acquire both (low- and high-energy) images simultaneously, thus avoiding motion artifacts in the resulting subtracted image. For comparison, a dual-energy technique prone to motion artifacts that uses a single-layer detector is also investigated. Both detectors are evaluated and optimized using amorphous selenium as the x-ray to charge conversion material, however the theoretical analysis could be extended to other conversion materials. Experimental results of single pixel prototypes of both multilayer and single-layer detectors are also discussed and compared to theoretical results. For a more comprehensive analysis, the motion artifacts present in dual-exposure techniques are modeled and the performance degradation due to motion artifacts is estimated. The effects of noise reduction techniques are also evaluated to determine potential image quality improvements in CEM images.

Acknowledgements

I would like to first thank my supervisor, Dr. Karim S. Karim, for his guidance, patience, and encouragement throughout my studies. I would also like to thank my STAR group colleagues for their help and companionship, namely, Shiva Abbaszadeh, Kai Wang, Feng Chen, Hadi Izadi, Michael Adachi, Amir Goldan, Nader Safavian, Mohammad Yeke Yazdandoost, Bahman Hadji, Dali Wu, Yuan Fang, Hasib Majid, Christos Hristovski, Kyung-Wook Shin, Umar Shafique, Chris Scott, Sina Ghanbarzadeh, Ryan Mann, and my office mate James *"Jimmy"* Ho. Also, thanks go out to the University of Waterloo ECE staff and my thesis committee members.

The help and guidance of Dr. John Lewin is acknowledged and greatly appreciated. Andre Fleck and Dr. Olivier Tousignant were instrumental in carrying out the experimental work and their help is greatly appreciated. Additional thanks go out to Dr. Erik Fredenberg and Dr. Ian Cunningham for fruitful discussions.

I would also like to thank the Natural Sciences and Engineering Research Council of Canada (NSERC), Waterloo Institute of Nanotechnology (WIN), Ontario Research Fund Research Excellence (ORF-RE), and the University of Waterloo.

Lastly, I would like to thank my family for their continuous support. Thanks to Leo, Theresa, Courtney, Matthew, and Ben. Finally, thanks to my wife, who has been a source of inspiration, for her kindness, encouragement, and support.

Contents

List of Tables

List of Figures

Chapter 1

Introduction

The uncontrolled proliferation of cancer cells can destroy adjacent tissues and may spread to different parts of the body. In order for the treatment of cancer to be effective, the detection process must have high sensitivity and specificity. There are several different methods for detecting cancer that typically depend on the type of cancer which is to be detected. In addition, several types of cancer have associated screening programs in which to detect cancer. These screening programs generally are desirable to have quick throughput as they are delivered to a large population.

A well known type of cancer with a well established screening program is breast cancer. Breast cancer is one of the most common cancers among women (excluding skin cancers) and the incidence generally increases with age [1]. This type of cancer takes the lives of approximately 40000 women per year in the United States, which is second only to lung cancer [1].

1.1 Breast cancer detection methods

Several methods may be used to detect cancer including (projection) x-ray imaging, magnetic resonance imaging (MRI), and computed tomography (CT). X-ray imaging modalities (including projection x-ray imaging and CT) are problematic due to the use of ionization radiation, which may itself cause secondary cancer to the exposed patient. It is desirable to keep the absorbed dose (energy absorbed per unit mass) of the patient as low as possible to minimize the chance of causing secondary cancer. In projection x-ray imaging, x-rays are directed towards the patient and a projection image is acquired from the x-rays which

reached the detector on the side of the patient opposite of the x-ray source. In spite of the potentially harmful radiation used in x-ray imaging, projection x-ray imaging is the method used for breast screening, as it has several advantages including (relatively) low cost (including operating cost) and (relatively) fast throughput. The projection image may be taken at several angles and the resulting images (e.g. 9-25) may be combined using computer algorithms to create a three-dimensional (3D) image [2]. This technique is known as tomosynthesis and can be carried out using a system similar to conventional mammography systems. It should be noted however that tomosynthesis is not a true 3D imaging technique since it does not allow for reformatting in all planes. In CT, projection images are taken at a large number of angles (effectively covering a 360 degree rotation around the imaged object) and the results are combined to create a three-dimensional image. CT is generally associated with high cost and high dose, however research is being carried out on a dedicated breast CT system [3].

Unlike projection x-ray and CT, MRI does not use ionizing radiation, instead it uses the excitation and relaxation of protons, and is thus considered safer, especially for frequent patient monitoring. MRI is a powerful tool for distinguishing soft tissues from each other however the resolution is somewhat limited (e.g. $\sim$1mm) and the scan times can be considerably long. MRI for breast cancer imaging typically requires an intravenously injected gadolinium contrast. In addition to the methods listed above, another alternative is positron emission tomography (PET) where a tracer is injected into the body which emits positrons that locally interact with the medium and emit gamma rays (high energy electromagnetic radiation produced by the annihilation of an electron and a positron). This type of imaging is good for determining the extent of metastases (the spread of the cancer) and there has been some work on PET being applied to a dedicated breast scanner [4], however PET has limited spatial resolution (e.g. $\sim$1mm) and is not a widely available alternative. Other examples of detection methods for breast cancer include infrared mammography and ultrasound.

One of the problems with x-ray imaging of the breast is the anatomical noise, which is due to the spatial variation of breast tissue (both fat and fibrous, or glandular, tissue). This spatial tissue variation makes it difficult to detect tumors within the breast, especially for patients with dense breasts. Approximately 20% of invasive breast cancers are missed using standard mammography [5]. A known method to enhance the tumors by reducing the appearance of the spatial tissue variation uses multiple images of the breast and an injected contrast agent.

Contrast-enhanced mammography (CEM) is a method of breast angiography (technique for visualizing blood vessels) where a contrast media is intravenously injected into a patient to enhance the acquired image. This technique relies on the growth of new blood vessels

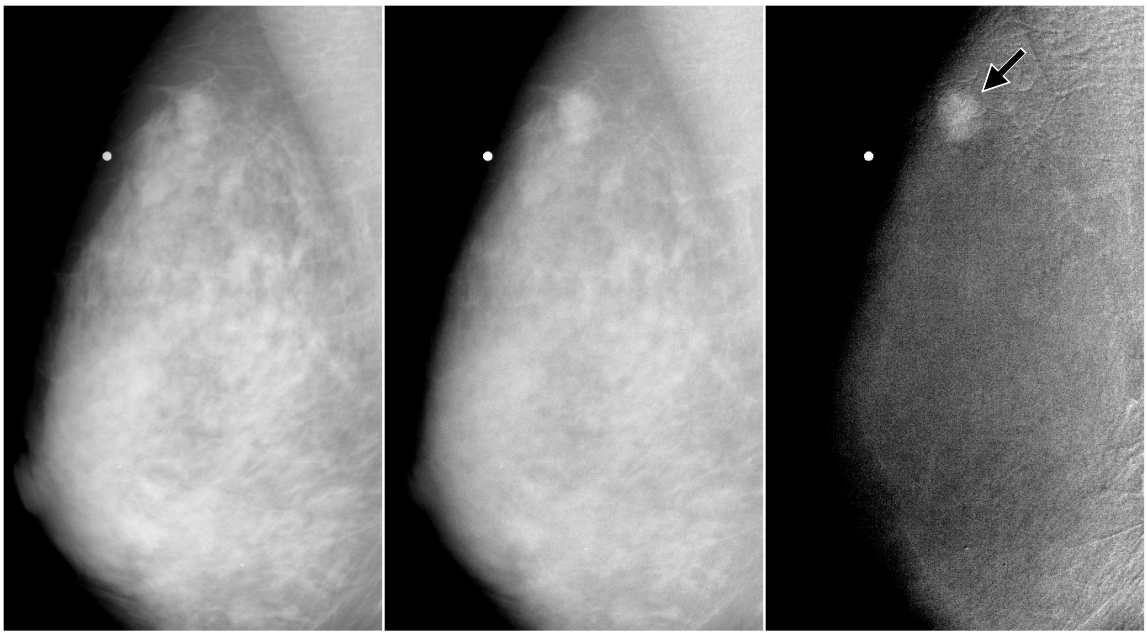

Figure 1.1: Low-energy (left), high-energy (centre), and combined dual-energy CEM (right) images. White, circular object in top-left of images is a metal marker bead. Arrow indicates enhanced lesion. Raw image data courtesy of Dr. John M. Lewin.

(i.e. tumor angiogenesis) during the development of cancer [6]. The growth accompanies an increase in tumor cell population to provide sufficient materials for cell proliferation. Since cancers will accumulate an injected contrast agent more than other tissues, it is possible to enhance the area of lesions and remove the contrast of the normal tissue. Lesions may be identified from contrast uptake and elimination rate (washout) due to the leaky abnormal vasculature associated with tumors. Using one of several techniques [7, 8, 9, 10, 11, 12, 13, 14, 15, 16, 17, 18], two (or more) images are taken, which are affected differently by the uptake of the contrast agent. By combining the two images, the background tissue is removed from the image while the area of lesion is enhanced (see Fig. 1.1). Several methods of image combination, such as subtraction, have been studied to aid in the removal of background tissue [19, 20, 21, 22].

CEM is used to aid in the visualization of cancers that may be difficult to identify using standard digital mammography (DM) [11], for example in high density breasts [6], and may be used to improve location and size assessments of lesions, which helps better plan surgery and treatment. This technique has the advantage of being able to detect the angiogenesis induced by cancers which otherwise would be difficult to detect on con-

ventional mammograms [23]. It is also thought that the use of CEM will help in the monitoring and treatment of breast cancer [24], the reduction of false biopsies, and clearer delineation of tumors [25]. CEM also has the potential application of monitoring the response to chemotherapy and detecting recurrences [23]. An estimate of 10% of women are recalled for additional testing after screening mammography. About 15% of the recalled women then undergo needle core biopsy and only 30% of these biopsies show malignant tumors [26]. Since biopsies are costly, invasive, and cause stress and anxiety for patients, it is desirable to not only confirm the cases where cancer is present, but also confirm at an earlier stage whether cancer is not present, which is a potential application of CEM.

MRI can also use the property of tumor angiogenesis to reveal cancers [6]. The benefit of x-ray based CEM is that it is significantly less costly compared to MRI, since CEM can be carried out in DM units, which are widely available [25]. Generally MRI units are more expensive to purchase and operate compared to DM units [11], with approximately 10 times the cost of mammography [5], and are more time consuming. In addition, DM units can provide greater spatial resolution compared to MRI [24].

Besides using MRI and DM units for CEM breast imaging, CT was also examined as a candidate [27]. The use of CT for CEM showed promising results except that it is associated with high radiation dose and marginal spatial resolution [28]. Tomosynthesis units may also be used to carry out CEM and provide a 3D CEM image [29].

Several different techniques to acquire the CEM images have been examined in the past using projection x-ray imaging. Temporal subtraction and dual-energy subtraction methods use images taken at different points in time to recreate the final image [30]. Both of these methods can be carried out in conventional DM units with few modifications. The drawback of these methods is that they use two exposures and thus suffer from motion artifacts in the subtracted image due to patient movement.

Other methods for carrying out CEM involve using a single exposure and discriminating the energy spectrum of the beam to create two images. Using a single exposure has the advantage of reducing motion artifacts since both images are acquired simultaneously. For example when using a single-exposure dual-energy system in chest imaging, there is no need for cardiac gating (for image synchronization) [31]. Energy discrimination may be achieved using a photon counting detector (e.g. [16]) or a multilayer detector. The use of multilayer detectors (or stacked phosphor detectors) for single-exposure energy discrimination has been leveraged for CT [32, 33] chest radiography [34], security applications [35], portal imaging [36], and microcalcification identification [37, 38], however its use for CEM has yet to be rigorously explored.

1.2 Thesis organization

The main focus of this thesis is to analyze and optimize a multilayer detector for CEM. A single-layer detector is also analyzed and optimized for comparison purposes.

Chapter 2 discusses background topics relevant to the research project. X-ray detection methods are discussed and relevant performance metrics are presented.

Chapter 3 discusses previous methods used to carry out CEM. These methods differ in the manner the images to be combined are acquired. The images are acquired either using a single exposure or two exposures. The previous use of multilayer detectors made of film-screen sets or computed radiography plates in other applications is also discussed.

Chapter 4 presents the project description and contributions. The overall multilayer and single-layer detector structures are also discussed.

Chapter 5 discusses the theoretical models used to optimize the single-layer and multilayer detector for CEM. Two cascaded detector models are presented, one evaluated at zero spatial frequency and the other evaluated as a function of spatial frequency. Details regarding the calculation of the mean glandular dose, the x-ray tube spectra, and performance metrics are also discussed. Results from the theoretical models are presented and the performance of the optimized single-layer and multilayer detectors is compared.

Chapter 6 presents the experimental results of prototype single-pixel single-layer and multilayer detectors. The experimental results are used for verification of the models developed in Chapter 5.

Chapter 7 discusses the effect of motion on dual-energy dual-exposure CEM image noise and performance. A model is developed and implemented as an extension of the cascaded systems model presented in Chapter 5 to include the effect of object motion between low- and high-energy exposures. The noise power spectrum of clinical images from a dual-energy clinical study is used for model verification. The impact of motion artifacts on performance is quantified for a fairer comparison of single-exposure and dual-exposure CEM technologies.

Chapter 8 discusses noise reduction techniques and their potential benefit. A model is presented, which takes into account anatomical noise when evaluating noise reduction techniques for more accurate noise and performance improvement estimations. Clinical images are used for model comparison and noise reduction techniques are applied to both single-layer and multilayer detectors.

Chapter 9 concludes this research and summarizes the contributions of the project to the field of medical imaging. Suggestions for future work are also discussed.

Chapter 2

Background

2.1 X-ray generation

Electromagnetic waves with a wavelength of approximately 0.01 to 10 nm are considered to be x-rays. X-rays may be produced by several means however in medical imaging applications x-rays are typically produced by accelerating electrons towards a metal target in a vacuum environment (see Fig. 2.1).

The electrons may be boiled off a tungsten filament (cathode) and accelerated by the difference in potential between the cathode and anode. These electrons then hit the metal anode and interact with the metal to generate x-rays. Due to the inefficient process of generating x-rays (e.g. more than 99% of the incident energy leads to heat at diagnostic tube potentials [39]) the heating of the anode becomes a problem. To avoid the anode from melting, high melting temperature metals are used for the anode material and the anode may be rotated during operation. Typical anode (or target) materials include tungsten (W), molybdenum (Mo), and rhodium (Rh).

The tube potential is typically expressed using the kilovolt peak (kVp) unit. The peak tube potential gives an indication of the highest possible energy of the x-rays generated by the electron beam (i.e. the highest possible energy of an x-ray generated by an electron beam is the kinetic energy of the accelerated electron). Thus a tube at a potential of 100kVp, for example, may generate x-ray photons with a maximum energy of 100keV.

The spectrum of x-rays which is generated by the impinging electrons on a target material is composed of the contribution due to two different types of radiation, known as characteristic radiation and bremsstrahlung.

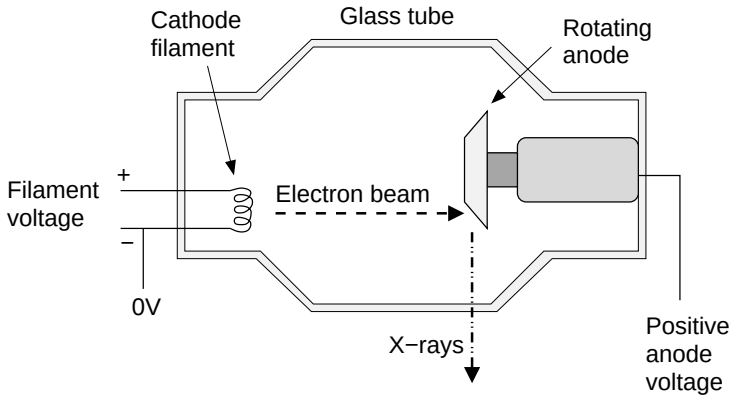

Figure 2.1: Simplified structure of a typical x-ray tube.

2.1.1 Characteristic radiation

Characteristic radiation, later referred to as fluorescent x-rays, is caused by the filling of an inner unfilled electron shell from an electron of a more outer shell. When an impinging electron has sufficient energy it may knock out a bound electron from an inner shell (e.g. the inner most shell, the K shell). An electron in a more outer shell (e.g. the L shell) will then fill the vacancy left by the ejected electron. By filling the vacancy the atom has reduced its energy by the change in the binding energy of the two shells involved in the process. This energy may be emitted as electromagnetic radiation (see Fig. 2.2). For inner shells such as the K and L shells the wavelengths of the electromagnetic radiation may fall in the range of x-rays. For example, the characteristic radiation from the filling of a vacancy in the K shell from an L shell is approximately 17.4keV for molybdenum and 58keV for tungsten [40].

Due to the discrete nature of electron shell energies, characteristic radiation occurs at discrete energy levels. Since the atomic energy levels are unique to each atom, the spectra generated from different target materials will differ, and the spectra due to this type of radiation is characteristic of the target atom.

2.1.2 Bremsstrahlung

Bremsstrahlung (German for braking radiation) is produced when the incident electron travels near the nucleus of an atom and is attracted by Coulombic forces which decelerate the electron (see Fig. 2.2). The change (loss) in energy of the traveling electron is the

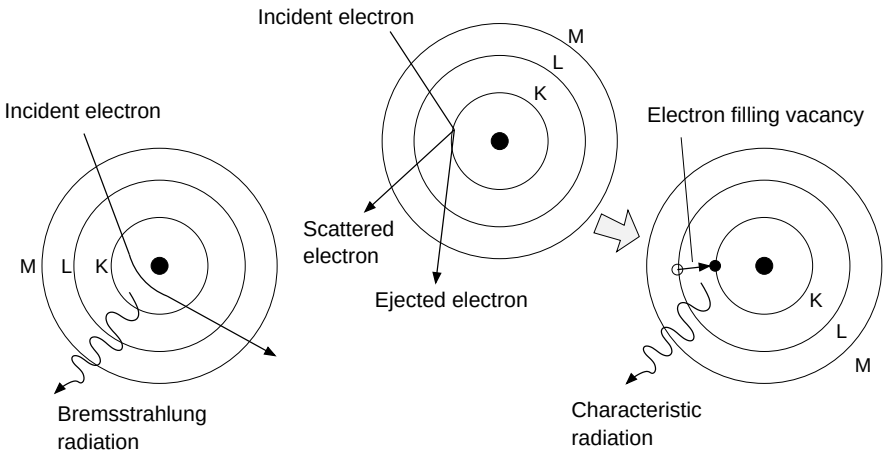

Figure 2.2: Simplified atomic-level depictions of the processes involved in generating bremsstrahlung (left atom) and characteristic radiation (two rightmost depictions). The shell identifiers are marked by K, L, and M.

energy of the radiation emitted. This type of radiation creates a continuous distribution of x-rays with a maximum energy which corresponds to the tube voltage which accelerates the electrons.

Fig. 2.3 shows the x-ray spectrum of a molybdenum target. Note that contributions from both characteristic and bremsstrahlung are visible.

2.2 X-ray attenuation

The attenuation of incident x-rays by different materials is an important factor to consider in medical imaging since in x-ray imaging it is the spatial variation in attenuation which is essentially measured by the detector and which provides the contrast in the image. For example, if we consider a chest x-ray, the dark area of the image representing the lungs is the area of the detector which receives the most x-rays as the lungs do not significantly attenuate the x-rays. On the other hand, the white area of the image represents the ribs, which significantly attenuate the x-rays. This property of x-ray imaging can be disadvantageous for imaging tissues with similar attenuation properties, such as the soft tissues in the brain.

There are several possible interactions that may occur when incident x-rays are attenuated by a material. These interactions are namely the photoelectric effect, Compton

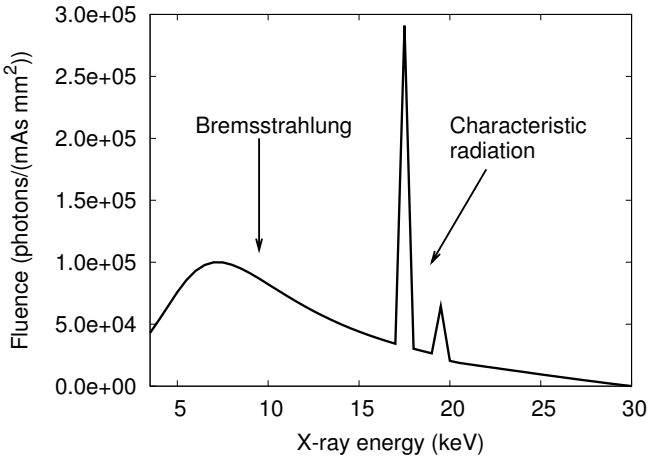

Figure 2.3: X-ray spectra from a 30kVp x-ray tube with a molybdenum target. The unit mAs refers to the tube loading which is obtained by multiplying the tube current (mA) by the exposure time (s). Spectra was generated using [41].

scattering, Rayleigh scattering, and pair production. The significance of these interactions varies with x-ray energy.

Pair production refers to the case when an incident x-ray creates an electron-positron pair in the material. Since this interaction creates an electron and a positron, an incident x-ray energy of $2m_ec^2$ (1.022MeV) is required, where m_e refers to the mass of an electron at rest. Since pair production is only a factor at very high x-ray energies (outside of the range considered for mammography) it will not be discussed further.

Rayleigh scattering is coherent scattering where the x-ray interacts with an atom however the energy of the atom and the scattered x-ray remains unaltered. This type of scattering is typically only a minor contributor to the overall attenuation of x-rays. For Compton scattering (incoherent scattering), the x-ray interacts with an electron and ejects the electron from its shell, in the process losing a fraction of its initial energy. The x-ray continues to propagate through the material however its directional path has been altered. Generally, scattering can lead to noisy images and is thus undesirable for medical imaging.

The photoelectric effect occurs when the incident x-ray ionizes an atom by transferring all of its energy to a bound inner shell electron. The energy of the ejected electron (secondary electron) then becomes equal to the energy of the incident x-ray minus the binding energy of the electron. A more-outer shell electron may fill the vacancy of the inner shell and generate a characteristic x-ray which may or may not be subsequently attenuated by

the same material which attenuated the incident x-ray.

The photoelectric effect is of importance due to its significance at relatively low energies which are used for medical imaging. It is this effect which leads to the generation of collectable charges in direct detectors, which will be further discussed in the next section.

2.2.1 Attenuation coefficient

The attenuation of x-rays by a material having thickness L can be summarized by the following relation:

$$I(E) = I_0(E) \exp(-\alpha(E)L) \tag{2.1}$$

where I is the intensity of the x-rays exiting the medium, I_0 is the intensity of the incident x-rays, α is the attenuation coefficient which is equal to the fraction of x-rays that interact per unit thickness, and E denotes the x-ray energy of the corresponding parameters. The attenuation coefficient takes into account the contribution of all the different interaction processes mentioned above where the interaction probability is proportional to the sum of the attenuation coefficients [39]:

$$\alpha(E) = \tau_{\mathrm{pe}}(E) + \sigma_{\mathrm{R}}(E) + \sigma_{\mathrm{C}}(E) + \kappa_{\mathrm{pp}}(E) \tag{2.2}$$

where the terms on the right-hand side refer to the attenuation coefficients of the photoelectric effect, Rayleigh scattering, Compton scattering, and pair production respectively.

The energy dependence of the different interaction types is shown in Fig. 2.4 for selenium. In this figure the significant energy dependence of the photoelectric effect attenuation coefficient can be seen ($\sim E^{-3}$). Also of note is the sharp increase in the attenuation coefficient at the K-edge, which is indicated in the figure (at 12.658keV for selenium [42]). This sharp increase occurs at the binding energy of the K shell since at this energy the x-ray has sufficient energy to eject an electron from the K shell. The addition of this interaction leads to an increase in the attenuation coefficient. Similar increases in attenuation coefficients can occur for the other shells however these increases may be less pronounced or may be of little interest if they occur at very small energies. The abrupt shift in attenuation coefficient of an element can be used in dual-energy imaging since the element will attenuate x-rays with energy higher than the K-edge more than it will attenuate x-rays with energy lower than the K-edge (assuming that both these energies are relatively close to the K-edge).

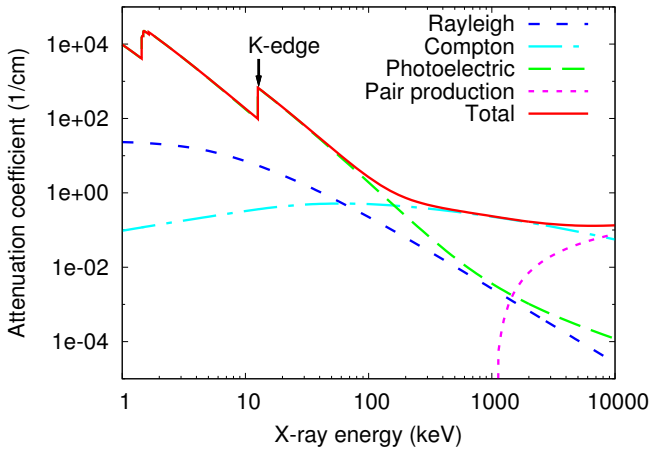

Figure 2.4: Attenuation coefficients in selenium for the different interaction types as a function of x-ray energy. Attenuation coefficients were taken from [43].

2.2.2 Filtration

An x-ray beam may be attenuated intentionally by a material to "shape" the spectrum into a more desirable form. This process is called filtering the beam. A filter, which can be in the form of a thin sheet of metal, is placed between the x-ray beam and the patient (or object of interest). The filter, not to be confused with an image processing filter, can be used to attenuate low energy x-rays to reduce the dose (absorbed energy per unit mass) to the patient/object. The filter hardens the beam, that is to say the spectrum has more emphasis placed on higher energy x-rays as they are absorbed the least (due to the inversely proportional relation of the x-ray energy on the photoelectric effect). Low energy x-rays which are not expected to reach the detector due to complete absorption (or nearly complete) by the patient/object are of no use for imaging and may cause harmful damage to the patient/object. Since in medical imaging it is important to keep the dose to as low as reasonably achievable it is favorable to minimize unnecessary dose.

2.3 X-ray detection methods

A common method for x-ray imaging is to use a photosensitive film coupled to a phosphor screen. The phosphor converts incident x-rays into optical light that alter the properties of the photosensitive film, which is developed in a chemical solution to provide the film in

its final form. This method is relatively simple however it has several problems which are summarized below:

- Storage is bulky
- Information retrieval and transfer is time consuming
- Image processing is not practical
- Real-time imaging is not possible

With the advent of readily available large area electronics it became possible to acquire digital images from the detector, which addresses several of the issues associated with film technology. In these detectors, x-rays are converted to collectable charges either directly (direct detection) or indirectly (indirect detection) through an intermediate conversion process where the x-rays are first converted to visible light.

2.3.1 Direct and indirect detection methods

Indirect detectors use a phosphor (e.g. thallium doped or sodium doped CsI, CsI:Tl, and CsI:Na, respectively) coupled to a photodetector array (e.g. amorphous silicon *p*-*i*-*n* photodiodes [44, 45], silicon charge-coupled devices [46], and amorphous selenium lateral [47, 48] and vertical [49] photodetectors). The phosphor converts the x-rays to isotropically emitted optical photons which pass through the phosphor and can be detected by the underlying photodetectors as shown in Fig. 2.5. The electrical signal acquired by the photodetectors can then be read out to acquire the image. For direct detectors, the x-rays are converted to multiple electron-hole pairs through the loss of energy of an energetic electron that was ejected (by the photoelectric effect) from the inner shell of an atom. These charge carriers are collected with the use of an applied bias across the photoconductor (e.g. amorphous selenium) as shown in Fig. 2.5. Although the typical configuration of the direct detector is that shown in Fig. 2.5 (vertical structure), lateral [50] and three-terminal [51] structures have also been investigated.

One of the disadvantages of indirect detection is that the spreading of the optical photons within the phosphor limits the resolution achievable. To reduce the effect of spreading it is possible to decrease the phosphor thickness, however at the cost of lower detection efficiency (since more x-rays will penetrate the detector without being attenuated by the phosphor). Direct detectors are not faced with such a problem since the electron-hole pair cloud produced by the energetic electron is relatively small (for x-ray energies

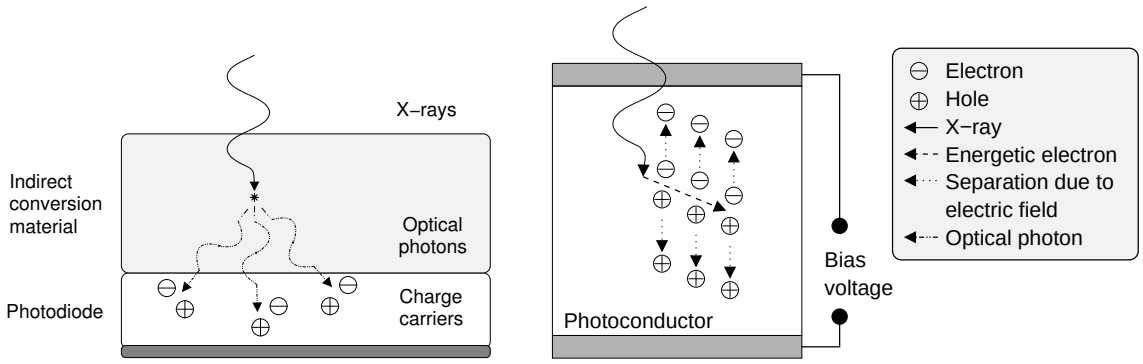

Figure 2.5: X-ray digital detection methods: indirect detection (left) and direct detection (right).

Table 2.1: Several photoconductor properties for direct detection [43, 52].

Photoconductor	Absorption depth at 30keV (μm)	$W_{\pm}$ (eV)	Resistivity (Ωcm)	Electron $\mu_e\tau_e$ (cm^2/Vs)	Hole $\mu_h\tau_h$ (cm^2/Vs)
a-Se	149	45[a]	10^{14}-10^{15}	$0.3\times10^{-6}-10^{-5}$	$10^{-6}-6\times10^{-5}$
HgI_2	91	5	4×10^{13}	$10^{-5}-10^{-4}$	10^{-6}
CdZnTe	81	5	10^{11}	2×10^{-4}	3×10^{-6}
PbI_2	137	5	10^{11}-10^{12}	7×10^{-8}	2×10^{-6}

[a]At an applied field of 10V/μm

of interest in medical imaging) and the bias voltage separates the charges in a direction normal to the electrode surface. Thus the resolution of direct detectors may be greater than that of indirect detectors, at the cost of a high voltage bias.

There are several different photoconductors that have been investigated for direct conversion detection. The properties of several photoconductors are summarized in Table 2.1 (where a-Se refers to amorphous selenium). The absorption depth, which is the depth at which the incident x-ray intensity has decreased to $\sim 36\%$ of its incident value, is given by the inverse of the attenuation coefficient. The higher the absorption depth, the further the x-rays may penetrate. To be able to stop all the incident x-rays and to be able to keep the detector thickness relatively thin, it is desirable for the absorption depth to be small. The second property in the table is the energy required to create a detectable electron-hole pair, $W_{\pm}$. It is desirable for $W_{\pm}$ to be low so that a higher fraction of the energy of an incident x-ray can be converted to collectable charge.

The resistivity of the material is also shown. Higher resistive materials lead to lower dark current, which is desirable. The $\mu\tau$ product is also given for both electrons and holes where μ and τ refer to the carrier mobility and lifetime, respectively. When this parameter is multiplied by the applied electric field, the mean range carriers will travel is obtained. It is desirable for this product to be high to assure that all carriers will be collected and not get trapped within the detector.

Although a-Se has a high $W_{\pm}$, its very high resistivity and capability of being deposited over large areas makes it a good candidate for large area direct x-ray detectors. However, due to its large absorption depth, it is limited to relatively low x-ray energies, such as those used for mammography. Though not discussed above, silicon is also used as a direct conversion photoconductor [53, 54].

2.3.2 Energy integrating and photon counting

The method used to acquire the x-ray signal with digital x-ray imagers can be divided into two categories: energy integrating and photon counting. Each method has its own corresponding set of electronics for signal readout and processing, however the x-ray conversion process, whether it be by indirect or direct conversion, is the same.

The readout circuit of an energy integrating detector is summarized in Fig. 2.6 for an a-Se detector. Though various pixel circuit architectures have been investigated, for example to improve long-term stability issues [55], the simplest configuration is shown here (passive pixel sensor). The charge generated by the interaction of the x-ray photon with the conversion material is swept to the collecting electrode due to the application of the electric field. The charge is stored on the storage capacitor, C_{st}, over a given period of time (the integration time). The stored charge is transferred from the pixel to the external circuit, consisting of a charge amplifier, through a read amorphous silicon thin-film transistor. The analog signal is then converted to a digital value using an analog-to-digital converter (not shown). The final signal represents the sum of the collected charge generated by all x-ray photons that interacted within the integration time.

A block diagram for a photon counting detector is shown in Fig. 2.7. The charge produced by the interaction of a single x-ray photon (or optical photons in the case of indirect detectors) generates a current pulse. This narrow pulse is passed through a pulse shaper to convert it to a broader pulse with a rounded peak to measure the amplitude with more precision. A comparator is used to determine if the pulse height is above some threshold and should be counted. If the pulse is within the desired (x-ray) energy window, it is counted. The desired pulse height thresholds can be determined using the

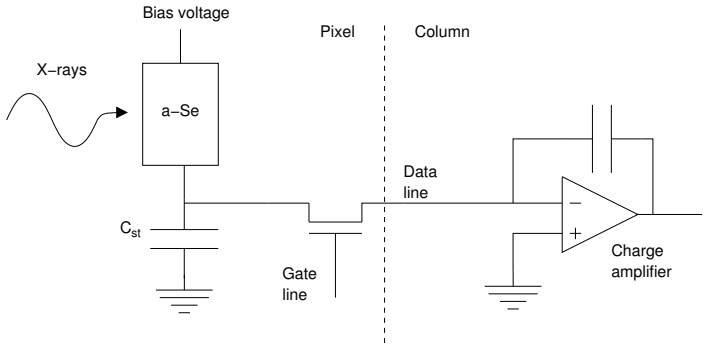

Figure 2.6: PPS circuit architecture configured for an a-Se photoconductor [56].

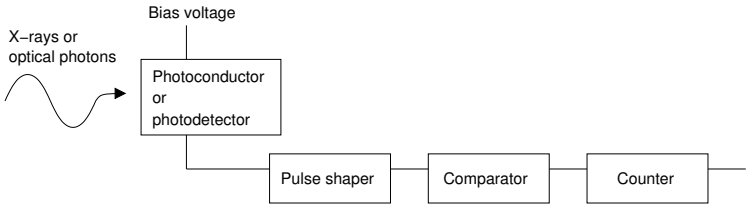

Figure 2.7: Block diagram for photon counter [57].

energies in the given x-ray spectrum and the conversion gain of the detector. By using multiple thresholds and keeping track of the total number of counted x-ray photons within each energy window, a histogram of the number of photons as a function of energy can be plotted for each pixel. To assure that current pulses from the interaction of two or more independent x-ray photons do not overlap, the incident x-ray photon rate must be controlled and kept to a relatively low value. Due to the added complexity required for the counting circuits of photon counters, it is difficult to achieve large area photon counting detectors with small pixel sizes (such as those required for mammography). Instead of large area detectors, a strategy using a slot scanned detector (i.e., a small detector array that is scanned across the width of the object) has been investigated [53]. Because of its ease of fabrication and since it is currently readily available as a full field large area imager, an energy integrating detector is considered for the current study.

2.4 Dual-energy imaging

Using different x-ray energies for obtaining tissue information was proposed by Jacobson [58]. Dual-energy imaging, discussed by Alvarez and Macovski [7], is a method of imaging that combines low-energy (LE) and high-energy (HE) images to create a third, enhanced image. It is also sometimes customary to generate a fourth image (using different combination parameters), such as in chest imaging (soft-tissue and bone-only images) [21]. There are several ways to combine the LE and HE images [19, 20, 21, 22]. The simplest is weighted logarithmic subtraction. Although this method is simple, it is quite effective and its performance is comparable to that of alternative methods [21].

The method will be demonstrated considering a case as in Fig. 2.8 where there are two monoenergetic incident exposures, one with low energy E_{L}, and the other with high energy E_{H}. To cancel out the image background it is desirable to eliminate the contrast between the adipose (fat) and glandular tissues in the object. The signal from x-rays passing through only the adipose region and the adipose plus glandular region are given by:

$$I_{i,a} = I_{i,0} G(E_i) e^{-\alpha_a(E_i) t} \tag{2.3}$$

$$I_{i,ag} = I_{i,0} G(E_i) e^{-\alpha_a(E_i)(t-t_g) - \alpha_g(E_i) t_g} \tag{2.4}$$

where I_0 is the number of photons per unit area incident on the object, G is the energy dependent gain of the detector and the subscript $i = \mathrm{L}, \mathrm{H}$ representing the different energy exposures. Using the weighted logarithmic subtraction method, the combined, dual-energy image is:

$$I_{\mathrm{DE}} = \ln I_{\mathrm{H}} - w \ln I_{\mathrm{L}} \tag{2.5}$$

where w is the weight factor. For the two cases considered (a and ag), the values of the dual-energy image are:

$$\begin{aligned} I_{\mathrm{DE},a} &= \ln\left(I_{\mathrm{H},0} G(E_{\mathrm{H}}) e^{-\alpha_a(E_{\mathrm{H}}) t}\right) - w \ln\left(I_{\mathrm{L},0} G(E_{\mathrm{L}}) e^{-\alpha_a(E_{\mathrm{L}}) t}\right) && (2.6) \\ &= \ln\left(I_{\mathrm{H},0} G(E_{\mathrm{H}})\right) - w \ln\left(I_{\mathrm{L},0} G(E_{\mathrm{L}})\right) - \alpha_a(E_{\mathrm{H}}) t + w \alpha_a(E_{\mathrm{L}}) t && (2.7) \end{aligned}$$

and

$$\begin{aligned} I_{\mathrm{DE},a} &= \ln\left(I_{\mathrm{H},0} G(E_{\mathrm{H}}) e^{-\alpha_a(E_{\mathrm{H}})(t-t_g) - \alpha_g(E_{\mathrm{H}}) t_g}\right) \\ &\quad - w \ln\left(I_{\mathrm{L},0} G(E_{\mathrm{L}}) e^{-\alpha_a(E_{\mathrm{L}})(t-t_g) - \alpha_g(E_{\mathrm{L}}) t_g}\right) && (2.8) \\ &= \ln\left(I_{\mathrm{H},0} G(E_{\mathrm{H}})\right) - w \ln\left(I_{\mathrm{L},0} G(E_{\mathrm{L}})\right) - \alpha_a(E_{\mathrm{H}})(t - t_g) - \alpha_g(E_{\mathrm{H}}) t_g \\ &\quad + w \alpha_a(E_{\mathrm{L}})(t - t_g) + w \alpha_g(E_{\mathrm{L}}) t_g && (2.9) \end{aligned}$$

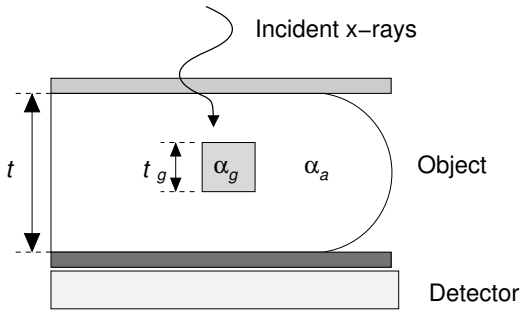

Figure 2.8: Object to be imaged having thickness t and composed of adipose and glandular (thickness t_g) tissues.

By tuning the weight factor, it is possible to set $I_{\mathrm{DE},a} = I_{\mathrm{DE},ag}$ for cancellation of the background tissue [59]:

$$w = \frac{\alpha_a(E_{\mathrm{H}}) - \alpha_g(E_{\mathrm{H}})}{\alpha_a(E_{\mathrm{L}}) - \alpha_g(E_{\mathrm{L}})} \tag{2.10}$$

With the background tissue contrast cancelled in combined, dual-energy image, lesions in the object will be enhanced.

2.5 Performance metrics

Several performance metrics will be used throughout the thesis. The most important metrics used in the analysis of the detectors presented are briefly summarized in the following sections. For more information on the metrics discussed below, the reader is referred to comprehensive medical imaging and image science textbooks [60, 61, 62, 63].

2.5.1 Modulation transfer function and noise power spectrum

The modulation transfer function (MTF) describes the (spatial) frequency response of the system. An input signal may carry information spanning many frequencies however they may not all be passed equally to the output of the system due to non-idealities such as blurring in the x-ray conversion layer. A conceptual illustration of the MTF is shown in Fig. 2.9.

The MTF of an imaging system may be experimentally determined by calculating the magnitude of the Fourier transform of the point spread function (PSF) or line spread

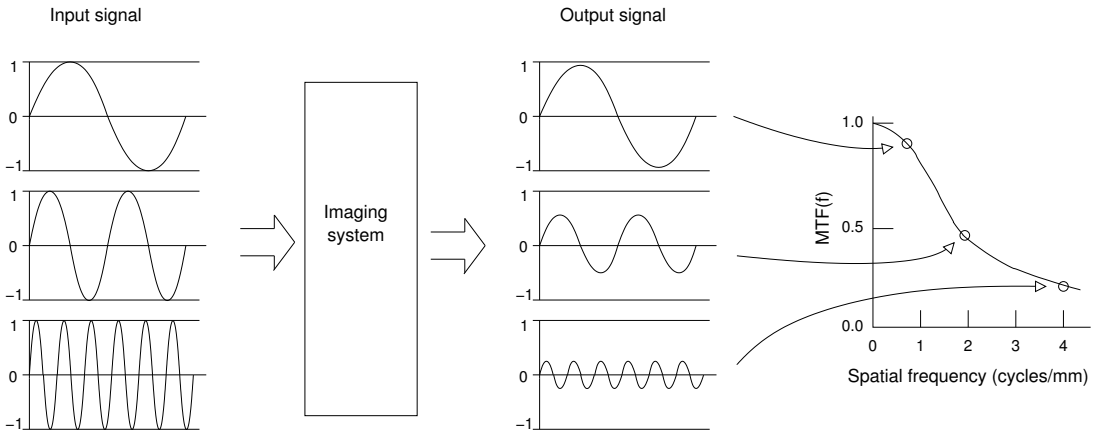

Figure 2.9: Conceptual depiction of MTF. Adopted from [64].

function (LSF) of the system. The input for the PSF is a pin hole source while the input for the LSF is a line source, which simulate a delta function in two and one dimensions, respectively.

The noise power spectrum (NPS) indicates the magnitude and frequency distribution of noise present in the image. Sources of noise include the electronic noise from the readout circuit, anatomical noise in the object, and quantum noise from the statistical fluctuations in the arrival of photons. The NPS can be experimentally determined by calculating the square of the Fourier transform of the image subtracted by its mean. The variance is given by integral of the NPS over all frequencies:

$$\sigma^2 = \int\int \mathrm{NPS}(u,v)dudv \tag{2.11}$$

where u and v are spatial frequencies. Although the variance quantifies the noise in the image, it does not give information on the frequency distribution of the noise.

2.5.2 Noise equivalent quanta and detective quantum efficiency

To quantify the performance of the imaging system, metrics are required that include information of both the signal and noise. The noise equivalent quanta (NEQ) is equal to the square of the output signal to noise ratio:

$$\mathrm{NEQ}(u,v) = \mathrm{SNR}^2_{\mathrm{out}} = \frac{\left|\overline{Q_{\mathrm{in}}}T(u,v)\right|^2}{\mathrm{NPS}(u,v)} = \frac{\mathrm{MTF}^2(u,v)}{\mathrm{NPS}(u,v)/\overline{I^2_{\mathrm{out}}}} = \frac{\mathrm{MTF}^2(u,v)}{\mathrm{NNPS}(u,v)} \tag{2.12}$$

where $\overline{Q}_{\text{in}}$ is the mean number of input quanta per unit area, $|T|$ is the system transfer function equal to the system gain, G, multiplied by the system MTF, $\overline{I}_{\text{out}}$ is the mean output signal, and NNPS is the normalized NPS. The NEQ can be thought of as the number of quanta that were used to produce the image if only Poisson (quantum) noise is present. When more noise sources are present the NEQ can be thought of as the number of quanta that the system appears to have used to create the image [65].

To quantify how well the SNR at the input is passed to the output of the imaging system, the detective quantum efficiency (DQE) can be used:

$$\text{DQE}(u,v) = \frac{\text{NEQ}(u,v)}{\overline{Q}_{\text{in}}} = \frac{\text{SNR}^2_{\text{out}}}{\text{SNR}^2_{\text{in}}} \tag{2.13}$$

where the second equality comes from $\text{SNR}_{\text{in}} = \overline{Q}_{\text{in}}/\sqrt{\overline{Q}_{\text{in}}}$ for Poisson distributed quanta. The DQE has a maximum of unity (for an ideal system) and is unitless.

2.5.3 Signal difference to noise ratio and detectability index

Typically when analyzing an image one is less interested in the absolute value of an area and instead interested in the difference in signal between nearby regions, or points, in the image (see Fig. 2.10). A metric used to quantify the difference in signal amplitude relative to the noise in the image is the signal difference to noise ratio (SDNR), which is given by:

$$\text{SDNR} = \frac{|\overline{I}_c - \overline{I}_b|}{\sqrt{\sigma_c^2 + \sigma_b^2}} \tag{2.14}$$

where the subscripts c and b refer to the object and background, respectively, and σ^2 is the variance. This metric does not contain spatial frequency dependent information of the object, signal, or noise.

The performance of the detection task of an object $\Delta p(x,y)$ (whose Fourier transform is $\Delta P(u,v)$) can be quantified by the ideal observer SNR, or detectability index, which takes into account the spatial frequency dependence information and is given by:

$$d'^2 = \text{SNR}_i^2 = \int\int |\Delta P(u,v)|^2 \text{NEQ}(u,v) du dv \tag{2.15}$$

This performance metric is especially useful when the object desired to detect is known. The ideal observer is an observer that uses all the information available, i.e. information contained in all frequencies. Other more complex observers have been studied to better characterize the visual response of human observers [66], however these observers are beyond the scope of this project.

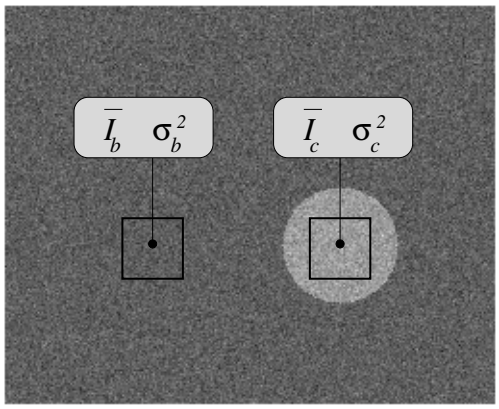

Figure 2.10: Image containing a disc object within the background. The signal and variance are determined within a region of interest in the object and background, denoted by subscripts c and b respectively.

Chapter 3

Previous work

3.1 Contrast-enhanced mammography (CEM) methods

The methods that have been previously leveraged for contrast-enhanced mammography are summarized below. Namely these methods are *temporal subtraction*, *dual-energy subtraction*, and *photon counting*.

3.1.1 Temporal subtraction (dual exposure)

As the name suggests, the images used for subtraction are taken at two different points in time. In temporal subtraction, a first image of the breast is acquired before the administration of a contrast agent. This image is known as the pre-contrast image. A contrast agent, for example an iodinated contrast agent with a K-edge at 33.2keV, is then intravenously injected into the patient. A second image is then taken after the intravenous administration of the contrast agent. This image is known as the post-contrast image. Once both of these images are acquired, software is used to subtract the pre-contrast image from the post-contrast image [30]. Since both images have approximately the same intensity for the pixels where the contrast agent was not present, the background structure in those pixels is removed during subtraction. The result is an image with enhanced lesions due to the accumulation of the contrast agent.

The tube voltage is chosen higher than the K-edge of the contrast agent to be able to capture the difference in attenuation of when the contrast agent is present and when it is

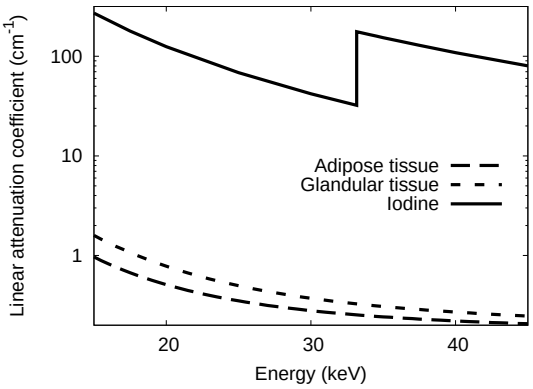

Figure 3.1: Linear attenuation coefficients for adipose and glandular breast tissues and iodine. Attenuation coefficients obtained using data from [43, 67, 68].

not present. Typically, voltages in the range of 45 to 49kVp are used for good separation between high and low energies. Figure 3.1 shows the linear attenuation coefficients for adipose and glandular breast tissue as a function of energy. The linear attenuation coefficient for iodine (contrast agent) is also shown and the K-edge can be seen at 33.2keV. Note that although the tube voltage for both images is traditionally the same, the use of different tube voltages for temporal subtraction has also been examined [13]. Such a technique was optimized by Skarpathiotakis *et al* [28] using the SDNR and dose, and followed by a clinical study by Jong *et al* [10].

The advantage of using temporal subtraction for CEM is that the same tube voltage and filter settings may be kept for both exposures. Another advantage of temporal subtraction is that it is possible to view the enhancement and washout patterns of the agent [23]. The drawback, however, is that motion artifacts will appear in the resulting image and cause image misalignment due to the patient movement from before and after the contrast agent is administered.

Using this method, the dose delivered to the patient is similar to that of a single view conventional mammogram. Tomosynthesis using temporal subtraction (with pre- and post-injection images) was also investigated, however, as expected, motion artifacts are problematic [12]. As an example, the time between the registration of the pre- and post-injection images can be greater than 10 minutes [69].

3.1.2 Dual-energy subtraction (dual exposure)

For the dual-energy subtraction method, the pre-contrast image is eliminated and instead two images are taken after the injection of the contrast agent, each image using a different voltage for the x-ray tube. One of the images is taken with an x-ray beam having a narrow x-ray energy spectrum centered below the K-edge of the contrast agent. This is known as the low-energy image. The other image is taken with an x-ray energy spectrum centered above the K-edge of the contrast agent. This is known as the high-energy image. As an example, in the study by Lewin *et al* [11], where an iodinated contrast agent was used, the x-ray tube voltage for providing the low-energy (LE) spectrum was in the range of 22-33kVp while the x-ray tube voltage for providing the high-energy (HE) spectrum was in the range of 44-49kVp.

The attenuation of the LE and HE x-rays in the soft tissue will be approximately the same, as can be seen in Fig. 3.1. This leads to similar contrast of the soft tissue in the LE and HE images. The attenuation of the HE x-rays will be much greater in the contrast agent compared to the attenuation of the LE x-rays. Once the LE and HE images have been acquired, software is used to subtract the LE image from the HE image to obtain an image where the material which has accumulated the contrast agent is enhanced.

One benefit of the dual-energy subtraction method is that images can easily be taken from different angles without the need to match pre-contrast and post-contrast images. This allows radiologists the freedom of choosing desired projections and patient positioning once the contrast agent has been injected, which is desirable, for example, during biopsy [11]. In addition, since both images (the LE and HE images) are taken within a shorter period of time compared to the temporal subtraction method, there are less motion artifacts present during the subtraction of the images and thus the effect of the patient motion is reduced [6].

A mean time between HE and LE image acquisitions has been reported as approximately 30s [23]. The dose was estimated to be 20%-50% higher than the dose in a single projection for conventional mammography. A drawback of this method is that it cannot capture the tumor enhancement kinetics (due to the limit on total number of images to keep the patient dose sufficiently low). An advantage is that multiple views of the same breast are possible. In addition, the patient can better tolerate the dual-energy method compared to temporal subtraction since the duration of breast compression is smaller.

Another method for dual-energy subtraction that was examined uses the Ross filter (i.e. balanced filter) method [70] to separate the spectrum of radiation into two separate spectra using three different exposures and three different filters (one of them being iodine)

[14]. The advantage of using this method is that there is no need to alter the x-ray tube configuration or voltage. The transmittance of the filters is made so that they are equal except for the energies between the K-edges of the different filters. The LE signal is the difference between the signal from the second filter and the first filter. The HE signal is the difference between the signal from the third filter and the second filter. Subtraction of the LE and HE signals is carried out to create the contrast-enhanced image. Due to the requirement of multiple exposures, motion artifacts may appear in the resulting image.

Although the effect of the patient motion is reduced for the dual-energy subtraction method, motion effects still exist, for example due to cardiac, respiratory, or patient movement [71]. To reduce the motion effects present in the temporal subtraction and dual-energy subtraction methods, having a method which uses a single exposure would be ideal. In addition to the problem of motion artifacts, image lag, which is caused by charge from a previous exposure that generates a signal in a subsequent image, can have a negative effect on image quality for dual-exposure methods [72].

3.1.3 Photon counting and differential beam filtering (single exposure)

One of the methods to eliminate the motion artifacts is to use a photon counting detector to split the spectrum of a single exposure of radiation [59, 73]. Due to the use of a single exposure, there is no need to modify the x-ray tube or filtration between exposures [74].

In this method the contrast agent is administered and then the patient is exposed to a single exposure of radiation. The spectrum of the radiation incident on the detector is split into LE and HE spectra, which is divided by the K-edge of the contrast agent. The spectrum used for this method has a peak approximately centered around the K-edge of the contrast agent to have sufficient LE x-ray photons below the K-edge and HE x-ray photons above the K-edge. Incident photons within the LE spectra are counted towards creating a LE image while incident x-rays within the HE spectra are counted towards creating a HE image. The LE image is then subtracted from the HE image once both images have been obtained. One of the limitations of this method is the difficulty in achieving an ideal electronic threshold level to separate the spectrum [59].

Instead of thresholding, it is also possible to separate LE and HE x-ray photons from a single-exposure spectrum using differential filtering where two filters are setup so that a certain number of detectors acquire the LE image while the others acquire the HE image [17].

Both these techniques have been carried out using slot scanning detectors. Slot scanning photon counting detectors have the advantage of being quantum noise limited and have increased scatter rejection however there is increased loading on the x-ray tube and a longer scan time [75, 17].

3.2 Multilayer detectors (single exposure) for dual-energy x-ray imaging

Previously, dual-energy images could be achieved using for example two film-screen sets or storage phosphors, which meant adding an addition film-screen or storage phosphor to the existing system. The top layer would absorb the LE x-rays while the bottom layer would absorb the HE x-rays. The conversion material for both layers need not be the same. A filter, e.g. made of copper, was typically placed between the detection layers to harden the beam (e.g. 120kVp beam) before it reached the bottom layer. Such a filter was required to achieve better spectral separation of the spectrum that is absorbed in each layer. This filter may absorb a significant number of x-rays, which decreases the efficiency of the system. As previously mentioned, multilayer detectors made of storage phosphors and film-screen sets for dual-energy imaging have been investigated for numerous applications [8], though not yet CEM. The investigation of multilayer detectors was typically carried out for relatively high energy applications (e.g. chest imaging, $>$ 70kVp) and the optimization of such systems was limited. The following describes some of the pertinent previous work in the area of multilayer detectors for dual-energy imaging.

Obtaining the low- and high-energy images using a multilayer configuration with screen-film was described by Alvarez and Macovski [76]. Brooks and Di Chiro [77] devised and tested a detector using such a multilayer configuration for computed tomography. The detector consisted of two scintillator crystals, each attached to a different photomultiplier tube. The preliminary results demonstrated that it was possible to use such a detector for material differentiation, similar to previous studies using dual exposure methods. Dual-energy CT was also shown to be possible using xenon as the detection material in a multilayer configuration by Drost and Fenster [78].

Later, Barnes *et al* [8] proposed a multilayer detector for digital radiography. The detector consisted of a low atomic number phosphor coupled to a photodiode array for the top layer and a high atomic number phosphor coupled to a photodiode array for the bottom layer. The midfilter, or inter-layer filter, provided greater energy separation between the low- and high-energy images. To test the proposed detector, two consecutive scans were taken with single-layer detectors (for the HE image, the attenuating midfilter and top screen were placed on top of the detector being used). It was found that the dual-energy images from the multilayer detector were comparable, but somewhat noisier than images from the dual-voltage method. The performance of a slit scanning method using a similar approach to Barnes *et al* was reported by Morgan *et al* [79]. In this study the photodiode arrays were aligned one behind the other with the two phosphor screen layers facing outward.

The attenuation of photons from both photodiode arrays before the photons can reach the bottom layer reduced the efficiency of the design, however from a practical standpoint this configuration (of back-to-back layers) was preferred. The trade-off of the midfilter was also noted, as the filter size increased there was increased energy separation, however this increase was accompanied by a decrease in the bottom detector DQE.

Screen/film and imaging plates multilayer detectors for radiography were subsequently tested and optimized by different groups [80, 81] using simulation and phantom studies. It was determined that the multilayer detector performance was acceptable for clinical application, and a clinical study of the multilayer detector for chest imaging was carried out by Ishigaki *et al* [82] where it was found that the dual-energy images complemented the conventional images.

Chakraborty and Barnes [38] applied the multilayer detector to mammography to examine calcifications using dual-energy imaging. In their theoretically investigated system the multilayer detector was achieved using storage phosphor technology and the two phosphor plates were separated by a copper filter. The use of a bimodal spectrum was discussed, that is a spectrum having two peaks separated by an energy difference. Such a bimodal spectrum can be obtained using a molybdenum target where one peak is due to the characteristic x-rays and the other is due to bremsstrahlung. This spectrum is desirable so that the energy separation of the photons can be achieved before the photons reach the patient, as opposed to after, in which case the dose to the patient would presumably be greater. Around the same time, Sones and Barnes [83] determined that the quantum noise in the top and bottom layers of a multilayer are uncorrelated and independent.

Ho *et al* [84] presented the first detailed comparison of single- and dual-exposure dual-energy methods for the application of chest imaging using computer simulations.It was found that the dual-exposure method had a greater SNR. This was mainly attributed to the greater energy separation capabilities of the low- and high-energy components. In this study the multilayer detector SNR was found to be $\sim 43\%$ of the dual-exposure method, however the study was limited to a 140kVp beam. It was also found that the noise of the subtracted multilayer image was mainly caused by the bottom detector image, i.e. HE image.

A somewhat different approach of viewing images was discussed by Boone *et al* [37]. The dual-energy image was obtained using a multilayer detector consisting of scintillation layers of different types The simulation study focused on better imaging of microcalcifications and the dual-energy image was colored and overlaid over the conventional single-energy mammogram. Such an overlaying scheme was used to prevent an increase in number of images that must be read per patient, i.e. to not affect throughput.

Ohki [85] applied the multilayer method to intra-oral radiography by placing films separated by a copper or tin midfilter, i.e. inter-film filter. The choice of midfilter was determined through theoretical and experimental studies and optimized to measure bone density. Since setting the film at the same position for both exposures of a dual-exposure method is difficult for intra-oral radiography, the use of a single-exposure technique is warranted. The top film, which obtains the LE image, can be used as a conventional intra-oral radiogram. Since films were used in this study, the layer thicknesses were not optimized to improve spectral separation of the LE and HE images.

Aside from using a copper or conventional material as the midfilter, the use of phosphor plates for additional filtration was investigated by Ergun *et al* [86]. In their configuration, the cassette was loaded with four phosphor plates, where the top recorded the LE image and the bottom recorded the HE image. The centre two were used for filtering, i.e. hardening, the beam. Subsequently the system was used in a chest imaging clinical study by Kelcz *et al* [87]. When using the dual-energy images, improvement in nodule detection and characterization was shown for all observers. Through computer simulations, Stewart and Huang [88] did not find significant differences in performance when using imaging plates as the midfilter as opposed to copper or tin.

Gaunt and Barnes [34] investigated the optimization of multilayer detectors for chest imaging that provide bone and soft-tissue images. Different phosphor sets (top/bottom) were examined. It was found that the choice of the bottom layer phosphor was the component that could lead to the greatest improvement in image quality, since the image noise could be reduced by a factor of 2 when a bottom layer with a near unity DQE is used. It was also found that using the highest attainable tube voltage lead to the greatest performance.

The challenge of moderate spectral separation with the multilayer detector was solved for computed radiography by Alvarez [89]. The solution involved coupling an optical chamber to the top layer and shielding the chamber from the bottom layer. The x-ray tube is first set to a high potential to provide a HE exposure to the multilayer detector. The stored image in the top (LE) detector is erased by a flash of light from the optical chamber. Next, the tube is set to a low potential to provide a LE exposure to the multilayer detector. In this way the bottom layer obtains the charge from the HE photons and the LE photons that have made it past the top detector. The top layer, assuming one hundred percent erasing efficiency, is left with the charge from the absorbed LE photons. If there is no need to use, i.e. switch, filters for the two exposures, the switching from the two exposures can take place on the order of 10s of milliseconds. Changing the filters for the two exposures will however take more time. Using achievable erasing fractions at the time, an SNR improvement of more than 4 times was found. With this proposed scheme, it was

found that the performance of the multilayer detector was still slightly less ($\sim$ 10% less) compared to that of the optimized dual-exposure technique. Also, this method requires a fast reseting technique to be available and still requires two separate exposures.

Heismann *et al* [32] investigated the multilayer detector for continuous radiation energy-resolving CT. The prototype was essentially two stacked standard detector modules, with a reduced top module scintillator thickness. The experimental results agreed well with the expected results. Carmi *et al* [33] used multilayer detectors made of stacked scintillators for material separation, specifically iodine-calcium separation, in dual-energy CT (140kVp). This configuration was later used by Kappler *et al* [90, 91] and consists of the top and bottom scintillators separated by a thin reflector. The optical photons produced in the scintillators are read out by sidewise mounted photodiodes. Due to the dose constraints in CT, the midfilter is this configuration was not used. The advantage of the multilayer detector in dual-energy CT compared to the dual-source, i.e. dual exposure, technique is that there is no cross-scatter interference in the LE and HE signals. However, it was found that the multilayer detector required around twice the dose of the dual-exposure technique to achieve the same performance [90]. In addition, the spatial resolution and scalability of this method is limited due to the configuration of the side-mounted photodiodes.

Richard and Siewerdsen [31] compared the performance of a hypothetical multilayer detector with a single-layer detector for dual-energy chest imaging. Both detectors were based on flat panel technology using CsI:Tl scintillators coupled to a photodiode array. From a DQE comparison it was found the single-layer detector (dual exposure) has a improvement factor of 2 for DQE and nodule contrast, though the anatomical noise was not considered. In addition the multilayer detector model was relatively simplistic and the detector layers (top/bottom/midfilter) did not appear to be optimized.

The multilayer detector is of course not only limited to medical imaging. Macdonald [35] investigated the use of a multilayer detector for airport security. Energy discrimination in such an application allows better detection of plastic explosives, for example. The built and tested detector prototype used CsI:Tl scintillators and was used in combination with a 145kVp x-ray source. Lower cost multilayer detectors based on terbium doped gadolinium oxysulfide (Gd_2O_2S:Tb) have also been investigated for this application [92].

In addition to the multilayer designs involving two layers, a three-layer design has also been investigated by Allec and Karim [15]. The three-layer design is based off the balanced filter (Ross filter) concept [70]. The thickness of the layers are designed such that when the signals from two adjacent layers are subtracted, the resulting signal corresponds to the signal between the K-edges of the different layers' phosphor or photoconductor (each layer is comprised of a different phosphor or photoconductor). It was found however that

K-fluorescent x-rays from one layer may get absorbed in adjacent layers, which reduces the effectiveness of the design.

Besides the methods mentioned above, the use of multilayer detectors for x-ray imaging is still an active area of research. For example there is ongoing work on using multilayer detectors for spectral microCT [93] and reducing the detector cost by reducing the number high-energy detector elements [94]. Previous research efforts however have typically not focused on multilayer large area flat panel imagers using current technology. They have also not addressed the design requirements or performance analysis for contrast-enhanced mammography.

Chapter 4

Multilayer detector (single exposure) for CEM

A single-exposure dual-energy method previously leveraged for medical imaging and security applications uses a multilayer (or sandwich) detector structure [32, 34], though its use for CEM has yet to be investigated. In this multilayer method a single exposure is used to acquire two images, where a LE signal is acquired by the top detection layer and the HE signal is acquired by the bottom detection layer. Since both images are acquired instantaneously, this multilayer acquisition scheme could potentially be used in CEM to eliminate motion artifacts.

4.1 Project description and contributions

This thesis describes the work for a project that investigates the use of a multilayer structure for medical imaging purposes geared specifically towards CEM. The signal from the different layers may be used in an additive (general mammography), stand-alone (general mammography) or subtractive mode (CEM) since the two detectors are always present, however additional modes of use of the multilayer detector, such as those mentioned or CEM tomosynthesis, are beyond the scope of this project. The project targets the use of the multilayer detector for CEM, which has not previously been investigated. Typically the multilayer detector was used for high x-ray energies, however this project targets relatively low energies (< 60kVp). Previously storage phosphors or screen-film sets were used. In this project the use of large area flat panel digital imaging detectors for the multilayer

are investigated. The system, which comprises the incident spectra (e.g. tube voltage), the detector (e.g. conversion layer thicknesses), and the image combination (e.g. the image subtraction weight factor), is optimized to achieve the greatest theoretical performance. The contributions of the project are listed below.

- Designing a dual-energy single-exposure multilayer detector for CEM
- Designing a dual-energy dual-exposure single-layer detector for CEM
- Comparing the theoretical performance of single-layer and multilayer detectors for CEM
- Experimentally testing multilayer and single-layer detectors for CEM
- Validating CEM detector theoretical models with experimental results
- Adding motion artifacts to dual-exposure CEM image noise and performance analysis and estimating their effect
- Validating CEM image noise models with CEM images from a clinical study
- Adding anatomical noise to dual-energy noise reduction technique analysis and estimating potential noise reduction improvements

This project entailed the design, through theoretical studies, of multilayer and single-layer x-ray detectors for CEM capable of energy discrimination. A framework to design an effective CEM detector using a-Se as the detection material was established. Through a simulation study, the design parameters and settings leading to the optimal performance were determined, which include: tube voltage, tube target type, filtration, photoconductor thickness, weight factors, and relative intensity ratio. Using the optimal system parameters, the performance of the multilayer and single-layer detectors were then compared. Proof-of-concept multilayer and single-layer detectors were tested. The theoretical studies were validated with experimental results from the prototype detectors. The effect of motion artifacts were studied to have a fairer comparison between the single-layer and multilayer detectors. Noise models were extended to include noise caused by motion artifacts. Noise analysis from clinical images of a dual-energy CEM clinical study was carried out to validate motion noise models. Noise reduction technique models were extended to include anatomical noise and clinical images were used to validate the extended noise models. Noise reduction techniques were applied to the single-layer and multilayer detectors to determine if image quality could be improved.

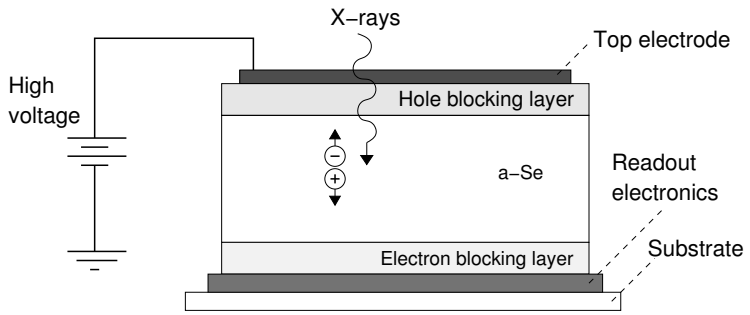

Figure 4.1: Conventional single-layer a-Se detector (not to scale) for mammography.

4.1.1 Single-layer detector

Conventional single-layer detectors are the basis of the multilayer detector, therefore it is worthwhile to first discuss the single-layer a-Se detectors used in this study. A schematic of the detector is shown in Fig. 4.1. The positive bias of the high voltage power supply is applied to the top electrode so that the collecting electrode, at the pixel, is collecting holes, the faster carrier in a-Se. The high voltage power supply is set to achieve an electric field of 10V/μm within the a-Se, which is a typical electric field. The hole and electron blocking layers prevent injection of carriers from the electrodes to keep the dark current low. Several materials, e.g. polyimide [49], have been investigated and found to be appealing blocking layers for a-Se detectors. In addition, the bottom blocking layer (denoted as the electron blocking layer in the figure) may act to improve the stability of the a-Se layer [95]. The detector is energy integrating, similar to commercial a-Se detectors, thus the readout electronics consist of thin-film transistors, storage capacitors, and charge amplifiers.

4.1.2 Multilayer detector

In the multilayer detector, due to the shorter absorption depth of LE photons (see Fig. 4.2) a single exposure of x-rays leads to a LE signal in the top detection layer and a HE signal in the bottom detection layer. The thicknesses of the detection layers are chosen such that the top layer absorbs a large fraction of the LE x-rays while the bottom layer absorbs a large fraction of the HE x-rays. Both images are taken instantaneously, thus no motion artifacts exist. Once the images are acquired, the LE image is subtracted from the HE image to obtain the enhanced image.

A schematic diagram of the multilayer detector design is shown in Fig. 4.3. In the implementation shown, two conventional flat panel detectors are stacked on top of each

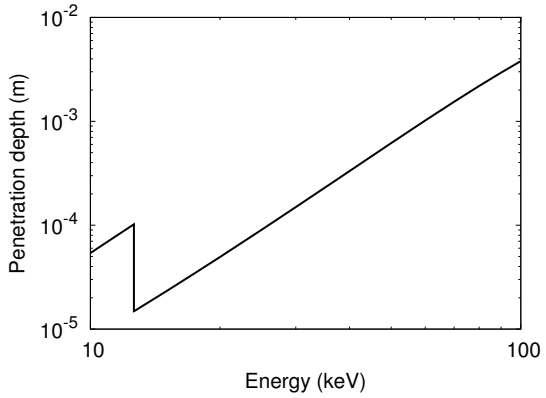

Figure 4.2: Absorption depth of x-ray photons in a-Se. The absorption depth, sometimes called penetration depth, is equal to $1/\alpha(E)$ and refers to the depth within a material that the intensity reduces to $1/e$ ($\sim 37\%$) of its original value. The K-edge of a-Se can be seen at 12.6keV.

other where L_1 refers to the thickness of the top conversion layer (a-Se) and L_2 refers to the thickness of the bottom conversion layer (also a-Se). Also shown is a midfilter located between the conversion layers. This optional midfilter may serve as an additional filtering layer to harden the x-ray spectrum incident on the bottom conversion layer. For the single-layer detector there is only one conversion layer and substrate pair and the thickness of the photoconductor will simply be referred to as L.

A schematic illustrating an example of the differences in LE and HE spectra for the multilayer and single-layer detectors is shown in Fig. 4.4. The LE and HE images acquired using the multilayer and single-layer detectors are combined using weighted image subtraction. Weighted image subtraction is used for CEM image combination since cascaded system models can be readily applied and subtraction has been shown to provide comparable quality with another combination technique, the basis decomposition method [96]. The subtracted image is given by:

$$I_{\mathrm{CE}} = \ln(I_{\mathrm{H}}) - w \ln(I_{\mathrm{L}}) \tag{4.1}$$

where I_{H} and I_{L} are the HE and LE images respectively and w is the weight factor. The optimal weight factor is that which reduces the anatomical noise the most in the subtracted image.

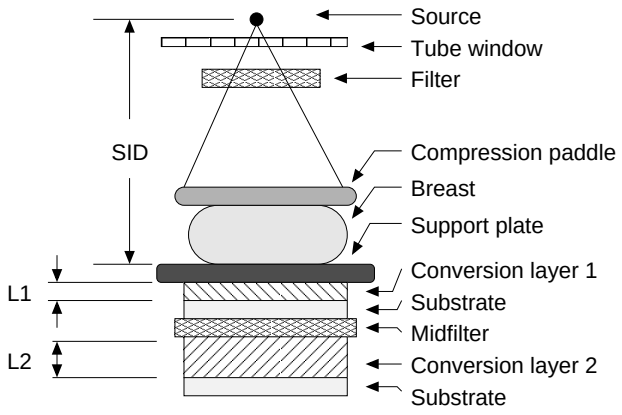

Figure 4.3: Example implementation of the multilayer detector using two stacked conventional mammography flat panel detectors.

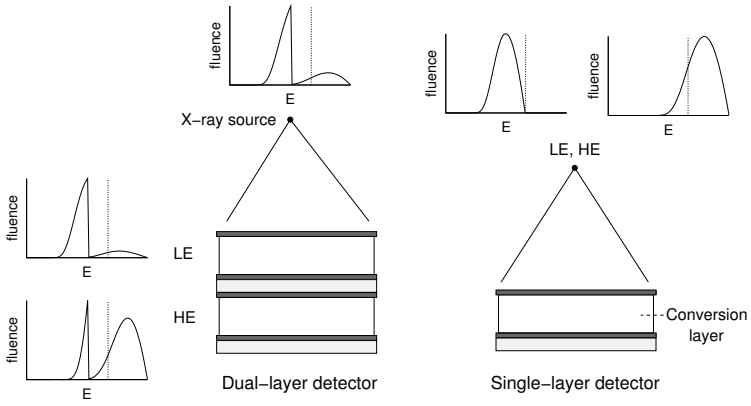

Figure 4.4: Schematic of the multilayer and single-layer detectors including exposure configuration (not to scale). Corresponding example spectra are included (dashed line is K-edge of iodine) to indicate the normalized spectra of x-ray sources and, in the case of the multilayer detector, the normalized attenuated spectra in the two layers.

Chapter 5

Theoretical system optimization

5.1 Introduction

The goals of the theoretical system optimization are to design and evaluate a multilayer detector for CEM, and to design and evaluate a single-layer detector for CEM for performance comparison. To investigate the potential usefulness of the multilayer detector for CEM, the system parameters are first optimized to achieve the greatest performance. For a fair single-layer detector comparison, the system parameters for the single-layer detector are also optimized. Using the optimized system parameters for both detectors, the performance of the detectors is compared under different conditions (e.g. low and high dose). In this study all conversion layers are assumed to be direct detection layers that use a-Se (a conventional conversion material for mammography) as the conversion material, although indirect conversion detectors may also be applied by substituting the photoconductor with a phosphor and photodiode layer.

The theoretical optimization was broken into two components: initial investigation and detailed investigation. Since there are a wide range of parameters involved in the system optimization (tube voltage, tube target type, filtration, photoconductor thickness, weight factors, and relative intensity ratio), the optimal parameters were first determined using a computationally efficient model. The optimal parameters were then verified using a computationally complex model, which includes the spatial frequency dependence of the system components.

The computationally efficient model is a cascaded detector model evaluated at zero spatial frequency (ZSF) where the spatial frequency dependence is ignored and is not expected to affect the optimization since it is assumed that the anatomical noise has been

significantly reduced after image combination [22] and can be ignored. This model allows us to optimize the performance of the detectors over a large range of system parameters. After the initial model was implemented, the model was extended to take into account the spatial frequency dependent anatomical noise, detector response, and tumor shape. The anatomical noise of the breast was included using the available information on the frequency dependence of the anatomical noise [97]. The spatial frequency dependence of a realistic tumor was also modeled [98]. The computationally complex model is a spatial frequency dependent (SFD) model that includes the anatomical noise and the spatial frequency dependence of the tumor (detection task). This model allows us to compare the performance of the detectors while varying the image combination factor (weight factor) over a range of imaging tasks, including those where the influence of the anatomical noise may be significant. The choice of system parameters to be optimized (tube voltage, tube target, filtration, photoconductor thickness, and relative intensity ratio) was determined based on the importance of the parameters on the performance of the detectors. The spectrum of the exposure in CEM is of great importance since it has a significant effect on how well the background tissue can be removed while maintaining high contrast in the region of agent uptake. For the single-layer detector, the ratio of the two exposures (high and low) also plays a role in the contrast and noise in the combined image. In the case of the multilayer detector, the thicknesses of the photoconductor layers are particularly important since they ultimately determine the absorbed spectrum in each layer. The major differences between the initial and detailed investigation models are briefly summarized below.

Initial investigation (ZSF model):

- Use zero spatial frequency model (ignore spatial frequency dependence)
- Ignore anatomical noise (assume it has been completely subtracted)
- Use results to guide detailed investigation

Detailed investigation (SFD model):

- Use initial investigation results to guide detailed investigation
- Use spatial frequency dependent model
- Include anatomical noise
- Consider shape of tumor

5.2 Cascaded detector model

The processes involved in the conversion of x-ray photons to the final image can be described using signal and noise transfer through a cascade of processes. The cascaded detector model is used to determine the NPS and MTF to evaluate the performance of both the single-layer and multilayer detectors. It should be noted that the cascaded detector model presented corresponds to that of either the LE or HE image. A description of the dual-energy model (where the LE and HE images are combined) will be discussed in Sections 5.5 and 5.6. The following subsections first describe the types of stages considered in the cascaded detector model. Next, since there are differences between the ZSF and SFD cascaded detector models, the ZSF model is first described, followed by a description of the SFD model. Lastly, a method to determine performance metrics from the results of the cascaded detector model is presented. For a more complete description of cascaded system models the reader is referred to [99]. It is noted that although a cascaded detector model is considered here, work on an a-Se Monte Carlo detector model is part of ongoing work [100, 101].

5.2.1 Types of stages

The different stages that appear in the cascaded detector model can be categorized as: gain, stochastic blurring, deterministic blurring, aliasing, and addition. Each stage i has an incident mean number of quanta (signal), $Q_{i-1}(E,f)$, and noise (NPS), $S_{i-1}(E,f)$, where the E and f denote the x-ray photon energy and spatial frequency dependence, respectively. The depth dependence (i.e. dependence of the signal and noise on the depth of interaction withing the photoconductor), denoted by x, may also be included [102], however it has been omitted from the following equations for clarity purposes. The equations for the different stages are summarized below.

For gain stages, the mean signal and noise at each stage can be determined according to the following [103]:

$$Q_i(E,f) = Q_{i-1}(E,f)g_i(E) \tag{5.1}$$

$$S_i(E,f) = g_i^2(E)S_{i-1}(E,f) + \sigma_{g_i}^2(E)Q_{i-1}(E,f) \tag{5.2}$$

where $g_i(E)$ is the mean gain of stage i and $\sigma_{g_i}^2$ is the variance of the gain of stage i.

For a stochastic blurring stage, the output mean signal and NPS are given by [103]:

$$Q_i(E,f) = \mathrm{MTF}_i(E,f)Q_{i-1}(E,f) \tag{5.3}$$

$$S_i(E,f) = \mathrm{MTF}_i^2(E,f)S_{i-1}(E,f) + [1-\mathrm{MTF}_i^2(E,f)]Q_{i-1}(E,f) \tag{5.4}$$

where MTF_i is the MTF of stage i.

For a deterministic blurring stage, the output mean signal and NPS are given by [103]:

$$Q_i(E,f) = \mathrm{MTF}_i(E,f)Q_{i-1}(E,f) \tag{5.5}$$
$$S_i(E,f) = \mathrm{MTF}_i^2(E,f)S_{i-1}(E,f) \tag{5.6}$$

For the aliasing stage, the mean signal and NPS are given by:

$$Q_i(E,f) = Q_{i-1}(E,f) \tag{5.7}$$
$$S_i(E,f) = \sum_{l=-\infty}^{\infty} S_{i-1}\left(E, f - \frac{l}{d_{pix}}\right) \tag{5.8}$$

where d_{pix} is the pixel pitch.

For the addition stage, the signal and noise power spectrum are determined by:

$$Q_i(f) = Q_{i-1}(f) \tag{5.9}$$
$$S_i(f) = S_{i-1}(f) + S_i^2(f) \tag{5.10}$$

where S_i^2 is the additive noise of stage i.

5.2.2 a-Se detector ZSF model stages

The a-Se cascaded ZSF detector model is shown in Fig. 5.1. Note that this model is for a single imaging chain, i.e. it represents the acquisition system of either the LE or HE image. This model takes into account both the energy of the incident spectrum, since the incident spectrum is polyenergetic, and the depth of interaction, since photons absorbed at different depths of the detector led to different values of signal and noise. Briefly, the detector model may be described as follows: The quantum detection efficiency stage accounts for the interaction of incident photons with the conversion layer (a-Se). The conversion gain stage accounts for the conversion of absorbed photons into detectable electron-hole pairs (since a-Se is a direct conversion detector). Trapping of the generated charge carriers as they drift toward the electrodes is considered in the charge collection stage. Finally, electronic noise from the readout electronics is considered in the electronic noise stage. The different stages are described in detail below along with the mathematical models used to describe the signal and noise transfer. Relevant parameters for the a-Se cascaded detector model are summarized in Table 5.1.

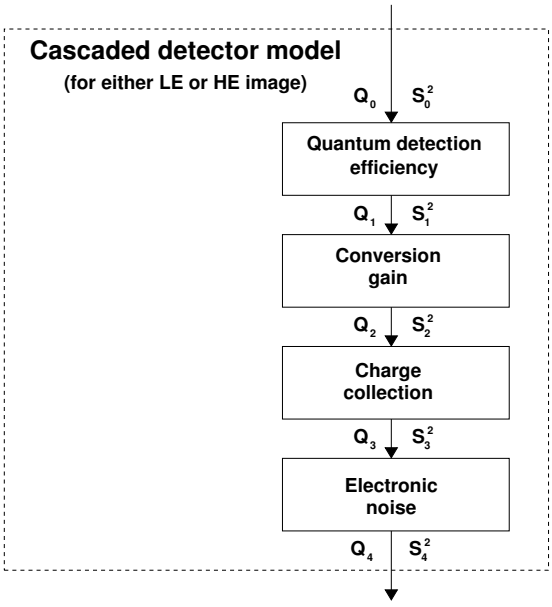

Figure 5.1: Schematic of the ZSF cascaded detector model showing the propagation of the signal (I) and noise (σ^2).

Stage: Quantum detection efficiency

The fluence and the noise power spectrum of photons incident on the detector are given by $Q_0(E)$ and $S_0(E)$ respectively where E is the photon energy. The photons incident on the detector may or may not interact with the photoconductor. The probability of interaction, or gain, and the variance of this binary selection process are given by [105]:

$$g_1(E) = \eta(E) = 1 - \exp(-\alpha(E)L) \tag{5.11}$$

$$\sigma^2_{g_1}(E) = g_1(E)(1 - g_1(E)) = \eta(E)(1 - \eta(E)) \tag{5.12}$$

where $\eta(E)$ is the quantum efficiency (i.e. probability of interaction with the detector), $\alpha(E)$ is the linear attenuation coefficient, and L is the photoconductor thickness. Since this is a gain stage, the signal and NPS at the output of this stage are given by:

$$Q_1 = Q_0 g_1 \tag{5.13}$$

$$S_1 = S_0\sigma^2_{g_1} + Q_0 g_1^2 = Q_0 g_1 \tag{5.14}$$

where the energy dependency has been omitted for clarity and $S_0 = Q_0$ since the incident photons follow a Poisson process where the mean is equal to the variance.

Table 5.1: Parameters for the ZSF and SFD a-Se cascaded detector models [104, 42, 105].

K-edge energy in keV (E_K)	12.658
K-shell contribution to photoelectric (ω_K)	0.864
K-fluorescence yield (f_K)	0.596
Frequency of production ($\mathcal{I}_{K\alpha}$, $\mathcal{I}_{K\beta}$)	0.862, 0.138
Fluorescence energy in keV ($E_{K\alpha}$, $E_{K\beta}$)	11.210, 12.503
Hole mobility in cm^2/Vs, lifetime in μs (μ_h, τ_h)	0.12, 50
Electron mobility in cm^2/Vs, lifetime in μs (μ_e, τ_e)	0.003, 200

Stage: Conversion gain

This stage represents the conversion of the absorbed photons into detectable electron-hole pairs. In a-Se the energy required to create a detectable electron-hole pair is given by the ionization energy, $W_{\pm}(E, F)$, which depends on both the applied electric field within the photoconductor (F) and the photon energy [106]. To model this dependence, the following empirical expression was used [107]:

$$W_{\pm}(E, F) = \left(6 + \frac{15 \times 10^6}{F^{0.8}}\right) \times \left(0.72 + 0.56 \times \exp(-E/62.7)\right) \tag{5.15}$$

where F has the units of V/m, E has the units of keV, and $W_{\pm}$ is given in eV. In the detector analysis it is assumed that the electric field within the photoconductor is uniform with a magnitude of $10\text{V}/\mu\text{m}$, which is a typical magnitude for conventional a-Se detectors used for mammography.

The energy absorbed within the photoconductor due to the interaction of a photon may be less than the photon's initial energy due to the escape of K-fluorescent photons. Figure 5.2 shows an example of the probability of reabsorption for different a-Se thicknesses. To determine the energy absorbed by a photon which interacted at a depth x, the absorption due to the primary and secondary (K-fluorescent) photons is considered:

$$E_{abs}(E, x) = \frac{\alpha_{en}(E)}{\alpha(E)} E + f_{ph}(E)\omega_K f_K [I_\alpha E_\alpha P_{\tau,\alpha}(x) + I_\beta E_\beta P_{\tau,\beta}(x)] \tag{5.16}$$

where $\alpha_{en}(E)$ is the energy absorption coefficient, f_{ph} is the fraction of the attenuation leading to photoelectric interactions, ω_K is the fraction of the photoelectric attenuation

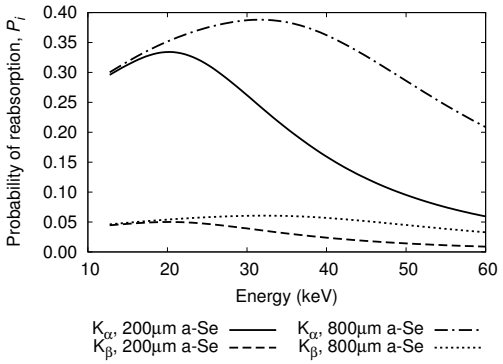

Figure 5.2: Probability of K_α and K_β reabsorption as a function of incident photon energy for different a-Se layer thicknesses.

leading to K-shell interactions, f_K is the K-shell fluorescent yield (i.e. probability that a K-fluorescent x-ray is emitted when a K-shell interaction occurs), I_α and I_β are the frequency of production of the K_α and K_β photons respectively, E_α and E_β are the K-fluorescent photon energies for the K_α and K_β photons respectively, and $P_{\tau,\alpha}$ and $P_{\tau,\beta}$ are the respective probabilities of reabsorption within the photoconductor of K_α and K_β photons created at a depth x within the photoconductor. The values of these parameters are listed in Table 5.1. The method used to calculate the probabilities of reabsorption is described in [108].

The gain for this stage is thus given by:

$$g_2(E,x) = E_{abs}(E,x)/W_{\pm}(E). \tag{5.17}$$

The variance of the conversion gain, $\sigma_{g_2}^2$, was obtained using information of the pulse height distribution, $\mathcal{P}$ (for example, see Fig. 5.3), describing the number of produced charges from an absorbed x-ray within the photoconductor. The moments of the pulse height distribution were used to find the Swank factor, A_s, which is related to the variance by the following [109]:

$$A_s = \frac{g_2^2}{g_2^2 + \sigma_{g_2}^2} = \frac{m_1^2}{m_0 m_2} \tag{5.18}$$

where the energy and depth dependencies have been omitted for clarity purposes and m_n denotes the n^{th} moment where $m_0 = 1$, $m_1 = g_2$, and $m_2 = g_2^2 + \sigma_{g_2}^2$.

The pulse height distribution, which takes into account the fluorescent photon escape, was found assuming that the gain is Poisson distributed about the mean [110]. A method

similar to that used by Fahrig *et al* [110] was used, however the depth dependence of the pulse height distribution was observed and is briefly summarized here. The Poisson distribution of the gain is modeled by a normal distribution, having a variance that is equal to the mean, which is valid so long as the mean is greater than 20 [111]. The pulse height distribution is then given by:

$$\mathcal{P}(\gamma, E, x) = \frac{\mathcal{F}(E,x)}{\sqrt{2\pi\overline{\gamma}}} \exp\left(-[(\gamma-\overline{\gamma})^2/\overline{\gamma}]/2\right) \tag{5.19}$$

$$\overline{\gamma} = \frac{E_{dep}}{W_{\pm}(E)} \tag{5.20}$$

where γ is the number of detectable electron hole pairs generated due to the interaction of a photon, E_{dep} is the mean energy deposited in the photoconductor from the absorption of a photon having energy E, and $\mathcal{F}(E,x)$ is the fraction of photons interacting at x that deposit energy E_{dep}. There are three possible energy depositing possibilities for an interacting photon (the probability of photoelectric absorption is considerably high thus it is assumed all interactions are photoelectric interactions): all of the energy of the interacting photon is deposited ($E_{dep} = E$ and $\mathcal{F} = \mathcal{F}_M$)), a K_α photon escapes ($E_{dep} = E - E_\alpha$ and $\mathcal{F} = \mathcal{F}_\alpha$), and a K_β photon escapes ($E_{dep} = E - E_\beta$ and $\mathcal{F} = \mathcal{F}_\beta$). Note that the dependencies of $\mathcal{F}$ have been omitted for clarity. For photon energies below the K-edge of a-Se, $\mathcal{F}_M = 1$ since there is not sufficient energy to produce K-fluorescent photons. Using this method the pulse height distribution was calculated for all energies of interest and the moments of the pulse height distribution were used to calculate the Swank factor given the relation in Eq. (5.18).

Given the above information, the signal and noise at the output of this stage are given by:

$$Q_2 = Q_1 g_2 \tag{5.21}$$

$$S_2 = Q_1\sigma_{g_2}^2 + S_1 g_2^2 = Q_1(\sigma_{g_2}^2 + g_2^2) = Q_1 g_2^2/A_s \tag{5.22}$$

where the energy and depth dependency has been omitted for clarity and $Q_1 = S_1$ from Eqs. 5.13 and 5.14.

Stage: Charge collection

Detectable charges, generated by the absorbed photon, drift toward the contacts due to the applied bias. These carriers may get trapped and therefore complete collection of the charge may not occur. It is assumed that the top contact (which is the radiation receiving

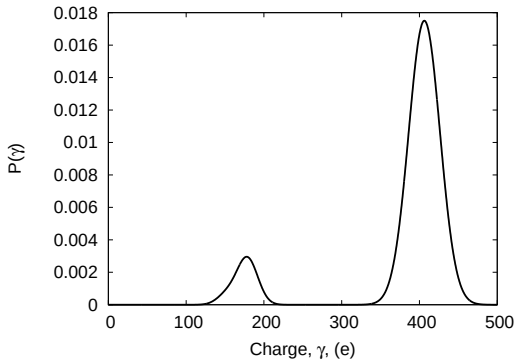

Figure 5.3: Pulse height distribution (integrated over photoconductor thickness) for 20keV incident photons and an a-Se thickness of 200μm. The large peak corresponds to full absorption while the smaller peak corresponds to the cases where K_α or K_β loss occurs.

contact) is positively biased leading to the drift of holes, the faster carrier in a-Se, towards the bottom contact. The charge collection efficiency and variance of the charge collection due to trapping of an electron-hole pair that is generated at depth x are given by [105]:

$$g_3(x) = \frac{x_e}{L}\left[1 - e^{(-x/x_e)}\right] + \frac{x_h}{L}\left[1 - e^{(-(L-x)/x_h)}\right] \tag{5.23}$$

$$\sigma^2_{g_3}(x) = \frac{1}{L^2}\big[x_e^2 + x_h^2 - x_e^2 e^{(-2x/(x_e))} - x_h^2 e^{(-2(L-x)/x_h)} - 2x_e x e^{(-x/x_e)} - 2x_h(L-x)e^{(-(L-x)/x_h)}\big] \tag{5.24}$$

where $x_e = \mu_e \tau_e F$ and $x_h = \mu_h \tau_h F$ are the electron and hole Schubweg, respectively, where μ is the drift mobility and τ is the carrier lifetime. The carrier Schubweg represents the mean distance a carrier travels before it is trapped.

The signal and noise at the output of this stage are given by:

$$Q_3 = Q_2 g_3 \tag{5.25}$$

$$S_3 = Q_2 \sigma^2_{g_3} + S_2 g_3^2 \tag{5.26}$$

where the energy and depth dependency has been omitted for clarity.

Stage: Electronic noise

The electronic noise due to the thin film transistors and charge amplifiers (which aid in the readout and amplification of the signal) is a source of noise in the resulting image. The

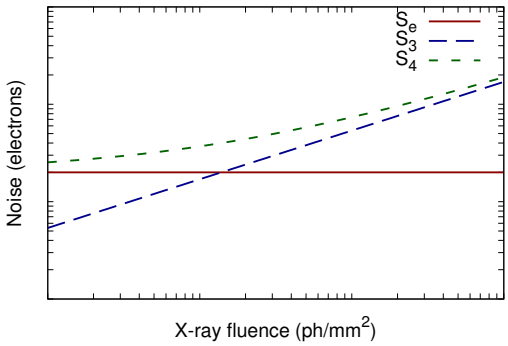

Figure 5.4: Example noise as a function of x-ray fluence incident on the detector.

electronic noise is independent of the other noise sources and is thus added in quadrature with the NPS from the output of the previous stage. The electronic noise stage is an addition stage whose contribution is added to the previous stage NPS after the integration over the photoconductor depth and photon energy (this addition is discussed further below). The electronic noise is in the range of 2000 electrons [105] per pixel, which is the value used in this study. The signal and NPS become:

$$Q_4 = Q_3 \tag{5.27}$$

$$S_4 = S_3 + S_e \tag{5.28}$$

where S_e is the electronic noise power ($\sqrt{S_e} = N_e = 2000$ electrons). From Fig. 5.4 it can be understood that the electronic noise is more significant for low incident fluence, which corresponds to low dose. Typically the x-ray fluence is set sufficiently high such that the noise is not significantly dependent on the electronic noise, though by reducing the electronic noise in the system (e.g. using CMOS technology as opposed to amorphous silicon), the fluence, and thus dose to the patient, can be reduced. For CMOS, reducing the electronic noise comes at a cost of large area compatibility.

Output signal and noise

Using the models from the above discussion, we can calculate the signal and noise power at the end of the last stage. Since the a-Se detector is energy integrating and the spectra incident upon the detector is not monoenergetic, we must integrate the signal and noise power over the energy range of values which the incident photons may possess. In addition,

we consider the depth of the interacting photons. For this, the probability density of incident photons interacting at depth x is used [105]:

$$p(E,x) = \begin{cases} \alpha(E)\exp(-\alpha(E)x)/\eta(E) & 0 \leq x \leq L \\ 0 & \text{elsewhere} \end{cases} \tag{5.29}$$

The signal and noise power at the end of the final stage of a detector then become:

$$Q_4 = \int_0^{E_m} Q_0(E)g_1(E)\int_0^L g_3(x)g_2(E,x)p(E,x)\mathrm{d}x\mathrm{d}E \tag{5.30}$$

$$S_4 = \int_0^{E_m} Q_0(E)g_1(E)\int_0^L \left(\sigma_{g_3}^2(x) + \frac{g_2(E,x)g_3^2(x)}{A_s(E,x)}\right)g_2(E,x)p(E,x)\mathrm{d}x\mathrm{d}E + S_e \tag{5.31}$$

where E_m denotes the maximum photon energy.

5.2.3 a-Se detector SFD model stages

The a-Se cascaded SFD detector model is shown in Fig. 5.5. Similar to the ZSF model this model is for a single imaging chain. The detector model consists of the following: quantum detection efficiency, K-fluorescence reabsorption and reabsorption blurring, conversion gain, aperture, image sampling (noise aliasing), and electronic noise stages. These stages are similar to those used for the ZSF model except for the inclusion of spatial frequency dependence. A quantum detection efficiency stage accounts for the interaction of incident photons with the conversion layer (a-Se). The model takes into account energy deposited by the reabsorption of K-fluorescence and the associated blurring due to non-local reabsorption. A conversion gain stage that accounts for the conversion of absorbed photons into detectable electron-hole pairs. To evaluate the output characteristics of the detector, the signal and noise of each pixel must be integrated over the entire pixel area. Since the pixels have a finite aperture size, not all spatial frequencies of the signal and noise will be passed through the system equally. This effect is taken into account by the aperture (deterministic blurring) stage. A noise aliasing image sampling stage takes into account the discrete pixel sampling and the effect of aliasing. Finally, electronic noise from the readout electronics is considered in the electronic noise stage. The effect of the charge collection stage was not found to have a significant effect using the ZSF model (demonstrating a maximum relative error in performance of 1% for optimal parameters when not taken into account), thus it was not taken into account for the SFD model. The different stages are described in more detail below.

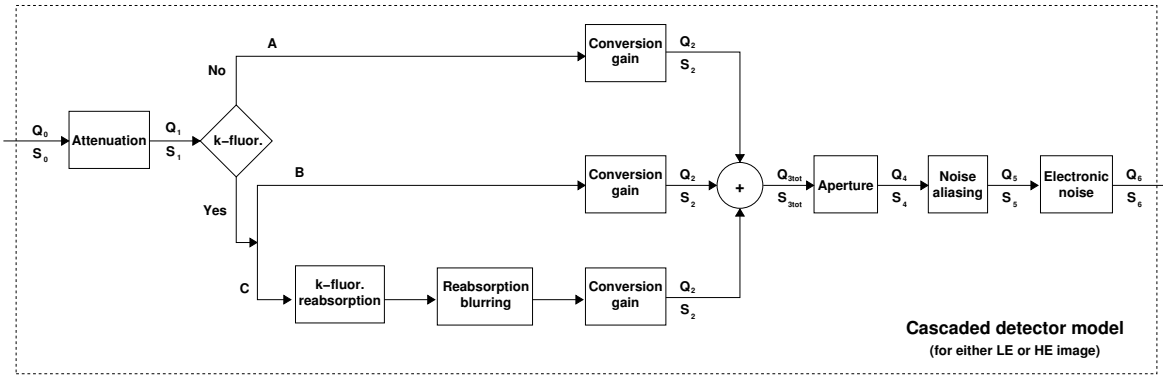

Figure 5.5: Schematic of the SFD cascaded detector model showing the propagation of the signal (Q) and noise (S). The three parallel branches represent three possible energy deposition conditions: (A) no K-fluorescent x-rays are generated, (B) K-fluorescent x-rays are generated and the remaining energy is deposited, (C) generated K-fluorescent x-rays are reabsorbed.

Stage: Quantum detection efficiency

This stage is similar to that used for the ZSF model. The fluence and NPS after this stage are given by:

$$Q_1(E) = Q_0(E)\eta(E) \tag{5.32}$$

$$S_1(E) = Q_0(E)\eta(E) \tag{5.33}$$

Stage: K-fluorescence reabsorption and reabsorption blurring

The generation of K-fluorescence may lead to the blurring of the signal and is thus taken into account. Three parallel processes are considered: (A) an interacting photon may not produce a K-fluorescent x-ray, (B) a K-fluorescent x-ray is produced and the energy not devoted to the K-fluorescent is deposited locally, and (C) a K-fluorescent x-ray is produced and its energy is deposited away from the initial point of interaction. Fluorescent x-rays generated from an L-shell electron filling the K-shell hole will be denoted as K_α while fluorescent x-rays generated from an M-shell electron filling the K-shell hole will be denoted as K_β. The contributions of both K_α and K_β are summed to provide the K-fluorescent component of the signal and noise.

The probability that a photoelectric interaction will result in the production of a K-fluorescent x-ray is given by the product of the K-shell contribution to the photoelectric

effect and the K-fluorescent yield, $\omega_K f_K$. An incident photon must have sufficient energy to generate K-fluorescent x-rays, which makes the probability of K-fluorescence generation equal to zero for photon energies below that of the K-edge. As with the ZSF model, the probability of reabsorption can be calculated numerically, e.g. using a multilayer model presented in [112].

The blurring due to the non-local reabsorption of K-fluorescent x-rays was determined using a multilayer method discussed in [113]. First the point spread function (i.e. spatial response to a point source) was determined. Next the MTF of the K-fluorescence, denoted as MTF_K, which describes the spatial frequency dependence, was calculated by taking the Fourier transform of the point spread function.

The inclusion of the K-fluorescence reabsorption and reabsorption blurring parameters in the cascaded model will be discussed in the explanation of the following stage, which discusses the conversion gain.

Stage: Conversion gain

The conversion gain stage describes the conversion of x-rays into collectable charge. The gain for the parallel branches A, B, and C are given by $g_{2A} = E/W_{\pm}$, $g_{2Bi} = (E - E_{Ki})$, and $g_{2Ci} = E_{Ki}$, respectively where $i = \alpha, \beta$. It is assumed that the noise of the gain follows Poisson statistics, making $\sigma_g = g$ for all three branches [104].

The resulting fluence and noise may be described by:

$$Q_{2A}(u,v,E) = Q_1(E)(1-\omega_K f_K)g_{2A}(E) \tag{5.34}$$

$$Q_{2B}(u,v,E) = Q_1(E)\omega_K f_K \sum_i I_{Ki} g_{2Bi}(E) \qquad (i=\alpha,\beta) \tag{5.35}$$

$$Q_{2C}(u,v,E) = Q_1(E)\omega_K f_K \sum_i I_{Ki} P_{Ki}(E) g_{2Ci}(E) \mathrm{MTF}_{Ki}(u,v,E) \tag{5.36}$$

$$S_{2A}(u,v,E) = Q_1(E)(1-\omega_K f_K)g_{2A}(E)(1-g_{2A}(E)) \tag{5.37}$$

$$S_{2B}(u,v,E) = Q_1(E)\omega_K f_K \sum_i I_{Ki} g_{2Bi}(E)(1+g_{2Bi}(E)) \qquad (i=\alpha,\beta) \tag{5.38}$$

$$S_{2C}(u,v,E) = Q_1(E)\omega_K f_K \sum_i I_{Ki} P_{Ki}(E) g_{2Ci}(E)(1+g_{2Ci}(E)) \tag{5.39}$$

$$S_{2BC}(u,v,E) = Q_1(E)\omega_K f_K \sum_i I_{Ki} P_{Ki}(E) g_{2Bi}(E) g_{2Ci}(E) \mathrm{MTF}_{Ki}(u,v,E) \tag{5.40}$$

$$Q_2(u,v,E) = Q_{2A}(u,v,E) + Q_{2B}(u,v,E) + Q_{2C}(u,v,E) \tag{5.41}$$

$$S_2(u,v,E) = S_{2A}(u,v,E) + S_{2B}(u,v,E) + S_{2C}(u,v,E) + 2S_{2BC}(u,v,E) \tag{5.42}$$

where u and v represent the spatial frequencies in two dimensions and P_i is the fraction of K-fluorescence reabsorbed that was found using the method described in [112].

The S_{2BC} term is included due to the correlation between parallel branches B and C. After the conversion gain stage the fluence and noise may be converted from polyenergetic (in x-ray photon energy) to mean values since the following stages are not x-ray photon energy dependent ($Q_2(u,v) = \int Q_2(u,v,E)dE$, $S_2(u,v) = \int S_2(u,v,E)dE$).

Stage: Aperture

The deterministic spreading aperture stage takes into account the blurring of the signal that is caused by the integration across the pixel aperture. The signal and noise become:

$$Q_3(u,v) = Q_2(u,v)\mathrm{MTF}_3(u,v)a_{pix}^2, \tag{5.43}$$

$$S_3(u,v) = S_2(u,v)\mathrm{MTF}_3^2(u,v)a_{pix}^4, \tag{5.44}$$

where a_{pix} is the size of the pixel aperture and is assumed to be square, $\mathrm{MTF}_3(u,v) = |\mathrm{sinc}(ua_{pix})\mathrm{sinc}(va_{pix})|$, and $\mathrm{sinc}(ua_{pix}) = \sin(\pi ua_{pix})/(\pi ua_{pix})$. Unless otherwise stated the square pixel aperture is assumed to be 85μm$\times 85\mu$m, which is a typical size for mammography. At the output of this stage the fluence has changed from quanta/mm^2 to mean number of quanta.

Stage: Noise aliasing

The image sampling noise aliasing stage takes into account the discrete pixel sampling and the effect of aliasing, which is caused by frequency components higher than the Nyquist frequency that fold to low frequencies. The fluence and noise become:

$$Q_4(u,v) = Q_3(u,v), \tag{5.45}$$

$$S_4(u,v) = \sum_{l=-\infty}^{\infty}\sum_{m=-\infty}^{\infty} S_3\left(u - \frac{l}{d_{pix}}, v - \frac{m}{d_{pix}}\right), \tag{5.46}$$

where d_{pix} is the pixel pitch, here assumed to be equal to the size of the pixel aperture. Although the summation indicates limits of infinity this is not practical for simulation. The nearest 'neighbours' considered in this work, which were found to provide the NPS without loss of accuracy are shown in Fig. 5.6.

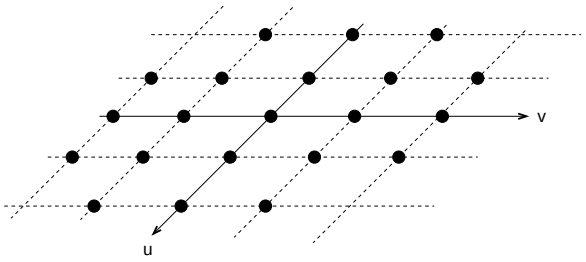

Figure 5.6: The nearest neighbours considered in this work.

Stage: Electronic noise

This stage is similar to that for the ZSF model. The electronic noise is spatial frequency independent, which leads to:

$$Q_5(u,v) = Q_4(u,v), \tag{5.47}$$

$$S_5(u,v) = S_4(u,v) + S_e. \tag{5.48}$$

5.2.4 Determining MTF, DQE, and NEQ from the cascaded model

The MTF is obtained by dividing the fluence of the final stage by the mean (zero-frequency) signal, e.g. $\mathrm{MTF}(u,v) = Q_5(u,v)/Q_5(0,0)$ for the SFD model. The NNPS is the NPS of the final stage divided by the mean signal squared, e.g. $\mathrm{NNPS}(u,v) = S_5(u,v)/Q_5^2(0,0)$. The DQE is given by:

$$\mathrm{DQE}(u,v) = \frac{\mathrm{MTF}^2(u,v)}{Q_0 \mathrm{NNPS}(u,v)} \tag{5.49}$$

where Q_0 is the input fluence at the detector. The NEQ is given by the signal to noise ratio at the output and can be written as:

$$\mathrm{NEQ}(u,v) = \mathrm{SNR}^2_{\mathrm{out}}(u,v) = \frac{\mathrm{MTF}^2(u,v)}{\mathrm{NNPS}(u,v)}. \tag{5.50}$$

5.3 Mean glandular dose

The dose absorbed by the patient being exposed to x-rays, defined as the energy absorbed per unit mass (J/kg = Gy), may be harmful to the patient and may lead to secondary

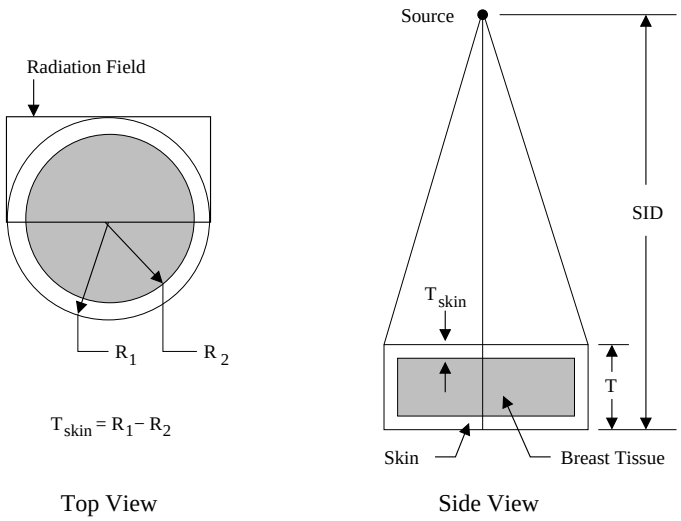

Figure 5.7: Geometry for determining the mean glandular dose. Adopted from [67, 115].

cancer. For mammography, it is believed that the glandular tissue of the breast is the tissue most sensitive or at risk radiation induced cancers [114, 67], therefore the quantification of the dose to the glandular portion of the breast is of great importance. To determine the mean glandular dose to the breast for a given incident fluence, a method similar to that described by Boone [67] was used. This method involves determining the average dose absorbed by the glandular tissue of the breast using Monte Carlo simulations. The dose to the glandular portion of the breast is used as a metric since it is thought that the glandular portion is the tissue most sensitive to radiation in the breast [115]. Using the Boone method the mean glandular dose, D_g(Gy), is given by:

$$D_g = \int \Phi(E)\theta^{-1}(E)D_{gN}(E)\mathrm{d}E \tag{5.51}$$

where Φ (photons/mm^2 per energy bin) is the photon fluence, θ^{-1} (R/(photons/mm^2)) is the photon fluence to exposure conversion factor, and D_{gN} (Gy/R) is the normalized glandular dose coefficient. In the simulations, a monoenergetic x-ray beam was directed at the breast and the dose to the glandular portion of the breast per x-ray was then determined. D_{gN} was evaluated for the monoenergetic energies of interest (one million histories per energy level) with Monte Carlo simulations using the PENELOPE software package [43]. θ^{-1} was obtained using the conversion relation from Johns and Cunningham [39]. The breast model used in the simulations is illustrated in Fig. 5.7.

In the detector optimization simulations, unless otherwise stated, the breast was defined

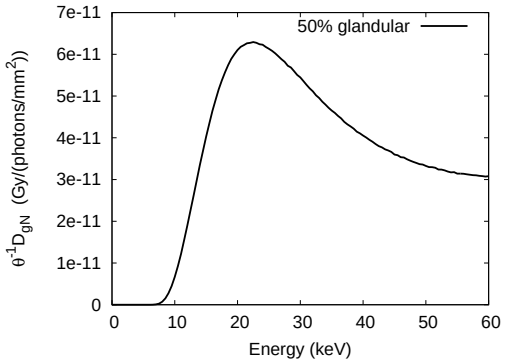

Figure 5.8: The dose per fluence, given by the photon fluence to exposure conversion factor (θ^{-1}) multiplied by the normalized glandular dose coefficient (D_{gN}), as a function of photon energy for a 45mm thick, 50% glandular breast.

as being composed of 50% (by mass) glandular tissue, having a skin thickness of 4mm, and a total thickness of 45mm. The mean glandular dose was evaluated for numerous glandular percentages and breast thicknesses over a range of x-ray energies appropriate for contrast-enhanced mammography. The source to detector distance (SID) was assumed to be 650mm. The elemental composition of the skin, adipose, and glandular tissue were taken from [116]. The results of the Monte Carlo simulations for the described breast model are shown in Fig. 5.8.

5.4 Tube spectra and attenuating layers

A wide range of filtered incident spectra were tested, which included different types of anodes: rhodium (Rh), molybdenum (Mo), and tungsten (W). The spectrum for the Rh anode was obtained using a validated method [69] of extrapolating the spectral model by Boone *et al* [117] while the Mo and W spectra were obtained from the models by Tucker *et al* [118, 119]. The spectrum of these targets was filtered using different filter materials (aluminum (Al), silver (Ag), copper (Cu), Rh, and Mo) and different tube potentials were tested. Each spectrum was attenuated by 0.5mm of beryllium (Be) to account for the tube window. The attenuation coefficients of the attenuating layers, including filters, used in the simulations were obtained from the PENELOPE Monte Carlo software package [43].

The mammography unit is assumed to have a 2.5mm lexan compression paddle and a 1.5mm carbon fiber support plate [120]. Additional attenuating layers considered in

the detector model include (for each conversion layer/substrate pair) a 0.05μm indium tin oxide (ITO) top contact layer, a 0.1μm ITO bottom contact layer, a 0.20μm dielectric layer (Si_3N_4), a 0.05μm bottom conductor (Cr), and a 1100μm thick Corning 1737 glass substrate [120]. The photons that are not attenuated by the breast are considered primary radiation (as opposed to scattered radiation) for both detector types. For several of the simulations a scatter grid was assumed to eliminate all scatter, while the primary radiation was reduced using a primary transmission fraction taken from [121] and [122]. Though not considered here, scatter radiation may also be included in the analysis [123], where it would be anticipated that its inclusion would lead to reduced performance [21]. It should be noted that the thicknesses of the conversion layers (L, $L1$, and L_2) refer only to the thickness of the a-Se layer, which does not include the layers listed above, as they are considered separately.

5.5 Dual-energy zero spatial frequency (ZSF) model

The dual-energy model combines the LE and HE cascaded detector models to evaluate the performance of the multilayer and single-layer detectors for CEM. This section describes the details of the signal, noise, and performance metric of the dual-energy model. The performance is quantified using the signal difference to noise ratio.

5.5.1 Contrast-enhanced signal and performance

Once the HE and LE signals are acquired, they are subtracted to create the enhanced image. The weighted logarithmic subtraction (or contrast-enhanced) image is obtained by the relation $I_{\mathrm{DE}} = \ln(I_{\mathrm{H}}) - w\ln(I_{\mathrm{L}})$, where I_{H} and I_{L} are the signal intensities from the HE and LE images respectively (obtained from the cascaded detector model), and w is the weight factor. Figure 5.9 summarizes the combination of the LE and HE cascaded detector models for forming the CEM image.

An optimal weight factor can be found that minimizes the anatomical noise from the variation in glandular percentage of the breast. The weight factor chosen is that which minimizes the standard deviation of the subtracted signal over glandular percentages surrounding the mean glandular percentage, given by [124]:

$$\sigma_w(w) = \left(\frac{1}{m-1} \sum_i^m \left[I_{\mathrm{DE}}(g_i, w) - \overline{I_{\mathrm{DE}}}(w) \right]^2 \right)^{1/2} \tag{5.52}$$

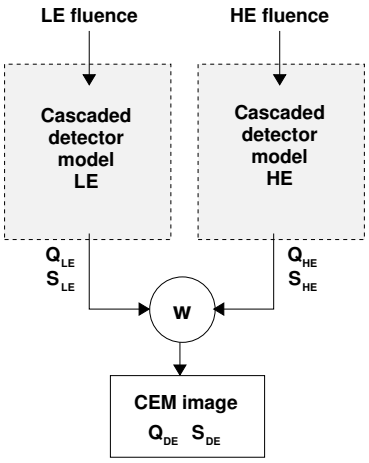

Figure 5.9: Schematic of CEM image formation with respect to LE and HE signal and noise. This schematic representation applies to both the ZSF and SFD models.

where g is the glandular percentage and $\overline{I_{\mathrm{DE}}}(w)$ is the mean subtracted signal over all glandular percentages considered. A uniform glandular distribution was assumed [22] and glandular percentages ranging from 0-100% were considered, with an increment size of 10%. As will be discussed in Section 5.9.2, this weight factor agrees well with the weight factor that minimizes anatomical noise using the SFD model.

To evaluate the performance of the detectors for CEM, the signal difference to noise ratio (SDNR) of the weighted logarithmic subtraction image is used. It should be noted that an anatomical noise source is not considered since the anatomical noise is assumed to be significantly reduced by using the optimal weight factor. The validity of this assumption is discussed in Section 5.9.2, where the results for the computationally complex SFD model, which includes an anatomical noise source, are presented. The SDNR, which is sometimes referred to as the contrast to noise ratio, is given by:

$$\mathrm{SDNR} = \frac{|I_{\mathrm{DE},c} - I_{\mathrm{DE},b}|}{\sqrt{\sigma^2_{\mathrm{DE},c} + \sigma^2_{\mathrm{DE},b}}} \tag{5.53}$$

$$\sigma^2(I_{\mathrm{DE},i}) = \left|\frac{1}{I_{\mathrm{H},i}}\right|^2 \sigma^2_{\mathrm{H},i} + w^2 \left|\frac{1}{I_{\mathrm{L},i}}\right|^2 \sigma^2_{\mathrm{L},i} \quad i = c, b \tag{5.54}$$

where the subscripts c and b denote signals from areas of the exposed breast that contain contrast agent and those that do not (background), respectively. The variance of the acquired signals, $\sigma^2_{\mathrm{HE},i}$ and $\sigma^2_{\mathrm{LE},i}$, are obtained from the cascaded detector model for the

HE and LE image acquisitions, respectively. The tumor tissue composition was assumed to be the same as skeletal muscle [125] and the tumor is modeled as the combination of both tumor tissue and contrast agent.

Relative intensity ratio (single-layer detector)

The single-layer detector has an additional parameter compared to the multilayer detector since the intensity of photons used to acquire each image (both LE and HE) may be controlled independently. For a constant dose, the performance is dependent on the ratio of these intensities and its optimization is briefly discussed here. For the single-layer detector, the fluence incident on the breast for the LE and HE exposures can be written as:

$$\Phi_i = \int \Phi_i(E)dE = \Phi_{i,0} \int \phi_i(E)dE \quad i = \mathrm{L}, \mathrm{H} \tag{5.55}$$

where $\phi(E)$ is the normalized spectrum. The relative intensity ratio, R, can then defined as $R = \Phi_{\mathrm{H},0}/\Phi_{\mathrm{L},0}$, which is the ratio of the high and low energy fluence. The optimal intensity ratio is found by maximizing the SDNR:

$$R_{opt} = \arg\max_{R} \mathrm{SDNR}(R) \tag{5.56}$$

where $\arg_x\max f(x)$ is the value of x, here assumed to be a single value, at which $f(x)$ is maximized. Note that a ratio in terms of dose, $D_{g,\mathrm{H}}/D_{g,\mathrm{L}}$, may be used in place of the relative intensity ratio since the two ratios are related.

The optimal intensity ratio was derived using Eqs. (5.53), (5.54), and (5.55) and the following relation for the total dose:

$$D_g = D_{g,\mathrm{L}} + D_{g,\mathrm{H}} = \Phi_{\mathrm{L},0}(\widehat{D}_{g,\mathrm{L}} + R\widehat{D}_{g,\mathrm{H}}) \tag{5.57}$$

where $\widehat{D}_{g,\mathrm{L}}$ and $\widehat{D}_{g,\mathrm{H}}$ are the dose deposited per incident photon for the LE and HE beams, respectively. To derive the optimal intensity ratio, the signal and NPS can be written in terms of the output of the cascaded stages:

$$j = c, b \quad i = \mathrm{L}, \mathrm{H}$$

$$I_{\mathrm{DE},j} = \ln(I_{\mathrm{H},j}) - w\ln(I_{\mathrm{L},j}) \tag{5.58}$$

$$I_{i,j} = Q_{4,i,j} = \Phi_{i,0}Q_{4,\phi,i,j} \tag{5.59}$$

$$S_{3,i,j} = \Phi_{i,0}S_{3,\phi,i,j} \tag{5.60}$$

$$\sigma^2(I_{i,j}) = S_{4,i,j} = S_{3,i,j} + S_e \tag{5.61}$$

where S_e represents the electronic noise, S (Q) with a numerical subscript denotes the NPS (signal) at the output of the corresponding cascaded stage, and the subscript ϕ denotes that the parameter has been calculated using the normalized spectrum. Substituting the relations (5.58)–(5.61) into (5.54) and (5.53) allows the SDNR to be written in terms of $\Phi_{\mathrm{L},0}$ and $\Phi_{\mathrm{H},0}$. Replacing $\Phi_{\mathrm{L},0}$ and $\Phi_{\mathrm{H},0}$ with the following, from the definition of R and Eq. (5.57):

$$\Phi_{\mathrm{H},0} = R\Phi_{\mathrm{L},0} \tag{5.62}$$

$$\Phi_{\mathrm{L},0} = \frac{D_g}{(\widehat{D}_{g,\mathrm{L}} + R\widehat{D}_{g,\mathrm{H}})} \tag{5.63}$$

provides the SDNR in terms of R. By equating the derivative of SDNR with respect to R to zero (i.e. $\partial\mathrm{SDNR}/\partial R = 0$), the following equation is found:

$$WR^4 + XR^3 + YR + Z = 0 \tag{5.64}$$

$$W = \frac{2B_2\widehat{D}^2_{g,\mathrm{H}}}{D_g}$$

$$X = \frac{2B_2\widehat{D}_{g,\mathrm{H}}\widehat{D}_{g,\mathrm{L}}}{D_g} + A_2\widehat{D}_{g,\mathrm{H}}$$

$$Y = -\frac{2B_1\widehat{D}_{g,\mathrm{H}}\widehat{D}_{g,\mathrm{L}}}{D_g} - A_1\widehat{D}_{g,\mathrm{L}}$$

$$Z = -\frac{2B_1\widehat{D}^2_{g,\mathrm{L}}}{D_g}$$

$$A_1 = S_{3,\phi,\mathrm{H},b}/Q^2_{4,\phi,\mathrm{H},b} + S_{3,\phi,\mathrm{H},c}/Q^2_{4,\phi,\mathrm{H},c}$$

$$A_2 = w^2(S_{3,\phi,\mathrm{L},b}/Q^2_{4,\phi,\mathrm{L},b} + S_{3,\phi,\mathrm{L},c}/Q^2_{4,\phi,\mathrm{L},c})$$

$$B_1 = S_{e,\mathrm{H}}(1/Q^2_{4,\phi,\mathrm{H},c} + 1/Q^2_{4,\phi,\mathrm{H},b})$$

$$B_2 = w^2S_{e,\mathrm{L}}(1/Q^2_{4,\phi,\mathrm{L},c} + 1/Q^2_{4,\phi,\mathrm{L},b})$$

The optimal R value is determined by solving the quartic roots of the above equation. Note that the resulting R will depend on dose. In the absence of electronic noise, the optimal R value is independent of dose and is simply:

$$R = \sqrt{\frac{A_1\widehat{D}_{g,\mathrm{L}}}{A_2\widehat{D}_{g,\mathrm{H}}}}. \tag{5.65}$$

5.6 Dual-energy spatial frequency dependent (SFD) model

The spatial frequency dependent model was used to evaluate and compare the performance of the two detector types under various conditions, which include changes to the contrast agent concentration, tumor size, and dose. This model is much more computationally complex than the ZSF model since it takes into account the spatial frequency dependence, not only of the detector response, but also of the imaging task and the anatomical noise. Therefore this model is used once a set of optimal system parameters (tube voltage, filtration, photoconductor thickness, and relative intensity ratio) has been determined using the ZSF model.

To evaluate the detectability and compare the multilayer and single layer detectors, the series/parallel cascaded systems model for dual-energy CEM is extended for a-Se as the detection material. The anatomical noise of the breast is taken into account using the signal dependence on glandularity in conjunction with a power law model that is incorporated in the generalized noise equivalent quanta (GNEQ).

5.6.1 Contrast-enhanced signal and performance

A slightly different formalism compared to the one used for the ZSF model is used to define the enhanced image. This formalism is used to leverage previous work ([22]) that accounts for the anatomical noise due to the breast. The low and high energy images are normalized to form the combined image with zero mean [22]:

$$I_{\mathrm{DE}} = \frac{I_{\mathrm{H}}}{\langle I_{\mathrm{H}} \rangle} - w\frac{I_{\mathrm{L}}}{\langle I_{\mathrm{L}} \rangle} - (1-w) \simeq \ln\left[\frac{I_{\mathrm{H}}}{\langle I_{\mathrm{H}} \rangle}\right] - w\ln\left[\frac{I_{\mathrm{L}}}{\langle I_{\mathrm{L}} \rangle}\right] \tag{5.66}$$

where the angle brackets denote the average of the signal over space and the approximation is for small signal differences.

The ideal-observer detectability index is given by integrating the generalized noise equivalent quanta (GNEQ) and the task function (W_{Task}) up to the Nyquist frequency [31,

22, 126]:

$$d'^2 = \int_{\mathrm{Ny}} \int_{\mathrm{Ny}} \mathrm{GNEQ}(u,v) W_{\mathrm{Task}}^2(u,v) du dv \tag{5.67}$$

$$d'^2 = \int_{\mathrm{Ny}} \int_{\mathrm{Ny}} \frac{\mathrm{MTF}^2(u,v) \Delta I^2(u,v) Y^2(u,v)}{\mathrm{NPS_D}(u,v) + \mathrm{NPS_B}(u,v)\mathrm{MTF}^2(u,v)} du dv \tag{5.68}$$

$$d'^2 = \int_{\mathrm{Ny}} \int_{\mathrm{Ny}} \frac{\mathrm{MTF}^2(u,v) W_{\mathrm{Task}}^2(u,v)}{\mathrm{NNPS_D}(u,v) + \mathrm{NNPS_B}(u,v)\mathrm{MTF}^2(u,v)} du dv, \tag{5.69}$$

where $W_{\mathrm{Task}} = \Delta I Y / \langle I \rangle$, Y describes the spatial frequency dependence of the task, $\Delta I = I_{\mathrm{background}} - I_{\mathrm{tumor}}$, MTF is the system modulation transfer function, NPS is the noise power spectrum where the subscript 'B' denotes the anatomical noise due to the breast while the subscript 'D' denotes the quantum plus detector noise, and 'G' in GNEQ denotes the generalized noise equivalent quanta which takes into account the anatomical noise.

Several factors affect the detectability index such as tube voltage, weight factor, and filtration. In addition, for the single-layer detector the ratio, $R = D_{g,\mathrm{H}}/D_{g,\mathrm{L}}$, of the dose delivered to the breast by the HE and LE images may be chosen to optimize the performance. The dose allocation (A) as defined in Ref. [31] may be calculated using the dose ratio as follows: $A = 1/(R+1)$, where $A = 0.5$ (or $R = 1$) indicates that the HE and LE exposures lead to an equal dose to the patient. For the multilayer detector the total dose is acquired within a single exposure and thus there is no defined dose ratio.

5.6.2 Dual-energy NNPS and MTF

The normalized noise power spectrum and modulation transfer function are found with the aid of cascaded systems analysis.

The MTF is obtained by dividing the fluence of the final stage (Q_5) by the mean (zero-frequency) signal while the NNPS is the NPS of the final stage (S_5) divided by the mean signal squared. The NNPS and MTF for the HE and LE spectra signals are found separately and are combined to solve the dual-energy MTF and NNPS. The high and low energy spectra signal terms (denoted by subscripts L and H respectively) are combined via the following relations:

$$\mathrm{MTF_{DE}}(u,v) = \left| \frac{-w k_{\mathrm{L}} \mathrm{MTF_L}(u,v) + k_{\mathrm{H}} \mathrm{MTF_H}(u,v)}{-w k_{\mathrm{L}} + k_{\mathrm{H}}} \right|, \tag{5.70}$$

$$\mathrm{NNPS_{DE}}(u,v) = \mathrm{NNPS_H}(u,v) + w^2 \mathrm{NNPS_L}(u,v), \tag{5.71}$$

where the weights can be obtained using $k_{\mathrm{L,H}} = I'^{\mathrm{obj}}_{\mathrm{L,H}} - I'^{\mathrm{back}}_{\mathrm{L,H}}$ where $I'^{\mathrm{obj}}_{\mathrm{L,H}}$ is the zero mean signal behind the object (tumor) and $I'^{\mathrm{back}}_{\mathrm{L,H}}$ is the zero mean signal behind the background [21]. The dual-energy NNPS (= $\mathrm{NNPS_D}$) and MTF are the terms used in Eq. (5.69) to solve for the detectability.

5.7 Anatomical noise ($\mathrm{NNPS_B}$)

The variation of glandularity (g) within the breast leads to the appearance of anatomical noise in the image. This anatomical noise follows a power law relation and is modeled by [22]:

$$\mathrm{NPS_B}(f) = \left\langle \left| \frac{dI}{dg} \right|^2 \right\rangle \frac{K}{f^\beta}, \tag{5.72}$$

where f is frequency (here the noise is assumed to be rotationally symmetric), $\beta \approx 3$ for mammograms [97], which is the value used in this study, K is a constant, I is the detected signal, and the angle brackets denote the expectation value acquired over the range of glandularity. To find the value of K, a method similar to that found in Ref. [22] was used. In this method, a crossing point of the anatomical noise and detector noise for a standard mammogram at a spatial frequency of $1\mathrm{mm}^{-1}$ was used, which is the crossing point that has been previously reported for mammograms [98]. The NPS is then divided by the mean signal squared to to get the NNPS. The simulated normalized noise power spectrum is shown in Fig. 5.10 for a single-layer absorption image showing the anatomical noise component and the component due to the acquisition of the image. It can be seen that the anatomical noise has a great effect on the total NNPS at low frequencies.

It was found that to facilitate the computation of dI/dg, the signal as a function of g could be fit using an exponential function. The fit for $I(g)$ vs g was found using the gradient descent method with the sum of the square of the differences (SSD):

$$\mathrm{SSD} = \Theta = \sum_i (f_i - h_i)^2 \tag{5.73}$$

$$m^{n+1} = m^n - \beta \nabla \Theta, \quad n \geq 0 \tag{5.74}$$

where Θ is the cost function (to be reduced), f is the fit, h is the data, m is the fitting parameter, n is the iteration, and β is a constant.

Since the signal can be fit (see Fig. 5.11), it is relatively simple to find the derivative at a given g for linear signals:

$$dI/dg = d(A\exp(-Bg))/dg = -AB\exp(-Bg) \tag{5.75}$$

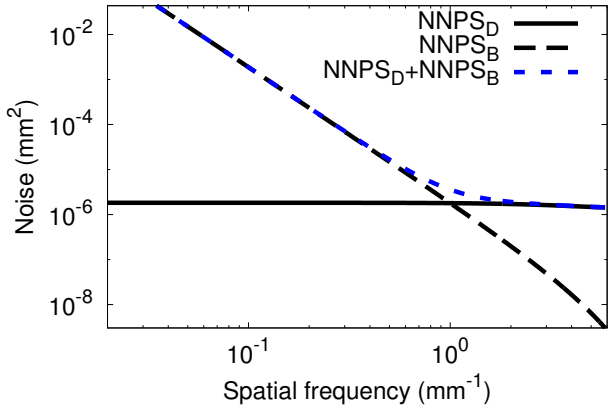

Figure 5.10: Anatomical noise ($\mathrm{NNPS_B}$), quantum plus electronic noise ($\mathrm{NNPS_D}$), and total noise ($\mathrm{NNPS_B} + \mathrm{NNPS_D}$) as a function of spatial frequency for an absorption image. A breast with a thickness of 45mm and 50% glandularity which receives a mean glandular dose 1.42mGy is assumed. For the absorption image, a 30kVp molybdenum target with 30μm of molybdenum filtration was used.

and log signals:

$$d\ln(I)/dg = -B \tag{5.76}$$

where A and B are fitting parameters.

5.8 Task function (W_{Task})

The task which is considered in this study is the finding of a tumor. The type of task is based on the two hypotheses: object-present (hyp_1) and object-absent (hyp_2), where the object is the tumor. Unless otherwise stated, the tumor in this study is assumed to be 10mm in diameter and 10mm thick. The task function is given by the Fourier transform of the difference in the hypotheses:

$$W_{\mathrm{Task}}(u,v) = |\mathcal{F}[hyp_1(x,y) - hyp_2(x,y)]|, \tag{5.77}$$

where $\mathcal{F}[x]$ denotes the Fourier transform.

To represent the tumor, the designer nodule is used, which has the following form [98]:

$$p(r) = A\mathrm{rect}(\rho/2)(1-\rho^2)^n, \tag{5.78}$$

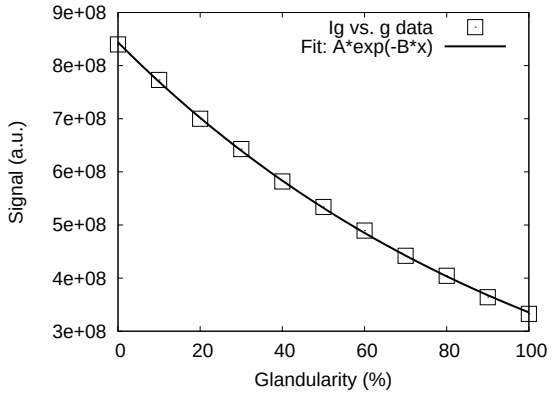

Figure 5.11: $I(g)$ vs. g for 200μm aSe detector, for a breast thickness of 45mm and a mean glandular dose of 1.42mGy (for a 50% glandular breast). The relation has been fit using the function $A * \exp(-B * g)$ where $A = 8.43988e + 08$ and $B = 0.0092281$.

where r is the radial coordinate, $\rho = r/R$ is the normalized distance, R is the nodule radius, A is a scaling factor, and n is a non-negative constant. It was found that $n = 1.5$ matched the shape for a lung nodule, and it was previously used to model tumors in mammograms [98], thus 1.5 is the value used in this study. Figure 5.12 shows the task function for the hypotheses considered. The task function will vary depending on the size of the tumor, and will for example contain larger high frequency components for smaller tumors.

5.9 Results

5.9.1 Optimal system parameters (extracted using ZSF model)

For the multilayer and single-layer system optimizations, a 45mm thick, 50% glandular breast is considered with an iodinated contrast agent having a concentration of 1.5mg/ml, which is in the clinically feasible range [59], within a cubic tumor with each edge having a length of 1cm. The mean glandular dose to the breast was chosen to be 1.42mGy to match that of the dual energy contrast-enhanced study by Lewin *et al* [11]. For both detectors the weight factor is optimized according to the discussion in Section 5.5.1.

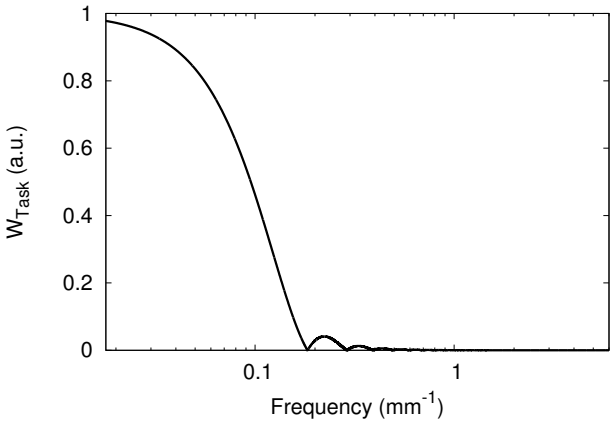

Figure 5.12: W_{task} for object absent/object present hypotheses using a nodule function of a 5mm radius tumor ($n = 1.5$).

Multilayer detector

The multilayer detector is exposed by a single exposure and the acquired images rely on the absorption of photons within the top and bottom layers, which do not have an abrupt change in absorption at the K-edge of iodine. Therefore the incident spectrum must be filtered to contain a low energy peak, below the K-edge of iodine, separated from a high energy peak, above the K-edge of iodine. This separation of the peaks is provided by the Mo or Rh spectra and can be provided by the W target spectrum once it has been filtered using a material with a K-edge near that of iodine, e.g. Rh or Ag. The SDNR, as defined in Eq. (5.53) provides the contrast (through the absolute difference of the tumor and background signals) to noise ratio of the combined image. Therefore, greater contrast and/or lower noise will yield a greater SDNR, which corresponds to a greater performance.

The use of a midfilter, or inter-detector filter, i.e. a filter between the top and bottom layers (see Fig. 4.3), in the structure of the multilayer detector was first examined using the ZSF model. Previous multilayer detector studies typically used such a filter to harden the beam between the top and bottom layers [88, 37, 85]. Hardening the beam improves the spectral separation of the LE and HE spectra, however it comes at a cost. Since the midfilter absorbs x-rays that have passed through the patient, the efficiency of the system decreases. The use of a midfilter also brings addition design and implementation complexities. To determine whether the use of a midfilter was warranted for the proposed multilayer CEM detector, the performance of a multilayer detector with and without a

midfilter was determined. The SDNR for a 1cm cubic tumor having a 1.5mg/cm^2 iodine area density was examined for the following anode/filter combinations: Rh/Rh, Mo/Rh, Mo/Mo, W/Rh, W/Al, W/Ag, W/Sn. The tube voltage for all anodes was varied from 35 to 60kVp. The detector layer thicknesses L_1 and L_2 were varied to determine the optimal detector layer thicknesses according to the following condition $L_1 + L_2 = 1000\mu$m. For the initial performance evaluation a scatter grid was not considered. All investigated midfilters were applied for each anode, but only one midfilter was used at a time. The investigated range of thicknesses for the filters [120] and midfilters [37] are summarized in Table 5.2.

Table 5.2: Filter and midfilter thickness ranges.

Type	Filter					Midfilter		
Element	Rh	Mo	Al	Ag	Sn	Cu	Mo	Ag
Thick. (mm)	0.05-0.1	0.05-0.1	0.1-3.1	0.01-0.15	0.03-0.12	0.01-0.3	0.01-0.3	0.01-0.3

The filtration, tube voltage, and conversion layer thickness which lead to the highest SDNR for each anode with and without a midfilter are tabulated in Table 5.3. Note that the Mo anode has the highest SDNR without the use of a midfilter. Midfiltration only led to a slight increase, if any, in the highest overall SDNR. Due to the marginal increase of SDNR with midfiltration, a midfilter was not used in the proposed multilayer design.

The Mo and W anodes, with Mo and Rh filtration, respectively, were found to have the greatest performance (both with and without the use of a midfilter). Since the performance of the Rh anode was the least favorable compared to the other two anodes, the Rh anode was not considered for the system optimization described in the rest of this section.

After it was determined that a midfilter was not required, the tube voltage, tube target, filtration, and photoconductor thickness were varied to maximize the performance of the multilayer detector using the ZSF model. For the multilayer detector, the following target/filter combinations were tested: W/Rh, W/Al, W/Ag, Mo/Mo, and Mo/Rh. The maximum thicknesses of the filters were determined based on the maximum product of the tube current and exposure time, i.e. mAs, allowed. The photoconductor thicknesses were limited to $L_1 = 50 - 300\mu$m and $L_2 = 200 - 1000\mu$m. Unless otherwise stated, the performance values cited were obtained using the following optimal parameters (i.e. parameters leading to the greatest performance): tube voltage, filtration, photoconductor thickness, and weight factor. For all remaining simulation results presented, a scatter grid, as discussed in Section 5.4, was assumed.

Table 5.3: Highest SDNR for a given anode with (upper) and without (lower) a midfilter.

Anode	kVp (kV)	Filter	Filter thick. (mm)	Midfilter	Midfilter thick. (mm)	L_1 (mm)	SDNR
Rh	54	Rh	0.050	Cu	0.04	0.05	95
Mo	54	Mo	0.100	-	0.00	0.05	130
W	49	Rh	0.095	Cu	0.05	0.04	124

Anode	kVp (kV)	Filter	Filter thick. (mm)	L_1 (mm)	SDNR
Rh	54.5	Rh	0.055	0.09	94
Mo	54	Mo	0.100	0.05	130
W	50	Rh	0.100	0.07	123

The spectra for different combinations of anode/filter are shown in Fig. 5.13(a). The filtration of the W spectrum using Al does not provide such a separation and thus its performance was found to be lower than that of the other target/filter combinations tested. Figure 5.13(b) shows the SDNR as a function of tube voltage for different target/filter combinations. It was found that Mo/Mo and W/Rh combinations provided the best performance. The results show that the optimal tube voltage depends on the target/filter combination and is in the range of 48-51kVp.

In the multilayer detector, the top layer serves not only to acquire the low energy image but also to harden the spectrum before it arrives at the bottom layer. Since low energy photons have a smaller penetration depth compared to high energy photons, the top layer will be thinner than the bottom layer. In addition, since the energy of the photons is greater than that used for conventional mammography the bottom layer must be relatively thick to be able to absorb a large fraction of the high energy photons. Figure 5.14 shows how the SDNR is affected by the choice of photoconductor layer thicknesses. As can be seen, a bottom layer thickness greater than 600μm is desirable and a top layer thickness of 100μm or less will lead to the greatest performance. It should also be noted that the performance is most sensitive to the thickness of the top layer.

The tube mAs is also an important factor to consider as higher mAs allows the spectrum to be further filtered to tailor the desired energy separation between high and low spectra. Figure 5.15 shows the SDNR as a function of maximum allowable mAs. For these results the dose is held constant, however the filter thickness is varied, where the maximum thickness tested leads to the desired dose using the maximum mAs, to find the filter thickness

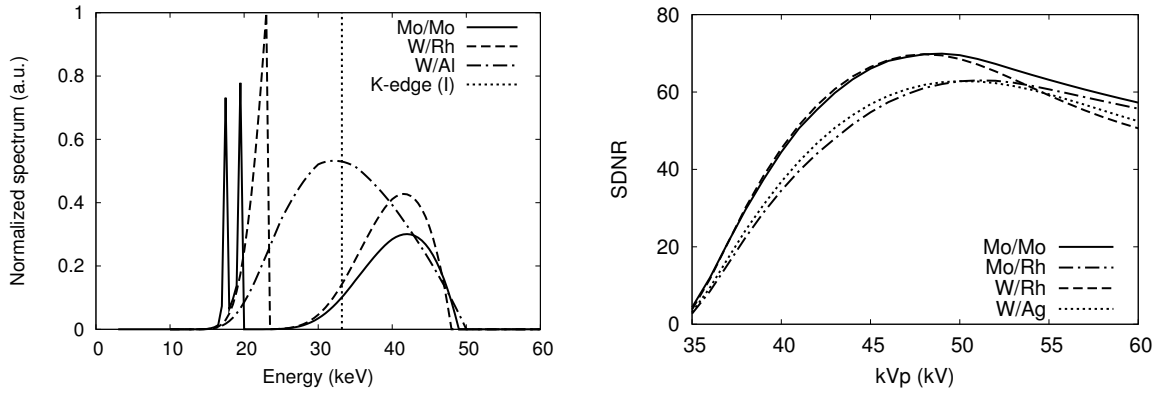

(a) (b)

Figure 5.13: (a) Normalized spectra after passing through the breast for different target/filter combinations. The vertical dotted line represents the energy of the iodine K-edge. (b) SDNR versus tube voltage for the multilayer detector with a maximum mAs of 300mAs.

that optimizes the performance. The trend for both target types show an increase in performance as the mAs is increased for low mAs values (where it is most sensitive) until the increase of performance with increasing mAs starts to flatten. At this point it can be seen that additional mAs is unnecessary, changing the performance less than 7% from 150 to 350mAs (for both detector types).

Single-layer detector

For the single-layer detector, we must consider two beams, the LE and HE beams, which are incident on the same detector but at different times. In addition to the optimization parameters determined for the multilayer detector, the relative intensity ratio was also found for the single-layer detector using the ZSF model according to Eq. (5.56). For the single-layer detector Mo/Mo and Mo/Rh target/filter combinations were tested for the low energy beam while Mo/Cu, W/Al, W/Cu, and W/Rh combinations were tested for the high energy beam. The photoconductor thicknesses were limited to $L = 50 - 1000\mu$m for the single-layer detector.

As mentioned previously, CEM requires higher energy photons than conventional mammography and relatively thick layers are required for absorbing a large fraction of the in-

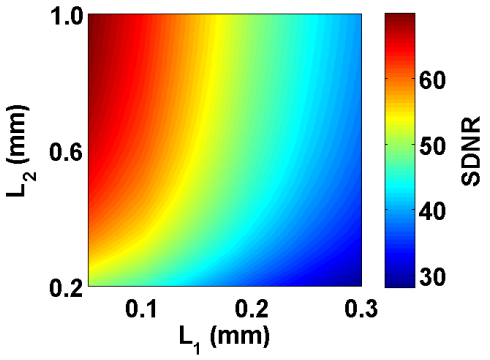

Figure 5.14: SDNR versus the photoconductor thicknesses for the multilayer detector using a 49kVp tube with Mo target and Mo filtration of 0.165mm (optimal parameters for a maximum mAs of 300mAs). L_1 and L_2 refer to the top and bottom layers of the multilayer detector, respectively.

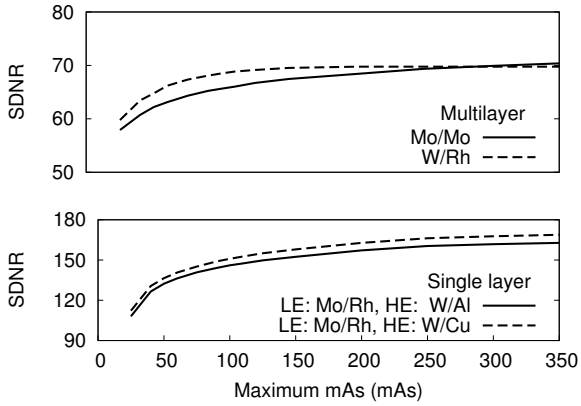

Figure 5.15: SDNR versus the maximum mAs for the multilayer detector (top) and single-layer detector (bottom). Note that the maximum mAs for the single-layer detector refers to the sum of the mAs for the LE and HE exposures.

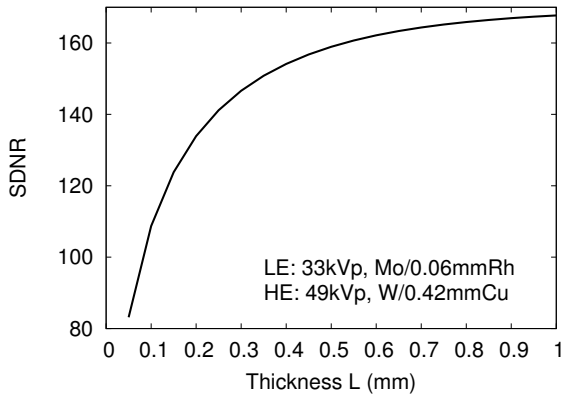

Figure 5.16: SDNR versus photoconductor thickness for the single-layer detector (tube and filtration parameters are listed in the figure inset for a combined mAs of approximately 300mAs).

cident photons. This can be seen in Fig. 5.16 where the performance is plotted against the photoconductor thickness. Once a large fraction of the incident photons are absorbed (thicknesses above about 600μm), there is relatively little change in performance. The increase in performance moving from a typical mammography detector thickness (200μm) to a thicker detector is considerable. Note that the trend shown in Fig. 5.16 is followed by all target/filter combinations tested.

The optimal combination of target/filter was found to be Mo/Rh for the low energy beam and W/Cu for the high energy beam, as can be seen in Fig. 5.17. The performance as a function of choice of low and high energy tube voltages are shown in Fig. 5.18(a) for a 1mm thick photoconductor. The choice of low energy tube voltage is optimal at 33kVp (and is relatively constant for tube voltages from 31-34kVp) and there is a rapid decrease in performance for tube voltages above this, once more photons above the K-edge are present in the low energy beam. The high energy tube voltage is found to be optimal at approximately 48-50kVp. The trend for the 1mm thick detector is similar to that of thinner photoconductors, e.g. 200μm used for conventional mammography, as can be seen in Fig. 5.18(b).

The results of the performance as a function of mAs are also shown in Fig. 5.15. Here the maximum mAs is considered to be the sum of the low and high energy mAs. As can be seen the trend is similar to that of the multilayer detector.

As discussed in Section 5.5.1, the relative intensity ratio must be considered for the single-layer detector. Figure 5.19 shows the performance as a function of relative intensity

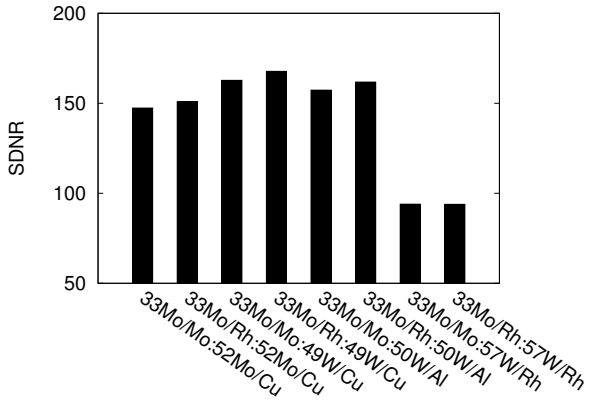

Figure 5.17: SDNR for the tested target/filter combinations for the single-layer detector (300mAs maximum). The combinations are labeled as follows: $\mathrm{kVp_L}$ $\mathrm{target_L}$ / $\mathrm{filter_L}$: $\mathrm{kVp_H}$ $\mathrm{target_H}$ / $\mathrm{filter_H}$, where the subscripts denote the corresponding exposure (LE or HE).

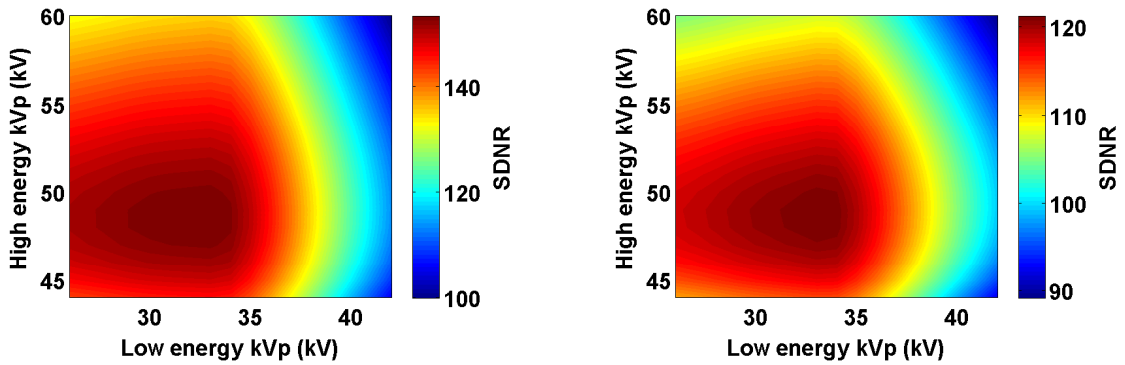

Figure 5.18: SDNR as a function of high and low energy tube voltages for the single-layer detector using (a) 1000μm and (b) 200μm photoconductor thicknesses. The filter thicknesses were held constant at 0.03mm for the Rh filter (Mo target, low energy exposure) and 0.3mm for the Cu filter (W target, high energy exposure).

ratio for two different photoconductor thicknesses. The dose ratio ($D_{g,H}/D_{g,L}$) corresponding to the relative intensity ratio is also shown. The optimal dose ratio was found to be

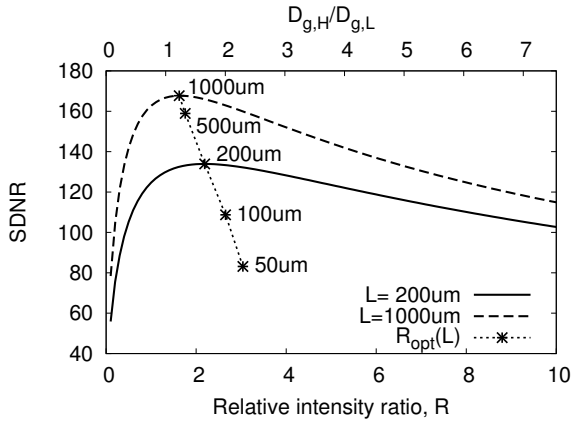

Figure 5.19: SDNR for the single-layer detector (300mAs maximum) versus relative intensity ratio, R, for $L = 200\mu$m and $L = 1000\mu$m. The tube voltages and filter thicknesses were held constant at the values that gave the optimal performance for $L = 1000\mu$m (300mAs maximum). The top axis denotes the corresponding dose ratio $D_{g,\mathrm{H}}/D_{g,\mathrm{L}}$. SDNR determined using the optimal R for various thicknesses is also shown where points and corresponding labels are used to indicate the associated thickness.

approximately 1.7 and 1.2 for 200μm and 1000μm thicknesses, respectively. The performance is thus greatest when the high energy exposure provides a higher dose to the breast, with an optimal dose ratio within 1.2-1.7 for practical detector thicknesses. The decrease in optimal dose ratio when the photoconductor thickness is increased can be explained by the following. As the photoconductor thickness is increased, a greater fraction of high energy photons are absorbed, therefore fewer high energy photons are required for the exposure. Ignoring the electronic noise for simplicity, the optimal R given by Eq. (5.65) can be used to illustrate the thickness dependence. The signal (Q) and NPS (S) are proportional (see Section 5.2.2) to the quantum efficiency, η, which represents the probability of interaction with the detector. η decreases with increasing photon energy (assuming the photoelectric effect is dominant) and/or decreasing photoconductor thickness. From Eq. (5.65), it can be seen that the optimal R is dependent on the square root of A_1/A_2, where the variables A_1 and A_2, defined in Eq. (5.64), contain fractions of the NPS over the signal squared for the high and low energy exposures, respectively. As η increases due to an increase in photoconductor thickness, A_1 and A_2 will then decrease. A_2 remains relatively constant (and reaches saturation) since a large fraction of the low energy photons are attenuated for relatively thin layers. A_1 on the other hand decreases until about 600μm where it starts to saturate. The decrease of A_1 leads to the decrease in observed optimal R.

For comparison, an effective dose ratio was found for the multilayer detector. The effective doses were found by assuming the spectrum attenuated in each layer of the multilayer detector was instead attenuated in a single-layer detector with a 1mm thick photoconductor from a separate exposure. The spectrum attenuated in the top (bottom) layer corresponded to the low (high) energy exposure. The effective dose ratio for the Mo/Mo combination (300mAs maximum) was 0.21 while it was 0.47 for the W/Rh combination. These ratios are both significantly lower than the optimal single-layer detector dose ratio and indicate that a greater fraction of the effective dose is associated with the low energy exposure. Since the number of photons attenuated in the bottom layer increases with decreasing top layer thickness, the effective dose ratio will increase with decreasing top layer thickness.

5.9.2 Multilayer and single-layer detector comparison (using SFD model)

Using the results of the previous section, the performance of the multilayer and single-layer detectors are compared using the SFD model. To gain information on the conditions where the performance of the single-layer and multilayer detectors may be comparable, the performance is examined by varying the contrast agent concentration, tumor size, and dose. The optimal spectrum from the previous section for both detectors, assuming a maximum mAs of 300mAs, was used.

For the single-layer detector, thicknesses of 200μm and 1000μm were used to obtain estimates of the low and high end of the expected performance. Similarly, thicknesses of 50μm and 200μm were used for the top layer of the multilayer detector and a thickness of 1000μm was used for the bottom layer. Unless otherwise stated the detectability was determined for a 5mm diameter tumor with a contrast agent concentration of 1.5mg/ml using a dose of 1.42mGy.

The detectability as a function of weight factor for both detectors is shown in Fig. 5.20(a). The single-layer is seen to perform significantly better than the multilayer detector (28.4 compared to 11.8). The detectability for different dose ratios is shown in Fig. 5.20(b) for the single-layer detector where a good agreement for the optimal dose ratios was found between the ZSF and SFD models (1.7 and 1.2 for 200μm and 1000μm thicknesses, respectively, using the ZSF model, which correspond to 1.7 and 1.3, respectively, using the SFD model).

The weight factors which minimized the anatomical noise were found to be in good agreement with those found using the ZSF model, as can be seen from the results in

Table 5.4: Weight factors reducing anatomical noise.

	Single-layer detector		Multilayer detector	
	ZSF model	SFD model	ZSF model	SFD model
w	0.226	0.229	0.363	0.359

Table 5.4. Note that this weight factor is independent of the imaging task considered in this work since it only considers eliminating the background in the subtracted image. It was found that the weight factor that minimized the anatomical noise was not always that which maximized the detectability. The optimal weight factor, i.e. the weight factor that led to the greatest detectability, was found to depend on many factors, including contrast agent concentration, tumor size, and dose. The impact of these factors on the detectability and weight factors for both detectors are discussed below.

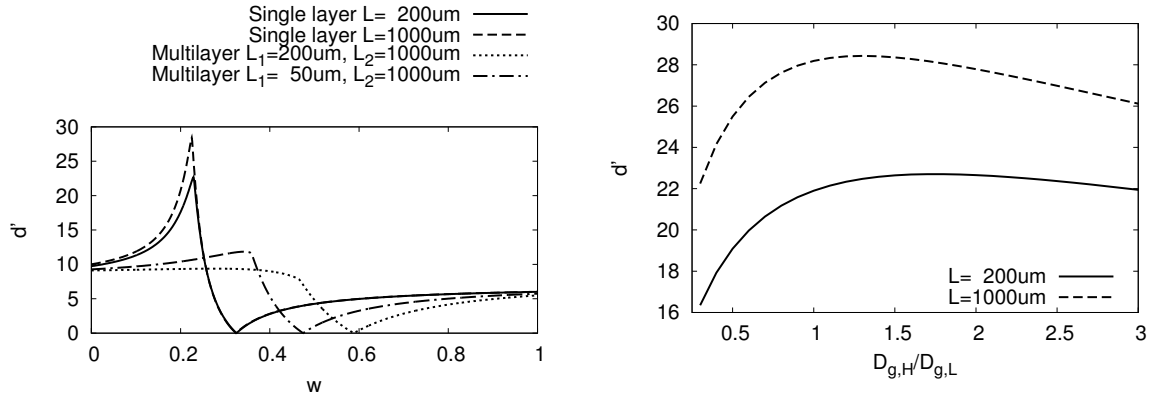

(a) (b)

Figure 5.20: Detectability as a function of (a) weight factor, w, for both detectors and (b) dose ratio for the single-layer detector.

Contrast agent concentration

Figure 5.21 shows how the detectability for the two detectors changes with contrast agent concentration, using concentrations of 0.5, 0.75, 1.0, 1.5, 2.0, 3.0, and 4.0mg/ml. The linear relation between the detectability and the concentration can be seen for the single-layer detector for all concentrations. The linearity comes from the effective increase in the

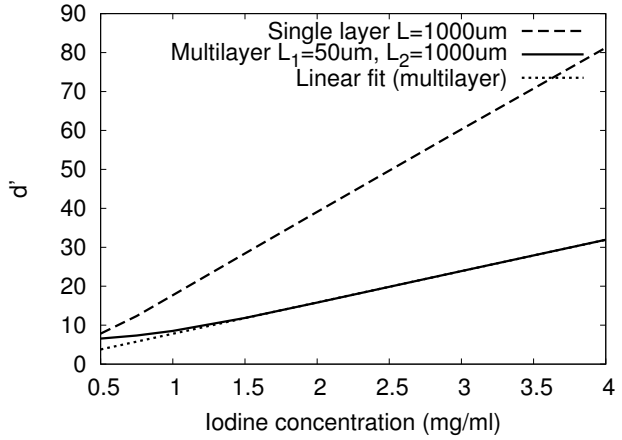

Figure 5.21: Detectability as a function of contrast agent concentration for both detectors. A linear fit is shown for the multilayer detector to better visualize the deviation from a linear relationship.

contrast thickness, which proportionally increases the subtracted contrast agent component of the contrast term, ΔI in Eq. (5.69). Note that the ΔI term contains components due to the tumor tissue and the contrast agent. For the multilayer detector, the linearity ceases for low concentrations where the contrast in the subtracted signal is heavily affected by the tumor tissue since the detector has limited spectral separation capability and has difficulty detecting such small concentration levels.

The contrast agent concentration also affects the optimal weight factor. At low concentrations, the subtraction of the tumor tissue has a greater impact on the contrast term. This in turn causes the contrast term to be smaller near the weight factor that minimizes anatomical noise and shifts the optimal weight factor to a lesser value. This effect is reduced at greater concentrations.

Tumor size

The detectability for both detectors was found using tumors having radii of 0.5, 1, 1.5, 2, 2.5, 3, 3.5, 4, 4.5, and 5mm. The results are shown in Fig. 5.22 and exhibit a quadratic dependence (except for the smallest tumors tested) since when the radius, r, is increased, the integral of the Y^2 term in Eq. (5.69) increases due to the increasing tumor area ($\propto r^2$) and the ΔI^2 term increases due to the increased tumor thickness ($\propto r^2$). Taking the square root of d'^2 from Eq. (5.69) gives the quadratic dependence. For tumor radii of 1.5mm and

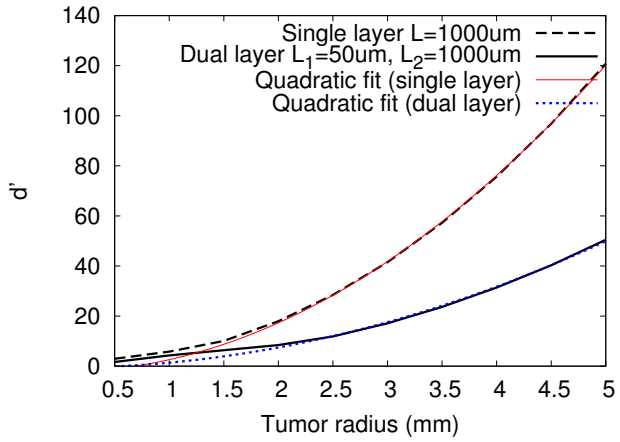

Figure 5.22: Detectability as a function of tumor radius for both detectors. Quadratic fits are shown for both detectors to better visualize the deviation from the quadratic relationship.

below, it was found that subtraction was not helpful for the multilayer detector and the optimal weight factor was zero (negative weight factors were not tested). A similar issue occurred for the single-layer detector, however only for a tumor radius of 0.5mm.

When the tumor is small, the high frequency components of the resulting task function have greater weighting. Since the anatomical noise dominates the low frequencies, it is not always optimal to reduce the anatomical noise to a minimum. In this case the shift in optimal weight factor is due to the increased contrast of the tumor at lower absolute weight factors compared to the contrast at the weight factor that minimizes the anatomical noise. For relatively large tumors, the low frequency components become more important and thus it becomes more important to reduce the anatomical noise, making the optimal weight factor close to the weight factor that minimizes the anatomical noise.

Dose

The effect of dose on the detectability is shown in Fig. 5.23. At high doses, the quantum noise is reduced and the anatomical noise becomes increasingly important. This effect shifts the optimal weight factor closer to that of the weight factor that minimizes anatomical noise. As the anatomical noise is minimized, the detectability is proportional to the square root of the dose, indicating that the quantum noise is dominant. At low doses, quantum noise is significant and the optimal weight factor is no longer at the weight factor

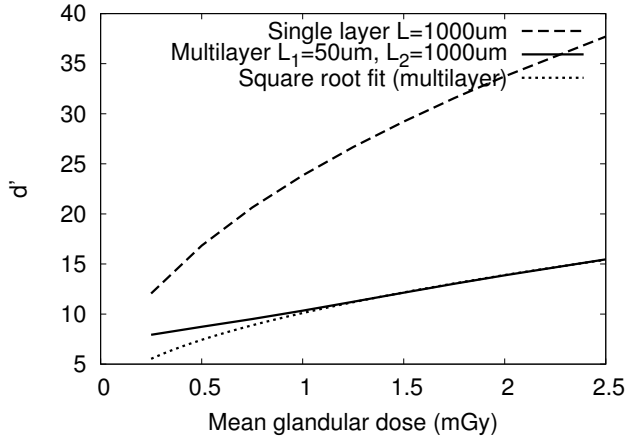

Figure 5.23: Detectability as a function of dose for both detectors. A square root fit is shown for the multilayer detector to better visualize the deviation from a square root relationship. The deviation of the single-layer detector performance from a square root dependence is not readily visible with the inclusion of a fit (not shown) as there is only a slight deviation at the lowest dose tested.

that minimizes anatomical noise, but instead is at a weight factor where the contrast is greater and both anatomical noise and quantum noise are significant. This is why the square root dependence is no longer seen at low doses. The single-layer detector not only provides greater contrast, but it also yields significantly less quantum noise compared to the multilayer detector.

5.10 Discussion

From the simulations it was found that the multilayer detector had comparable performance with and without the use of a midfilter. The midfilter was therefore not considered in the multilayer design. The Mo/Mo and W/Rh combinations were found to provide comparable performance for the multilayer detector. The optimal tube voltage was in the same range as the tube voltage for the (single-layer detector) high-energy exposure. The optimal top and bottom layer thicknesses were found to be 50μm and 1000μm, respectively. For the single-layer detector, Mo/Rh (low energy) and W/Cu (high energy) were found to be the optimal target/filter combinations and it was found that thicker layers provided greater performance. The optimal kVp for both the LE and HE exposures were greater than those

Table 5.5: Optimal parameters for single-layer and multilayer detectors (300mAs maximum).

Single-layer detector						
HE kVp (kV)	HE target/filter	LE kVp (kV)	LE target/filter	L (μm)	$D_{g,HE}/D_{g,LE}$	w
49	W/Cu	33	Mo/Rh	1000	1.2	0.226

Multilayer detector				
kVp (kV)	target/filter	L_1 (μm)	L_2 (μm)	w
49	Mo/Mo	50	1000	0.363

found by Puong *et al* [20] for weighted log subtraction. The difference may be due to differences in the attenuation characteristics for the conversion materials a-Se (used in this work) and CsI (used by Puong *et al*), where Cs (cesium) and I (iodine) have K-edges at 36.0 and 33.2keV, respectively. The use of Rh/Rh, where Rh has a slightly greater K-edge than Mo, for the LE exposure might also have lead to different optimal kVp values. For the single-layer detector it was found that the optimal dose ratio was greater than unity, which agrees with previous studies (e.g. Carton *et al* [17] where weighted log subtraction was used, and Puong *et al* [127] where an image chain recombination algorithm was used). The optimal parameters found using the ZSF model for both detectors are summarized in Table 5.5.

The multilayer detector proposed in this research has two stacked detectors (shown in Fig. 4.3) although other architectures may be possible. The proposed design requires additional costs compared to the single-layer detector due to the additional detector. Although scatter from the top detection layer may affect the signal acquired in the bottom layer, this effect is assumed to be negligible since the photoelectric effect contributes to a large fraction of the total attenuation. As an example, $\alpha_{photoelectric}/\alpha_{total}$ is found to be around 89% (α is the attenuation coefficient) at the highest photon energy considered in this study (60keV) and corresponds to the worst case. Aside from primary photons being scattered, the K-fluorescent photons generated in the top layer may also lead to unwanted signal generation in the bottom layer.

The advantage of the proposed multilayer design in addition to simultaneous image acquisition to reduce motion artifacts, is that it leverages existing commercial thin-film transistor a-Se detectors. Alternatively, both images (high and low energy) may be acquired simultaneously from a single exposure using a photon counting detector with a threshold at the K-edge of iodine. The threshold is used to split the spectrum into low and high energy spectra [59]. Acquiring both images simultaneously through photon counting spectral separation using a large area detector is challenging due to the manufacturing complexity associated with building a large area CMOS backplane containing pixel level

photon counting circuits [128].

Other methods for acquiring both images simultaneously use a slot scanning detector and either acquire the images by differential filtering of the incident beam where a certain number of detectors acquire the LE image while the others acquire the HE image [17] or spectral separation using thresholding [22]. Slot scanning detectors have the advantage of being quantum noise limited and have increased scatter rejection however there is increased loading on the x-ray tube and a longer scan time [75, 17].

Considering a-Se as a conversion material, single-layer and multilayer detectors for CEM were evaluated. The system parameters leading to the greatest performance for both detectors were determined from a study over a wide range of parameters. For the multilayer detector, Mo/Mo and W/Rh target/filter combinations with tube voltages in the range of 48-51kVp were found to perform the greatest. The performance was most sensitive to the top layer detector thickness. For the single-layer detector, a combination of Mo/Rh at a tube voltage of 33kVp for the LE spectrum and W/Cu at a tube voltage of 49kVp for the HE spectrum was found to be most suitable. It was also found that single-layer detectors can benefit greatly from photoconductor thicknesses thicker than those used in conventional mammography. The most favourable dose ratio was found to be in the range of 1.2-1.7, depending on the photoconductor thickness.

The performance comparison of the two detectors indicated that the single-layer detector outperformed the multilayer detector, with a peak detectability greater by a factor of 2.4 for a 2.5mm radius tumor having a contrast agent concentration of 1.5mg/ml. For three factors investigated, namely contrast agent concentration, tumor size, and dose, the detectability was found to be most comparable between the detectors at the lower end of the evaluated factors. The single-layer detector not only led to better contrast, due to its greater spectral separation capabilities, but also had lower quantum noise. If either or both of these issues could be addressed by extending the multilayer detector considered in this work, it would be of great benefit. The strength of the multilayer detector is the elimination of motion artifacts, here assumed to be negligible. For a further comparison of the detectors described in this work, the motion artifacts present in dual-exposure CEM must be quantified and included as part of the resulting noise in the image. The inclusion of motion artifacts in the analysis will be discussed in Chapter 7.

Chapter 6

Experimental validation

6.1 Introduction

The objectives of the experimental studies were to validate the theoretical models for both the multilayer and single-layer detectors using prototype detectors. Similar to the theoretical investigation, a-Se was used as the conversion material for the prototype detectors. The single-layer detector is a conventional flat panel detector using direct or indirect conversion methods to convert the incident x-rays into collectable charge. The multilayer detector includes two of such detectors stacked on top of each other. To further harden the beam between the top and bottom layers, it is also possible to place an additional filter (e.g., copper [88]) between the top and bottom layers, however as found in Chapter 5 additional filtration is not needed for CEM. The contrast of both detectors for different amounts of contrast agent were measured and compared to theoretical results for model validation.

6.2 Experimental method

The experimental setup is shown in Fig. 6.1, which will be described in more detail below. Both the single-layer and multilayer detectors were tested using an iodinated contrast agent. For the multilayer detector, 200 and 1000μm thick single pixel a-Se detectors (Anrad corporation) were used for the top and bottom layers respectively. Although it had previously been found (Chapter 5) that a thin top layer ($\sim$ 50μm) would provide better performance, a 200μm detector was used since it is a standard thickness for mammography and is thus readily available. The same (200 and 1000μm) detectors were used for the

single-layer detector experiments. Conventional a-Se flat panel detectors are designed with an attenuating backplane glued to the glass under the thin-film transistors (which would attenuate most x-rays passing through the top-layer of a multilayer detector). It is not practical to remove the backplane and for this reason it was decided that single pixel detector samples would be used for the prototype detector. These detector samples are fabricated using the same *n-i-p* a-Se layers in conventional a-Se flat panel detectors [129]. The signals were read from the detectors by subtracting the dark current from the x-ray current. The detectors used for the experiments are shown in Fig. 6.2 in a multilayer configuration.

The 200 and 1000μm detectors were biased at 10 and 6V/μm respectively. An applied field of 10V/μm is typical for a-Se detectors, however the bias voltage was limited by our high voltage power supplies (Canberra 3106D and Stanford Research Systems PS350) to 6000V. High biases are desirable in a-Se detectors since the ionization energy (i.e., energy required for generation of a detectable electron-hole pair) decreases with increasing electric field [130]. The signals from the detectors were amplified using a low-noise current amplifier (Ametek 5182) and read out from an oscilloscope.

It should be noted that the 200μm detector was hole collecting (top contact biased positive) while the 1000μm detector was electron collecting (top contact biased negative) due to the configuration of the *n* and *p* blocking layers ([131]) of the detectors with respect to the top and bottom electrodes (see Fig. 6.3). Electrons have relatively poor mobility in a-Se compared to holes and electron trapping can become significant especially at low electric fields.

The incident spectra (i.e., tube kVp, filtration) were chosen to optimize the signal difference to noise ratio (SDNR) according to Section 5.5 using the available a-Se detectors described above. For the single-layer detector, the spectra were optimized for the 1000μm detector. A Gulmay 3150 x-ray unit having a W anode was used to expose the detectors, which was also considered when determining the spectra. In the case of the multilayer detector, an additional incident spectrum with a filtration material (Mo) different from the optimal spectrum (Ag) was used to further test the detector. The tube and filter settings are summarized in Table 6.1 where the filtration material for the single-layer is seen to be the same for both LE and HE exposures (Al). The simulated spectra for the different tube settings are shown in Fig. 7.4.

The breast phantom was constructed using a polymethyl methacrylate (PMMA) cylinder having a base thickness of 23.8 mm and filled with olive oil to achieve a total thickness of 45 mm to emulate a 4.5 cm thick, 50% glandular breast. As in previous CEM studies [22, 16], PMMA and olive oil were used since their difference in attenuation coefficients

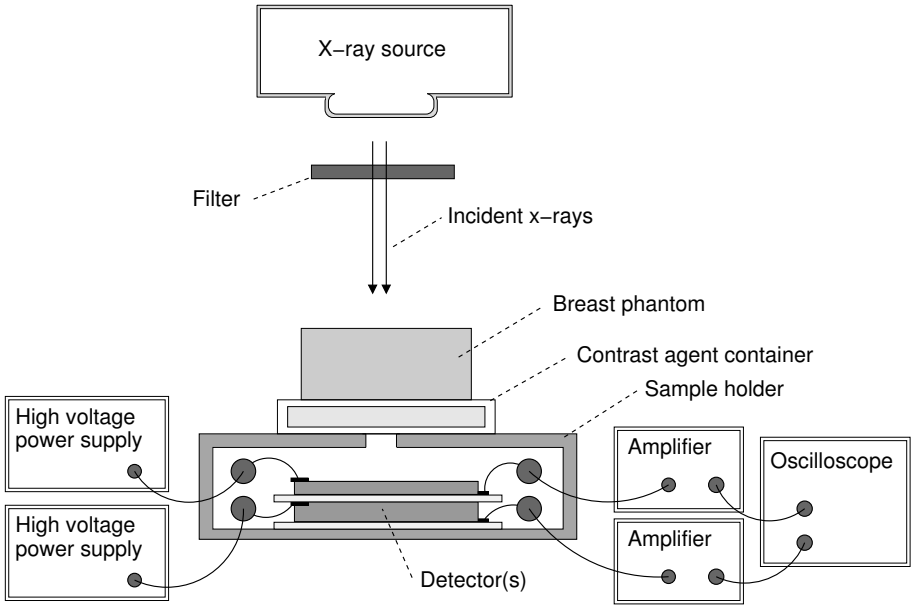

Figure 6.1: Experimental setup. For the single-layer experiments only a single high voltage power supply and a single amplifier were used.

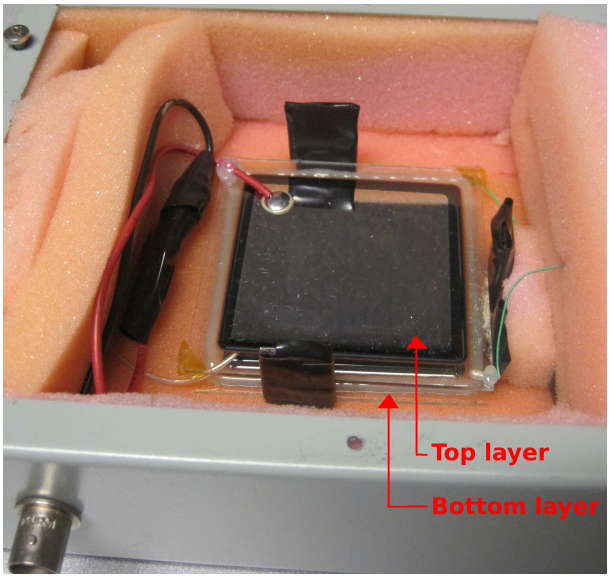

Figure 6.2: Detectors used for experiments in multilayer detector configuration. The bottom layer is almost entirely obscured by the top layer.

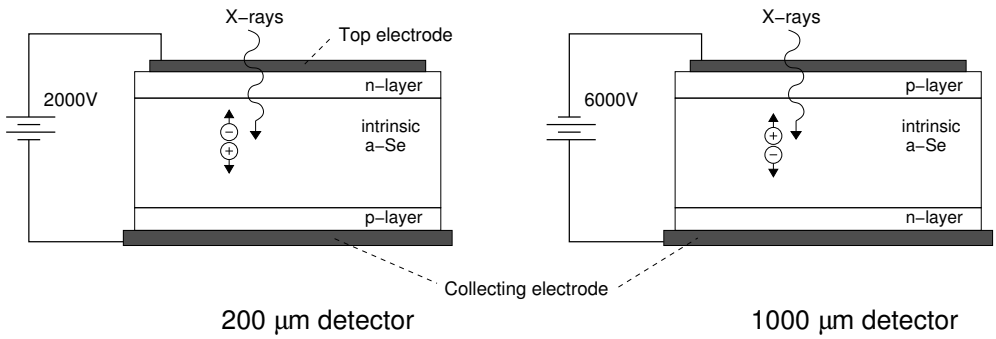

Figure 6.3: Biasing configuration of the 200μm and 1000μm thick detectors (not to scale).

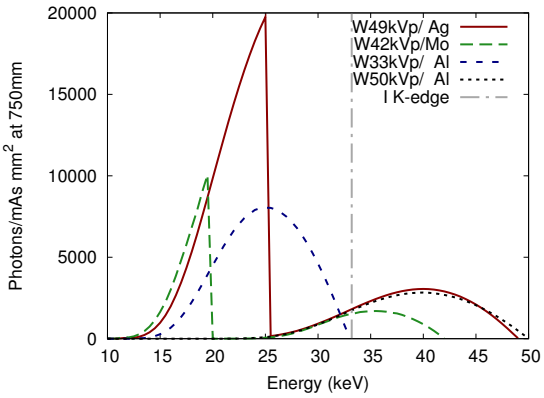

Figure 6.4: Simulated spectra for different tube/filter combinations. The iodine K-edge energy is also denoted for comparison purposes.

Table 6.1: Tube, filter, and image combination settings. The superscripts a and b refer to the 200μm and 1000μm detectors, respectively.

Detector	Beam	Tube voltage (kVp)	Filter material	Filter thickness (mm)	w
Multi	LE, HE	49	Ag	0.1	0.484
Multi	LE, HE	42	Mo	0.127	0.650
Single	LE	33	Al	2.5	0.42^a, 0.41^b
Single	HE	50	Al	13	-

match well with the difference of glandular and adipose tissues in the breast. The contrast agent (Omnipaque 180 mg I/ml, GE Healthcare, Mississauga, ON, Canada) was diluted in water in a separate container. Different containers were used for each concentration. Concentrations ranging from 0.7 mg/ml to 5.6 mg/ml were tested assuming a 10 mm thick tumor, where iodine concentrations of 3 mg/ml are feasible for tumor uptake [22]. It should be noted that due to the heavy patient load on the cancer center's therapy x-ray unit each set of experiments was conducted on a different day, meaning different poured and mixed contrast agent containers were used.

Once the HE and LE signals were measured using the different contrast agent concentrations, the dual-energy (DE) signal was obtained using logarithmic subtraction:

$$I_{\mathrm{DE}} = \ln(I_{\mathrm{H}}) - w \ln(I_{\mathrm{L}}) \tag{6.1}$$

An optimal weight factor was chosen to minimize the anatomical noise due to variation in glandular tissue within the breast as described in Section 5.5.

The HE and LE signal measurements were repeated to obtain a total of three measurements of HE and LE for each concentration. The observed contrast, C, for the different iodine concentrations was then obtained by subtracting the DE signal through the contrast agent by the DE signal through the background (container with no contrast agent):

$$C = I_{\mathrm{DE},b} - I_{\mathrm{DE},c} \tag{6.2}$$

where c and b denote signals from exposures that contain contrast agent and those that do not (background), respectively.

6.3 Modeling

The cascaded detector model described in Section 5.2.2 was used to model the detectors. Since the detector prototypes were single pixel detectors, the zero spatial frequency cascaded model was used. The performance of the detectors was evaluated using the signal

difference to noise ratio (SDNR). Note that the signal difference referred to in the numerator of the SDNR, Eq. (5.53), also refers to the contrast in Eq. (6.2). The optimal intensity ratio for the single-layer detector was determined by maximizing the SDNR, as described in Section 5.5.1.

The exposed breast was assumed to be made of 50% glandular tissue, having a skin thickness of 4 mm and a total thickness of 45 mm. The tumor was assumed to be 10 mm thick and, to be consistent with the experiment, was comprised of a combination of 50% glandular tissue and iodine corresponding to the contrast agent concentration used. The mean glandular dose to the breast chosen to be 1.42mGy for spectra optimization to be consistent with a previous dual-energy single-layer detector CEM clinical study [11]. The maximum product of the tube current and exposure time for both detectors was assumed to be 300mAs. A tungsten anode was assumed for the x-ray source due to the availability of a tungsten source for measurements. Al, Ag, and Mo filters were considered to filter the beam since they were shown in Chapter 5 to provide good performance for a tungsten anode. Due to Al filters being readily available, an Al filter was also used for the LE beam for the single-layer detector. The configuration of a tungsten anode for the LE beam was not part of the theoretical optimization presented in Chapter 5. However the anode/filter combination of W/Al for the LE beam was found to provide comparable performance to the optimal configurations found in Chapter 5.

6.4 Results

The 200μm and 1000μm detectors were first examined under dark conditions (results shown in Fig. 6.5). The dark current of a-Se is widely known to decrease over time [129], which agrees with our observations from the dark current of the two tested detectors. In addition to the requirement of stable dark current, the x-ray current and the difference between the dark current and x-ray current must also remain stable. To reduce the amount of variations in the measurements and achieve consistent measurement readings, the detectors were allowed to settle (i.e., biased) for approximately an hour before being exposed to x-rays.

Initially the multilayer detector experiments were run by biasing one layer (either the top LE or bottom HE layer) at a time since only one low-noise high-gain (10^8V/A) amplifier was available. The heavy patient load on the cancer centre's therapy x-ray unit, the length of the time required for the measurements, and the availability of a single low-noise high-voltage power supply lead to acquiring the LE and HE signals on different days. Since the LE and HE signals must be subtracted, any small differences of these signals can lead to significant differences in the subtracted signal. The experimental and simulation

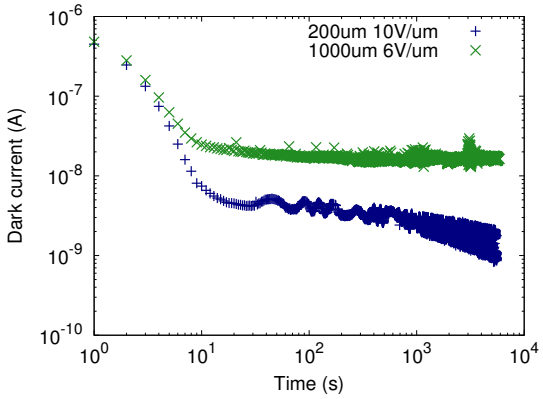

Figure 6.5: Dark current of the 200μm and 1000μm thick detectors under applied bias. The active area of the detector is approximately 5.2 $\times$ 5.2 cm^2.

results for the two multilayer detector configurations tested are shown in Fig. 6.6. Linear fits for both the experimental and simulation results are also shown. Ideally the contrast should increase linearly with increasing contrast agent concentration. Good agreement is seen between the simulation and experimental results, especially at lower concentrations. Interestingly, the greatest deviation between experimental and simulation results occurred at the highest concentration for both filters. It is believed that one of the reasons leading to differences in the experimental and simulation results (for both the Mo and Ag filters) is due to the acquisition of the LE (200μm) and HE (1000μm) signals on different days. This led to the use of different contrast agent containers (poured and mixed on different days) and may have led to further variations in the setup.

To better verify the operation of the multilayer detector, another low-noise high-gain amplifier was purchased so that both layers (top and bottom) could be biased and readout simultaneously. The results for the simultaneous readout multilayer detector configurations are shown in Fig. 6.7. The data is seen to have better agreement with the expected values compared to Fig. 6.6. The configuration using the Mo filter (Fig. 6.7, left) was expected to have less contrast than the configuration using the Ag filter (Fig. 6.7, right), which is confirmed by the experimental results. Good agreement is seen between the simulation and experimental results and the results demonstrate the successful operation of the multilayer detector for CEM imaging.

The simulation and experimental results for the single-layer detector are shown in Fig. 6.8. Again good agreement is seen between the experimental and simulation results. The single-layer detector LE and HE signals were acquired on the same day which is

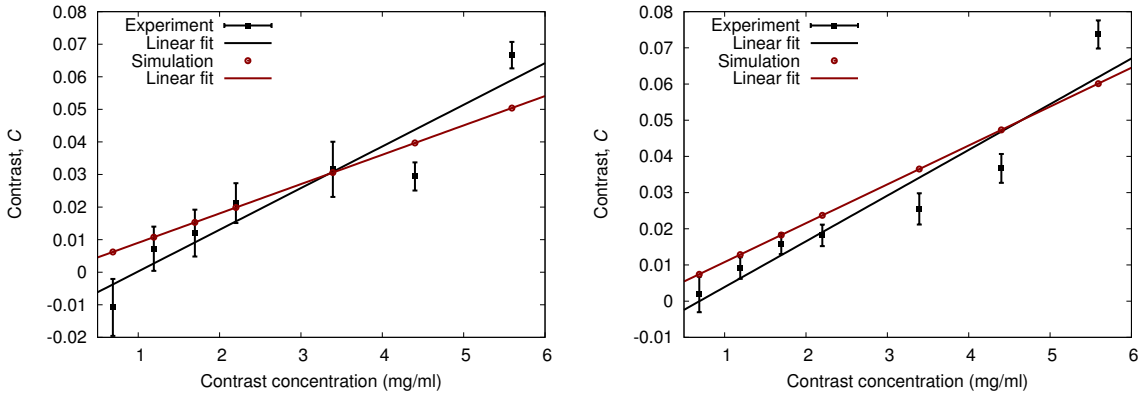

Figure 6.6: Contrast as a function of contrast agent concentration for initial experimental and simulation results for the multilayer detector using (left) Mo and (right) Ag filters. Linear fits are also shown.

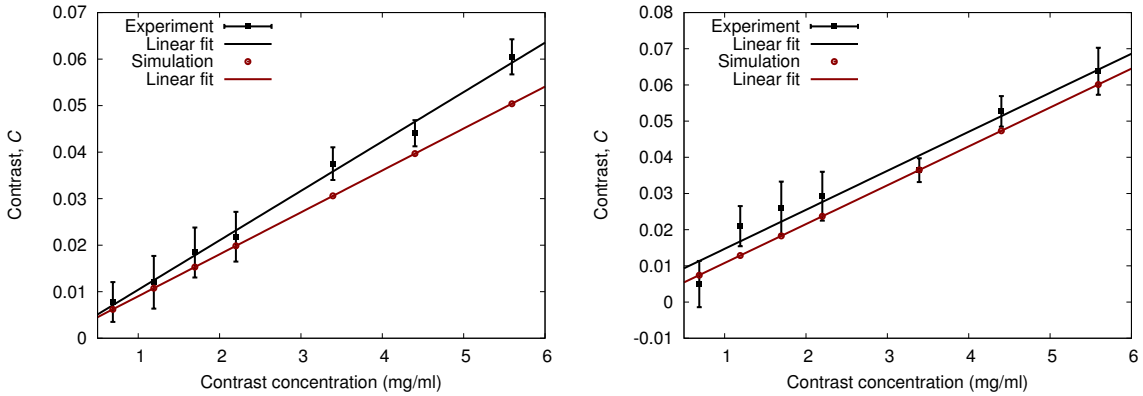

Figure 6.7: Contrast as a function of contrast agent concentration for simultaneous acquisition experimental and simulation results for the multilayer detector using (left) Mo and (right) Ag filters. Linear fits are also shown.

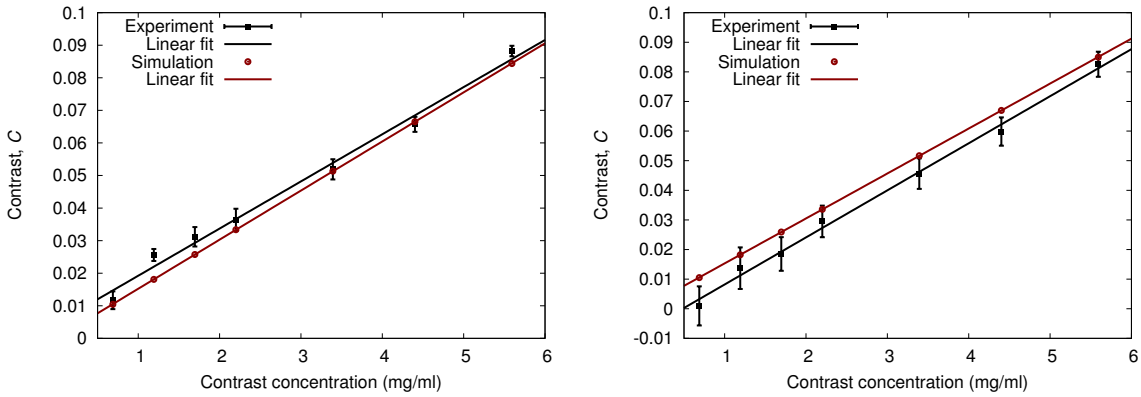

Figure 6.8: Contrast as a function of contrast agent concentration for experimental and simulation results for the single-layer (left) 200μm and (right) 1000μm thick detectors using Al filters (as listed in Table 6.1). Linear fits are also shown.

believed to be why there is less deviation between the experimental and simulation results compared to the initial multilayer detector results (Fig. 6.6). Greater variations in the detector response were observed for the 1000μm detector, compared to the 200μm detector, as can also be deduced from comparing the standard errors of the mean in Fig. 6.8.

To facilitate the comparison between the measured results, the measured contrast for all four detector configurations are shown in Fig. 6.9. It should be mentioned again that the layer thicknesses used in the experiments for the multilayer detector were found to be sub-optimal from the SDNR simulation analysis. However the thickness of 1000μm for the single-layer detector was found to be optimal (again, from simulations). The possible performance improvements using the optimal detector configuration for the multilayer detector are shown in Fig. 6.10. In addition, the performance could be improved using an alternative tube anode material (e.g., Mo as discussed in Section 5.9, also shown in Fig. 6.10). The SDNR of the single-layer detector is greater than that of the multilayer detector (see Fig. 6.10) due to its greater spectral separation capabilities (leading to better contrast) and its greater control of LE and HE beam intensities (leading to lower quantum noise). Although the SDNR of the multilayer detector is lower than that of the single-layer detector, its strength is in reducing motion artifacts, which is a parameter not taken into account in the evaluation of SDNR. Quantifying the impact of motion artifacts on image quality is discussed in Chapter 7.

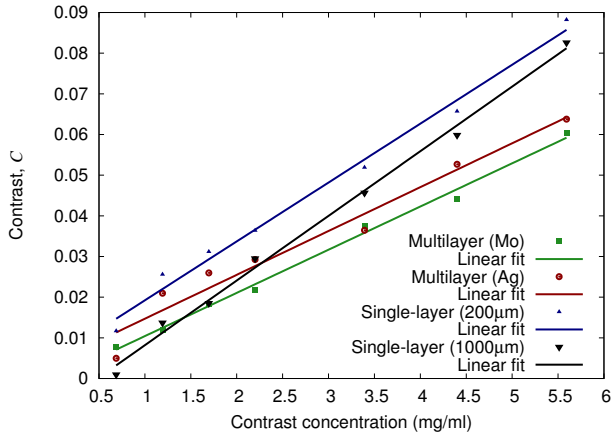

Figure 6.9: Experimentally obtained contrast as a function of contrast agent concentration for the four detector combinations tested: multilayer (Mo and Ag filters, simultaneous acquisition) and single-layer (200μm and 1000μm thick).

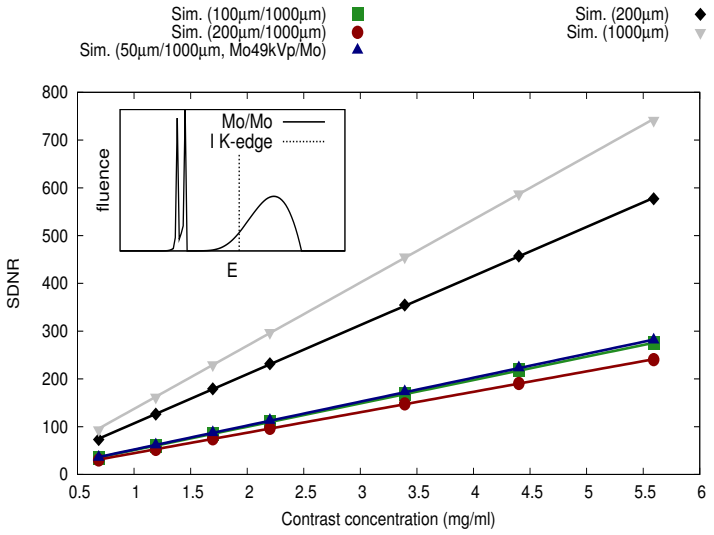

Figure 6.10: SDNR for multilayer thicknesses of 100μm/1000μm (optimal, 50kVp, 0.1mm Ag, $w = 0.500$) and 200μm/1000μm (used for experiments) using a tungsten anode and Ag filter. Also shown is the SDNR for multilayer layer thicknesses 50μm/1000μm (optimal) using a Mo anode and Mo filter (49kVp, 0.165mm Mo, $w = 0.365$). Inset shows the Mo/Mo spectrum after passing through the breast. SDNR are also shown for single-layer thicknesses of 1000μm (optimal, used for experiments) and 200μm (used for experiments) using a tungsten anode and Al filters.

6.5 Discussion

Experimental and theoretical results on multilayer detectors for CEM imaging were presented and good agreement was found between the two. The technology used in the experiments is based on that used for commercial large area flat panel imagers. The results suggest that CEM imaging using a large area multilayer detector is a feasible technology for reducing motion artifacts. In addition to the multilayer detector, a single-layer detector was studied and good agreement was found between the experimental and theoretical results thus validating the theoretical models. The single-layer detector benefits from better spectral separation capabilities, leading to greater contrast as seen in the presented results, however the combined image is prone to motion artifacts. The choice of detector hinges on the application and its sensitivity to motion artifacts, e.g. 3D contrast-enhanced digital breast tomosynthesis.

Chapter 7

Effect of motion on image noise and performance

7.1 Introduction

The objectives of the motion artifact studies were to estimate the effect of motion on anatomical noise in combined image, use clinical CEM images to further validate theoretical models, determine how motion impacts tumor detectability, and to determine how the performance of the single-layer detector compares to the multilayer detector once the motion artifacts have been taken into account.

As previously mentioned, one of the drawbacks of dual-energy imaging using two exposures with a single-layer detector is that motion artifacts may appear in the combined image [71, 31]. These artifacts exist due to the anatomical motion (e.g., caused by cardiac, respiratory, or patient movement) that occurs within the time between exposures when multiple exposures are required to acquire both images.

Motion artifacts in CEM images acquired using temporal subtraction (having pre- and post-contrast images) have been reported as requiring typical corrections in terms of displacements (i.e. shifts) or rotations in the range of 200-300 μm and 1-2°, respectively, and in some instances, corrections up to 8 mm were required [10, 69, 132]. Although the effect of patient motion is lessened for the dual-energy subtraction compared to the temporal subtraction method due to the shorter inter-acquisition time, motion artifacts are still present. Even though the performance of single-exposure strategies has been compared to the performance of dual-exposure techniques [133], the comparison is lacking the inclusion

of motion, which is the one of the main benefits of the simultaneous image acquisition strategies, thus rendering the comparison incomplete. A method has been proposed to measure the effect of simple linear motion using a phantom [134], however there is limited applicability of this method to complex motion and to system design or performance and noise analysis prior to having the detector in hand.

In this chapter a method is presented that includes motion artifacts in the noise and performance analysis. The effect of motion artifacts on the anatomical noise in the combined image and on the ideal observer detectability are quantified for a CEM system using dual-energy subtraction. Image acquisition for the dual-energy subtraction scheme studied consists of acquiring the LE and HE images separately using two exposures [11]. The anatomical noise, including the effect of motion artifacts, is taken into account using an extended cascaded systems model. To validate the model, the noise power spectra from the model are compared against noise power spectra of clinical images from a previous dual-energy CEM clinical study [11]. The model is then used to estimate the effect of motion on tumor detectability. The described model could be used for a more comprehensive performance analysis of dual-exposure techniques (such as dual-energy or temporal subtraction) and allow for a fairer comparison of dual-exposure and single-exposure techniques.

7.2 Materials and methods

7.2.1 CEM signal and noise

The methodology for including motion in the analysis leverages the models presented for the SFD model in Section 5.6. The combined CEM image is obtained using a weighted combination of the LE and HE images.

For analysis, the noise of the combined image can be separated into detector noise (which comprises quantum and electronic noise) and anatomical noise (i.e. structural noise of the object). The noise power spectrum (NPS) of the combined image, similar to the NPS of each individual (LE and HE) image, can be written as:

$$\mathrm{NPS_C}(u,v) = \mathrm{NPS_{D,C}}(u,v) + \mathrm{NPS_{B,C}}(u,v), \tag{7.1}$$

where the subscript B refers to the anatomical noise and $\mathrm{NPS_{D,C}} = \mathrm{NPS_{Q,C}} + \mathrm{NPS_{E,C}}$ where subscripts Q and E refer to the quantum and electronic noise, respectively, and D refers to the detector noise. The detector noise of the combined image is given by [96]:

$$\mathrm{NPS_{D,C}}(u,v) = \mathrm{NPS_{D,H}}(u,v) + w^2\mathrm{NPS_{D,L}}(u,v). \tag{7.2}$$

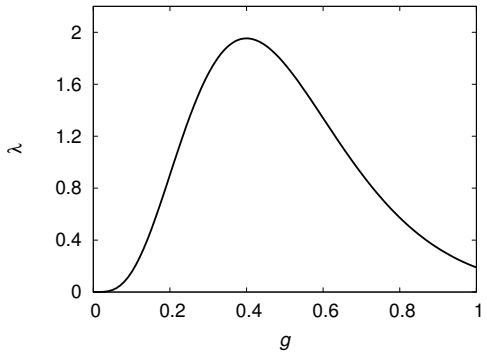

Figure 7.1: Glandularity distribution.

As in Eq. (5.68), typically the anatomical noise term is written as $\mathrm{NPS_{B,C}} = \mathrm{NPS_B MTF^2}$ where MTF is the modulation transfer function of the system and is included to account for the effect of the imaging system on the variation of the background, which is independent of the imaging system [96, 62].

7.2.2 Anatomical noise

The anatomical noise is the same as that presented in Section 5.6, however the glandularity distribution was modified to better model a realistic breast to coincide with the measured glandularity distribution reported in a recent study [135]. The expectation value in Eq. (5.72) was determined according to [22]:

$$\left\langle \left| \frac{dI}{dg} \right|^2 \right\rangle = \int \left| \frac{dI}{dg} \right|_g^2 \lambda_g dg \tag{7.3}$$

where λ_g is the glandularity probability density function. A skewed glandularity distribution was used [135] and modeled with a gamma distribution having a 50% mean glandularity (Fig. 7.1).

7.2.3 Image and motion filters

To introduce motion in the analysis the use of two additional linear shift invariant filters (in each image branch) were considered, as schematically shown in Fig. 8.1. The 'M' filter (object filter) is used to emulate motion in the background tissue from one image

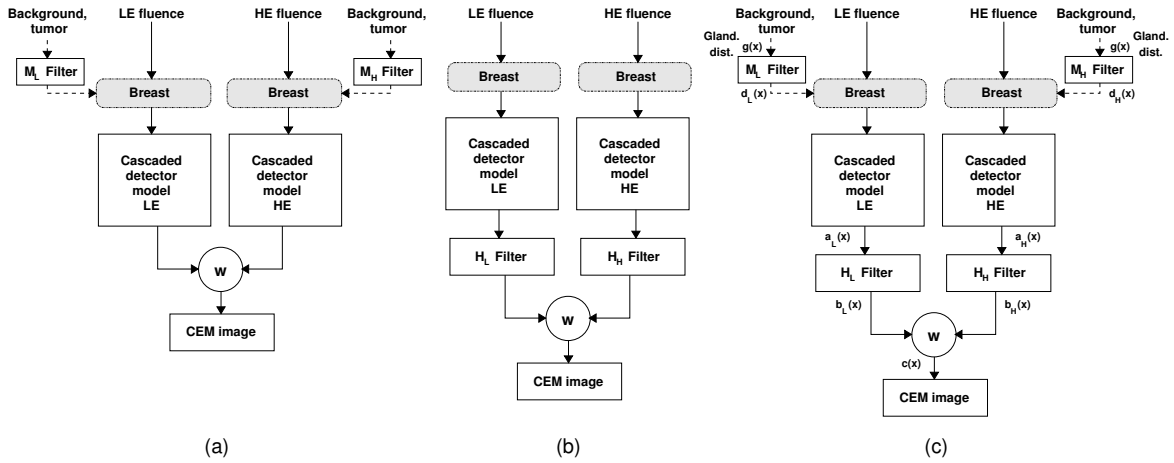

Figure 7.2: Schematic of CEM image formation for (a) the motion model, (b) the clinical image comparison model, and (c) both (used for derivation). The dashed lines represent changes to the object.

acquisition to the next. This filter is therefore applied (i.e., is not a delta function) to only one of the backgrounds, either the LE or HE background, whichever is acquired last. Since the 'M' filter affects the background, it is applied to the glandularity, $g(x)$. Filtration of the background will only affect the anatomical noise and does not affect the mean signal intensity or detector noise.

The 'H' filter (image filter) represents a filter applied after the image is acquired by the x-ray detection system and is mainly used for model verification. The main caveat of using the 'H' filter to model motion is that in addition to affecting anatomical noise this filter also affects detector noise. The 'H' filter is much like the low-pass filters occasionally applied in dual-energy imaging to reduce high frequency quantum noise [136, 21].

The anatomical background is assumed to be stationary and independent of the signal amplitude, and the detector NPS and anatomical NPS are treated separately [137, 138]. Since the detector NPS is unaffected by the 'M' filter, the combined image detector NPS is the sum of the filtered NPS from the LE and HE images [60, 21]:

$$\mathrm{NPS}_{\mathrm{D,C}}(u,v) = |H_{\mathrm{H}}(u,v)|^2 \mathrm{NPS}_{\mathrm{D,H}}(u,v) + w^2 |H_{\mathrm{L}}(u,v)|^2 \mathrm{NPS}_{\mathrm{D,L}}(u,v), \tag{7.4}$$

where $H_i(u,v)$ is the Fourier transform of the 'H' filter, $h_i(x,y)$.

The anatomical noise is affected by both the 'M' and 'H' filters. Here the effect of the 'M' and 'H' filters on the anatomical noise of the combined image is derived (refer to

Fig. 8.1 for glandularity and image signal symbols at the different stages). For determining the anatomical NPS the application of motion ('M' filter) to the glandularity is looked at first:

$$d_i(x) = g(x) * m_i(x), \tag{7.5}$$

where $*$ represents the convolution and i can represent either the LE or HE path. Note that the formulation of the anatomical NPS will be presented in one dimension, which can then be extended to two dimensions. The autocorrelation of $d_i(x)$ is given by:

$$K_{d_i}(\xi) = \left\langle \int \int m_i(\tau) g(x-\tau) m_i^*(\tau') g^*(x-\tau'+\xi) d\tau d\tau' \right\rangle, \tag{7.6}$$

where the superscript $*$ denotes the complex conjugate and the expectation value is taken over x. The autocorrelation of $g(x)$ can also be written [62]:

$$K_g(\xi - \tau + \tau') = \langle g(x+\xi-\tau) g^*(x-\tau') \rangle . \tag{7.7}$$

Using the above equation, the autocorrelation of $d_i(x)$ can be rewritten as:

$$K_{d_i}(\xi) = \left\langle \int \int m_i(\tau) K_g(\xi - \tau + \tau') m_i^*(\tau') d\tau d\tau' \right\rangle . \tag{7.8}$$

Using the following relation [139]:

$$\int \int m(\tau) K_g(\xi - \tau + \tau') m^*(\tau') d\tau d\tau' = m(\xi) * K_g(\xi) * m^*(-\xi), \tag{7.9}$$

we can write the autocorrelation of $d_i(x)$ as:

$$K_{d_i}(\xi) = m_i(\xi) * K_g(\xi) * m_i^*(-\xi). \tag{7.10}$$

We now look at the crosscovariance of the correlated LE and HE components. Using a similar analysis as above we get:

$$K_{d_\mathrm{L} d_\mathrm{H}}(\xi) = \langle d_\mathrm{L}(x) d_\mathrm{H}^*(x+\xi) \rangle = m_\mathrm{L}(\xi) * K_g(\xi) * m_\mathrm{H}^*(-\xi) \tag{7.11}$$

$$K_{d_\mathrm{H} d_\mathrm{L}}(\xi) = \langle d_\mathrm{H}(x) d_\mathrm{L}^*(x+\xi) \rangle = m_\mathrm{H}(\xi) * K_g(\xi) * m_\mathrm{L}^*(-\xi), \tag{7.12}$$

where $K_{g_\mathrm{L} g_\mathrm{H}} = K_{g_\mathrm{H} g_\mathrm{L}} = K_g$ since $g_\mathrm{H}(x) = g_\mathrm{L}(x) = g(x)$.

For notational simplicity the 'H' image filters will be lumped with the detector point spread function (PSF) at this point since they affect the optical transfer function (OTF) and MTF of the LE and HE images in the same manner [21, 140], $\mathrm{PSF}_i(x) = \mathrm{PSF}_{\mathrm{D},i}(x) *$

$h_i(x)$. The Fourier transform of the detector PSF yields the detector OTF, $\mathrm{OTF_D}$, and the magnitude of the OTF yields the MTF, $\mathrm{MTF_D} = |\mathrm{OTF_D}|$. The detector signal varies with the gandularity in the object background. Using Eq. (7.9) and the autocovariance and crosscovariance at the output of the detector [22], the autocovariance and crosscovariance after the 'H' image filters are given by:

$$K_{c_i}(\xi) = \left\langle \left. \frac{\partial a_i}{\partial d_i} \right|_{d_i}^2 \right\rangle [\mathrm{PSF}_i(\xi) * K_{d_i}(\xi) * \mathrm{PSF}_i^*(-\xi)] \tag{7.13}$$

$$K_{c_i c_j}(\xi) = \left\langle \left. \frac{\partial a_i}{\partial d_i} \right|_{d_i} \left. \frac{\partial a_j}{\partial a_j} \right|_{d_j} \right\rangle \left[\mathrm{PSF}_i(\xi) * K_{d_i d_j}(\xi) * \mathrm{PSF}_j^*(-\xi)\right], \tag{7.14}$$

where the expectation is taken over the glandularity and j, similar to i, can represent either the LE or HE path.

The combined image is a weighted subtraction of the HE and LE signals. The background autocovariance of the combined image is then given by:

$$K_c(\xi) = w^2 K_{c_\mathrm{L}}(\xi) - w\left(K_{c_\mathrm{L} c_\mathrm{H}}(\xi) + K_{c_\mathrm{H} c_\mathrm{L}}(\xi)\right) + K_{c_\mathrm{H}}(\xi). \tag{7.15}$$

The background NPS of the combined image is given by the Fourier transform of the background autocovariance ($\mathrm{NPS}_c = \mathcal{F}\{K_c(\xi)\}$), which leads to:

$$\begin{aligned}
\mathrm{NPS}_c(u) &= w^2 \mathrm{NPS}_{c_\mathrm{L}}(u) - w\left(\mathrm{NPS}_{c_\mathrm{L} c_\mathrm{H}}(u) + \mathrm{NPS}_{c_\mathrm{H} c_\mathrm{L}}(u)\right) + \mathrm{NPS}_{c_\mathrm{H}}(u) && (7.16)\\
&= \left[\left\langle \left. \frac{\partial a_\mathrm{L}}{\partial d_\mathrm{L}} \right|_{d_\mathrm{L}}^2 \right\rangle \left|w^2 \mathrm{OTF_L}(u)\right|^2 |M_\mathrm{L}(u)|^2 \right.\\
&\quad - \left\langle \left. \frac{\partial a_\mathrm{L}}{\partial d_\mathrm{L}} \right|_{d_\mathrm{L}} \left. \frac{\partial a_\mathrm{H}}{\partial d_\mathrm{H}} \right|_{d_\mathrm{H}} \right\rangle w \mathrm{OTF_L}(u) M_\mathrm{L}(u) \mathrm{OTF}_\mathrm{H}^*(u) M_\mathrm{H}^*(u)\\
&\quad - \left\langle \left. \frac{\partial a_\mathrm{H}}{\partial d_\mathrm{H}} \right|_{d_\mathrm{H}} \left. \frac{\partial a_\mathrm{L}}{\partial d_\mathrm{L}} \right|_{d_\mathrm{L}} \right\rangle w \mathrm{OTF_H}(u) M_\mathrm{H}(u) \mathrm{OTF}_\mathrm{L}^*(u) M_\mathrm{L}^*(u)\\
&\quad \left. + \left\langle \left. \frac{\partial a_\mathrm{H}}{\partial d_\mathrm{H}} \right|_{d_\mathrm{H}}^2 \right\rangle |\mathrm{OTF_H}(u)|^2 |M_\mathrm{H}(u)|^2 \right] \mathrm{NPS}_g(u) && (7.17)\\
&= w^2 \mathrm{NPS}_{\mathrm{B_L}}(u) |H_\mathrm{L}(u)|^2 |M_\mathrm{L}(u)|^2 \mathrm{MTF}_{\mathrm{D,L}}^2(u)\\
&\quad + \mathrm{NPS}_{\mathrm{B_H}}(u) |H_\mathrm{H}(u)|^2 |M_\mathrm{H}(u)|^2 \mathrm{MTF}_{\mathrm{D,H}}^2(u)\\
&\quad - w \mathrm{NPS}_{\mathrm{B_{LH}}}(u) \left[H_\mathrm{L}(u) M_\mathrm{L}(u) \mathrm{MTF}_{\mathrm{D,L}}(u) H_\mathrm{H}^*(u) M_\mathrm{H}^*(u) \mathrm{MTF}_{\mathrm{D,H}}(u)\right.\\
&\quad \left. + H_\mathrm{H}(u) M_\mathrm{H}(u) \mathrm{MTF}_{\mathrm{D,H}}(u) H_\mathrm{L}^*(u) M_\mathrm{L}^*(u) \mathrm{MTF}_{\mathrm{D,L}}(u)\right], && (7.18)
\end{aligned}$$

where OTF_i is the total OTF of image i ($\mathrm{OTF}_i = \mathrm{MTF}_{\mathrm{D},i} H_i$) and $\mathrm{MTF}_{\mathrm{D},i} = \mathrm{OTF}_{\mathrm{D},i} = |\mathrm{OTF}_{\mathrm{D},i}|$ since the detector point spread function is even [140]. Since $K_{c_\mathrm{L} c_\mathrm{H}}(\xi) = K^*_{c_\mathrm{H} c_\mathrm{L}}(-\xi)$, the cross power spectra are conjugate pairs $\mathrm{NPS}_{c_\mathrm{L} c_\mathrm{H}}(u) = \mathrm{NPS}^*_{c_\mathrm{H} c_\mathrm{L}}(u)$ and the result of their sum is real: $\mathrm{NPS}_{c_\mathrm{L} c_\mathrm{H}}(u) + \mathrm{NPS}_{c_\mathrm{H} c_\mathrm{L}}(u) = 2\mathrm{Re}\{\mathrm{NPS}_{c_\mathrm{L} c_\mathrm{H}}(u)\} = 2\mathrm{Re}\{\mathrm{NPS}_{c_\mathrm{H} c_\mathrm{L}}(u)\}$ [141]. The power spectra terms $\mathrm{NPS}_{c_\mathrm{L}}$ and $\mathrm{NPS}_{c_\mathrm{H}}$ are also real [139] therefore we are only interested in the real portion of each power spectra term in Eq. (7.16).

In the case where no filters are applied (i.e., the filters are delta functions) and if $\mathrm{MTF}_{\mathrm{D,L}} \simeq \mathrm{MTF}_{\mathrm{D,H}} = \mathrm{MTF}$, NPS_c in Eq. (7.16) reduces to:

$$\begin{aligned}
\mathrm{NPS}_c(u) &= \left[w^2 \left\langle \left| \frac{\partial a_\mathrm{L}}{\partial g} \right|_g^2 \right\rangle - 2w \left\langle \left| \frac{\partial a_\mathrm{L}}{\partial g} \right|_g \left| \frac{\partial a_\mathrm{H}}{\partial g} \right|_g \right\rangle + \left\langle \left| \frac{\partial a_\mathrm{H}}{\partial g} \right|_g^2 \right\rangle \right] \mathrm{NPS}_g(u) \mathrm{MTF}^2(u) && (7.19) \\
&= \left[w^2 \mathrm{NPS}_{\mathrm{B_L}}(u) + \mathrm{NPS}_{\mathrm{B_H}}(u) - 2w \mathrm{NPS}_{\mathrm{B_{LH}}}(u) \right] \mathrm{MTF}^2(u) && (7.20) \\
&= \mathrm{NPS}_\mathrm{B}(u) \mathrm{MTF}^2(u), && (7.21)
\end{aligned}$$

where NPS_B with no subscript refers to that of the combined image.

From the above derivation it is shown that with the application of the two filters the anatomical noise becomes:

$$\begin{aligned}
\mathrm{NPS}_{\mathrm{B,C}} = \; & w^2 \mathrm{NPS}_{\mathrm{B,L}} |H_\mathrm{L}|^2 |M_\mathrm{L}|^2 \mathrm{MTF}^2_{\mathrm{D,L}} + \mathrm{NPS}_{\mathrm{B,H}} |H_\mathrm{H}|^2 |M_\mathrm{H}|^2 \mathrm{MTF}^2_{\mathrm{D,H}} \\
& - w \mathrm{NPS}_{\mathrm{B,LH}} \mathrm{MTF}_{\mathrm{D,L}} \mathrm{MTF}_{\mathrm{D,H}} \left[H_\mathrm{L} M_\mathrm{L} H^*_\mathrm{H} M^*_\mathrm{H} + H_\mathrm{H} M_\mathrm{H} H^*_\mathrm{L} M^*_\mathrm{L} \right], \qquad (7.22)
\end{aligned}$$

where the frequency dependence has been omitted for clarity. Eq. (7.22) is generalized to include all filters, though when emulating motion all but one filters will be delta functions, that is to say that only one filter will include the effect of motion. For the combined image, the $\mathrm{NPS}_{\mathrm{B,C}}$ noise term contains both correlated ($\mathrm{NPS}_{\mathrm{B,LH}}$) and uncorrelated terms ($\mathrm{NPS}_{\mathrm{B,L}}$ and $\mathrm{NPS}_{\mathrm{B,H}}$). For favorable suppression of the anatomical noise during image combination, the anatomical noise will be reduced by the subtraction of the correlated terms from the uncorrelated terms. When motion is present, the correlated noise will be reduced, making the anatomical noise greater than what it would have been without motion artifacts.

The full combined image noise, i.e. including detector and anatomical noise, is given by:

$$\begin{aligned}
\mathrm{NPS}_\mathrm{C} &= \mathrm{NPS}_{\mathrm{D,C}} + \mathrm{NPS}_{\mathrm{B,C}} = |H_\mathrm{H}|^2 \mathrm{NPS}_{\mathrm{D,H}} + w^2 |H_\mathrm{L}|^2 \mathrm{NPS}_{\mathrm{D,L}} \\
&\quad + w^2 \mathrm{NPS}_{\mathrm{B,L}} |H_\mathrm{L}|^2 |M_\mathrm{L}|^2 \mathrm{MTF}^2_{\mathrm{D,L}} + \mathrm{NPS}_{\mathrm{B,H}} |H_\mathrm{H}|^2 |M_\mathrm{H}|^2 \mathrm{MTF}^2_{\mathrm{D,H}} \\
&\quad - w \mathrm{NPS}_{\mathrm{B,LH}} \mathrm{MTF}_{\mathrm{D,L}} \mathrm{MTF}_{\mathrm{D,H}} \left[H_\mathrm{L} M_\mathrm{L} H^*_\mathrm{H} M^*_\mathrm{H} + H_\mathrm{H} M_\mathrm{H} H^*_\mathrm{L} M^*_\mathrm{L} \right] && (7.23) \\
&= \mathrm{NPS}_\mathrm{H} + w^2 \mathrm{NPS}_\mathrm{L} - w \left(\mathrm{NPS}_{\mathrm{HL}} + \mathrm{NPS}_{\mathrm{LH}} \right), && (7.24)
\end{aligned}$$

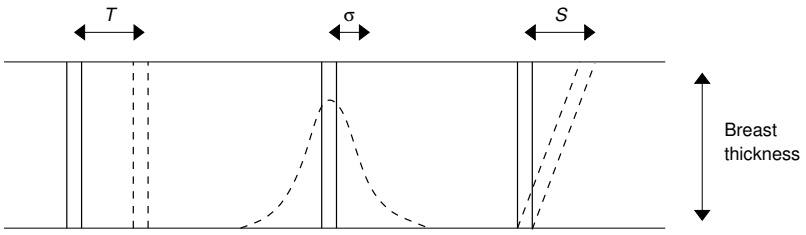

Figure 7.3: Conceptual illustration of the different types of motion considered where a small portion (thin slice) of the object before and after motion is represented by the solid and dashed lines, respectively, for translation (left), distributive (middle), and shear (right) motion.

where again the frequency dependence has been omitted for clarity. From (7.23) we see that the 'M' and 'H' filters have similar effect on anatomical noise. The main difference is that the image filter, 'H', also affects the detector noise while the motion filter 'M' does not. Since we cannot apply a motion filter similar to 'M' to the clinical images, the 'H' filter is used for model verification. The impact of the 'H' filter on the detector noise is taken into account during the model and clinical image comparison.

Motion filters

Typically the motion of the object, e.g. linear or sinusoidal/vibrational, that occurs within the exposure time (i.e. intra-image motion) is of interest [142, 143, 144]. In the current study we are interested in the motion that occurs between exposures (i.e. inter-image motion). In the present study motion is only applied to either the LE or the HE image to emulate the motion that has occurred between the two exposures. Since in the clinical study the HE image was taken after the LE image, the filtration, unless otherwise stated, was applied to the HE glandularity.

Three different types of motion are considered in this study: translation motion, distributive motion, and shear motion (see Fig. 7.3). Each type of motion is implemented using the spatial frequency dependent 'M' filter. The translation and distributive motion filters are also implemented using the 'H' filter for clinical image comparison. The motion filters are linear and shift invariant, and are applied to the entire object. The filters are normalized to unity at zero frequency (unity gain) and thus do not affect the mean signal intensity. Note that the filters considered below are only examples that we consider in this study, and other, more complex types of motion models may be applied.

For translation motion along the x-axis (which refers to the u-axis in the frequency

domain), a shift filter is used whose Fourier transform is given by:

$$M(u,v) = \exp\left(-2\pi jTu\right), \tag{7.25}$$

where $j = \sqrt{-1}$, $\exp(-ju) = \cos u - j\sin u$, and T is the translation distance in real space. It should be noted that the magnitude of the square of the filter yields unity, i.e. $|M|^2 = 1$, thus when this type of noise is applied to the 'H' filter, the detector noise, $\mathrm{NPS_{D,C}}$, will not be affected.

Rotationally symmetric distributive (or diffusive-like) motion of tissue spreading in each direction, is applied using a Gaussian function, whose Fourier transform is given by:

$$M(u,v) = \exp\left(-2\pi^2\sigma^2(u^2+v^2)\right), \tag{7.26}$$

where σ^2 is the variance in real space. Note that this filter is the equivalent of a low-pass filter.

Lastly we consider a type of shear motion, or deformation. As with the translation motion, the shear motion is considered in one dimension (x-axis). For simplicity the glandularity is assumed to be relatively constant, i.e. uniform, within the thickness of the breast. The shear motion filter is much like that of linear intra-image motion [142], and its Fourier transform is given by:

$$M(u,v) = \mathrm{sinc}(\pi uS)\exp\left(-\pi jSu\right), \tag{7.27}$$

where S is the spatial extent of the shear motion in real space.

7.2.4 Cascaded detector model and incident spectra

The conversion material (a-Se) thickness is assumed to be 200 μm, which is the thickness typically used for conventional mammography. The pixel pitch was assumed to be 100μm to match the clinical study. For the comparison study, the spectra were chosen to match those of the Lewin *et al* clinical study (44kVp, rhodium target, and 0.025mm thick rhodium and 8mm thick aluminum filtration for HE exposure and 30kVp, molybdenum target, and 0.03mm thick molybdenum filtration for the LE exposure). The mean glandular dose ratio (ratio of the dose of the HE exposure to the dose of the LE exposure) was determined from the magnitude of the clinical study spectra (Lewin *et al* 2003) for a 50% glandular, 4.5cm thick breast. The dose was chosen to be the same as that estimated from the Lewin *et al* clinical study [133].

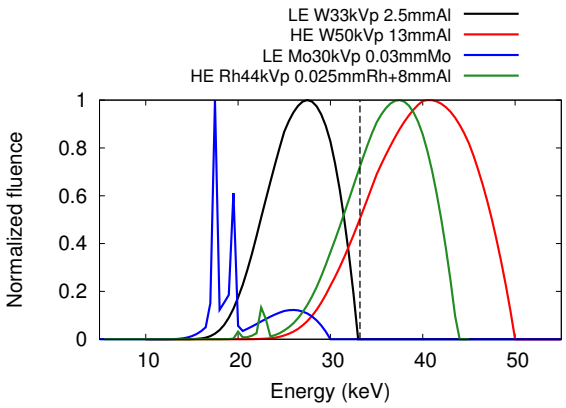

Figure 7.4: LE and HE spectra after passing through the breast. The dashed vertical line represents the K-edge energy of iodine.

For the detectability study, in addition to the Lewin *et al* spectra, the incident spectra to optimize the performance were determined (assuming no motion) for the same dose and breast characteristics as mentioned above. The optimal target/filter combinations were found to be 50kVp with a 13mm aluminum filter for the HE spectrum and 33kVp with a 2.5mm thick aluminum filter for the LE spectrum where a tungsten target was used for both the LE and HE spectra. This was the same optimized spectra as used in the experiments presented in Chapter 6. The optimal weight factor was found to be 0.42 while the optimal dose ratio was found to be 1.7. An iodinated contrast agent was used with an iodine concentration of 3mg/ml, which is feasible for tumor uptake [22]. The spectra used for the clinical comparison study and detectability study are shown in Fig. 7.4. The HE spectra are similar however the LE spectra differ significantly due to the use of the molybdenum target characteristic radiation for the clinical study.

7.2.5 Detectability

The ideal observer detectability index, as presented in Section 5.6 was used to quantify the degradation of the performance due to the presence of motion artifacts. For the detectability study we only consider motion to the object through the 'M' filter. The mean signal that reaches the detector is not altered by filtration and the applied changes to the object glandularity through the 'M' filter will not affect the MTF and $\mathrm{NNPS}_{\mathrm{D,C}}$. However, the task function (W_{Task}) and $\mathrm{NNPS}_{\mathrm{C,B}}$ are affected by the motion. As before the task considered is based on the object-present and object-absent hypotheses, where the object

is the tumor. The task function was computed taking into account the motion applied to the nodule in one of the images.

7.2.6 Clinical images

The noise power spectra of clinical images from a dual-energy CEM study [11] were examined. The images were acquired with a Senographe 2000D mammography unit (GE Medical Systems, Milwaukee, WI) having 100μm pixel pitch. Four sets of mediolateral oblique (MLO) images from the clinical study were investigated where each set contains an LE and an HE image. Noise analysis of the clinical images was carried out using MATLAB (Version R2011a, 170 Mathworks, Natick, MA). Regions of interest (ROI) 256×256 pixels in size containing breast tissue were chosen from the images for analysis. A 2-D second-order polynomial fit was used for detrending [145, 146] and a 50% overlap was used in addition to a cosine-taper [147, 132]. The noise power spectra were obtained by averaging the radially averaged squared modulus of the two-dimensional Fourier transform of the ROIs.

The combined image was obtained using (5.66) where the weight factor was determined as that which minimized the anatomical noise. Attempts were made to correct (by translation) existing motion artifacts found in the clinical images. The amount of correction required was noted. As previously mentioned, since we do not have direct access to the anatomical information, but instead have the signals acquired after passing through the detection system, the comparison of the theoretical model and the clinical images is carried out using the 'H' filter as opposed to the 'M' filter.

7.3 Results

The clinical images are first compared with the cascaded systems model using the distributive (Gaussian) and translation filters. Then the detectability of tumors of different size in the presence of different amount of motion artifacts is investigated using the extended cascaded systems model.

7.3.1 Clinical image comparison

First how noise is affected by filters in the clinical images is looked at. The clinical images were combined using a weight factor that led to the least amount of anatomical noise in

Table 7.1: Pixel translations (motion correction) and weight factors for anatomical noise reduction in the clinical images (100μm pitch pixels).

Image 1		Image 2		Image 3		Image 4	
x (pix.)	y (pix.)	x (pix.)	y (pix.)	x (pix.)	y (pix.)	x (pix.)	y (pix.)
1	0	4	2	3	5	6	3
w		w		w		w	
0.19		0.23		0.25		0.19	

the combined image. The anatomical noise was further reduced in the combined image by applying translations to one of the images (LE or HE). This translation was used to obtain the 'motion corrected' combined image, although the only motion that was attempted to be corrected was translation motion. The weight factors and translations for the (four) different image sets are summarized in Table 7.1. These translations correspond well with those found in previous CEM studies [10, 69, 132]. The NNPS as a function of spatial frequency for the four image sets, including the noise for the LE and HE images alone, is shown in Fig. 7.5. It should be noted that for all the NNPS of the LE images that are shown in the results section (for the model and clinical images), the effect of the applied weight factor is taken into account, i.e. $\mathrm{NNPS}_{\mathrm{L}}^{\mathrm{results}} = w^2\mathrm{NNPS}_{\mathrm{L}}$. This is done for a more effective comparison since in the combined image the effect of the weight factor has been included.

The 'motion corrected' images were used as the baseline images prior to applying any filter for comparison. Figure 7.6 shows the noise of the combined image for different amounts of translation. A single pixel translation does not significantly increase the noise. However for larger translations the noise becomes greater than the LE and HE image noise at high frequencies. The slope of the anatomical noise also changes and the frequency where the anatomical noise approaches the detector noise is increased. From Fig. 7.6 it is also clear that translations in either direction led to approximately the same amount of noise, which is expected for a translation motion corrected image. The suppression of the anatomical noise at 1mm^{-1} when $T = 1000\mu$m, due to the effect of the cosine (from the real part of Eq. (7.25)), is visible in all cases.

The Gaussian filter was applied to either the LE or HE images, and the results for the combined image are shown in Fig. 7.7. From Fig. 7.7 it can be seen that the noise is relatively unaffected by significant filtration ($\sigma_{\mathrm{L}} = 500\mu$m) at low frequencies (<0.7mm^{-1}). At high frequencies the noise tends to either the LE or HE image noise, the opposite of which the filter was applied to and has had its high frequency components lessened. The combined image noise becomes significant at low frequencies when the filtration is increased to $\sigma = 1000\mu$m.

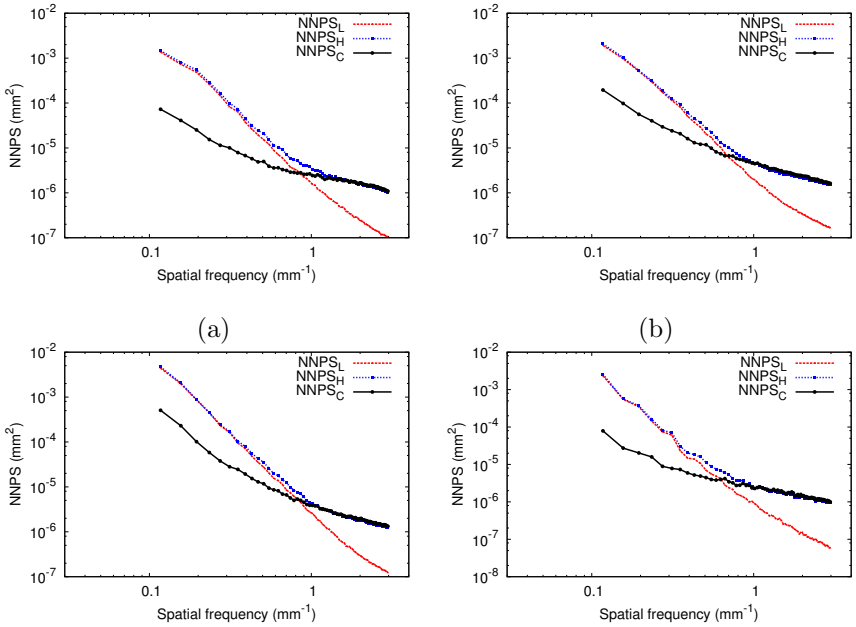

Figure 7.5: NNPS for the combined, LE, and HE clinical images using the parameters in Table 7.1.

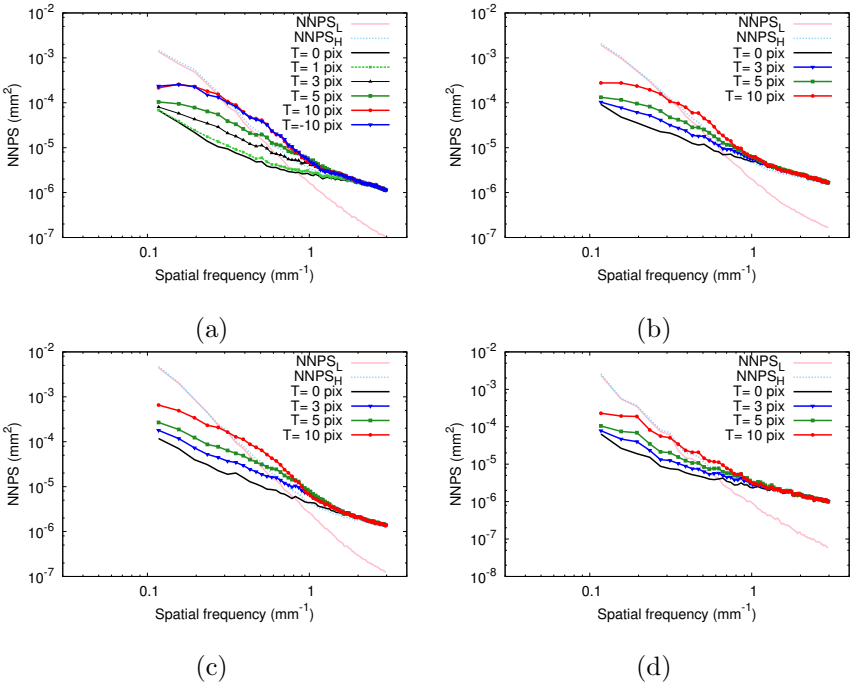

Figure 7.6: NNPS for clinical images with different magnitudes of translation, T, where 1 pixel is equivalent to 100μm. The negative sign indicates a shift in a direction opposite to all other shifts.

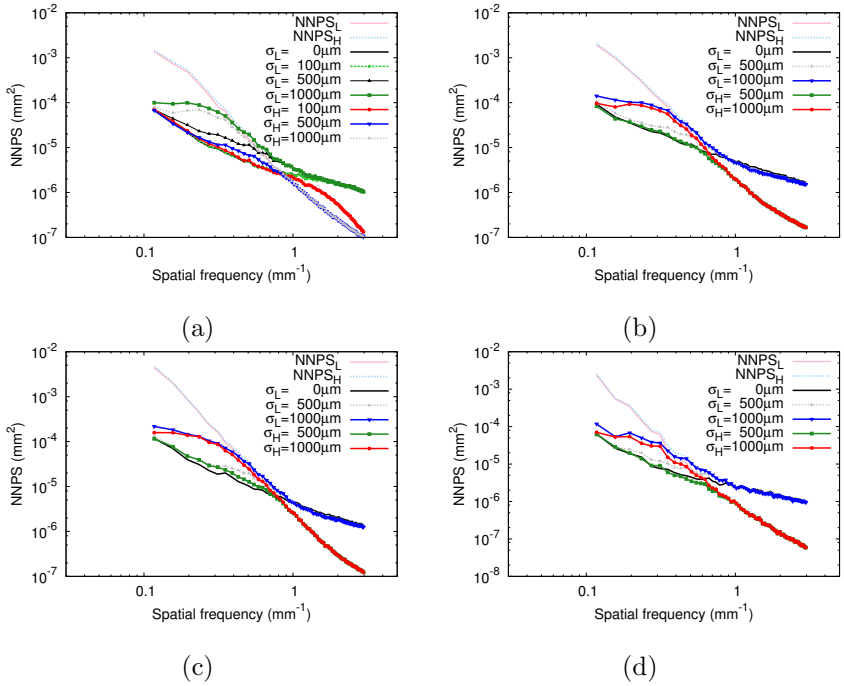

Figure 7.7: NNPS for clinical images with different magnitudes of Gaussian filtration. The subscript for σ indicates whether filter was applied to the low- (L) or high-energy (H) image.

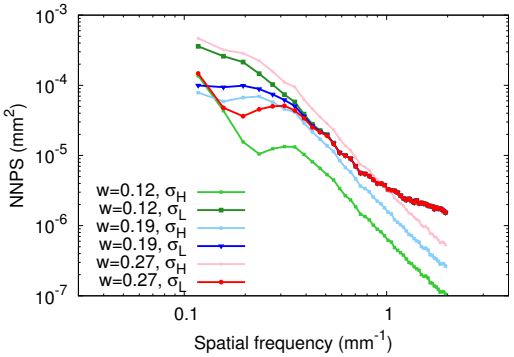

Figure 7.8: NNPS for clinical image (image set 1) for Gaussian filtration ($\sigma = 1000\mu$m applied to either LE or HE image) with different weight factors.

When using the Gaussian filter, a local minimum can be seen at the frequency where the anatomical noise is significantly suppressed. The frequency of this local minimum depends on the weight factor and which image (LE or HE) the filter was applied to, as seen in Fig. 7.8. The anatomical noise approaches the noise of the unfiltered image for frequencies higher than the local minimum.

The correlated noise term in Eq. (7.24), which is present due to correlation of the background in the LE and HE images, was investigated by fitting the NNPS of the LE and HE images to $\text{NNPS}_i = K_i/f^\beta$ (see Eq. (5.72)). It was assumed that the MTF is flat in the spatial frequency region of interest (i.e., MTF = 1) and we are only interested in the real component of the NNPS. A Gaussian filter was applied to either the LE or the HE image and the NNPS of the combined clinical image was calculated. Consistent with the model equations, the correlated noise term was modeled as $\sqrt{K_\text{L}K_\text{H}}H/f^\beta$, where H is the transfer function of the Gaussian filter. The fit model matched quite well with the clinical image and the results are shown in Fig. 7.9.

The NNPS of the anatomical and detector noise for no filter, translation filter, and Gaussian filter using the cascaded model are now presented. Differences in the simulated and clinical images can be expected due to differences in breast size, glandularity, and detector. For example, here a 200μm thick a-Se detector was assumed, which has different photon absorption and spatial frequency response characteristics compared to the cesium iodide (CsI) panel used in the clinical study. For comparison with the clinical images a weight factor of 0.2 is used, unless otherwise stated, the same as that used in the clinical study (Lewin *et al* 2003). The detector noise (NNPS_D) is plotted (Fig. 7.10(a)) alongside the anatomical noise (NNPS_B) for the LE, HE, and CEM images using the cascaded systems

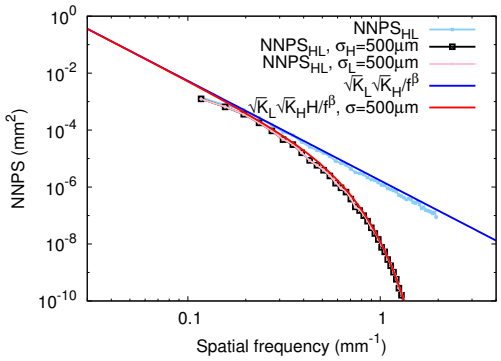

Figure 7.9: Correlated NNPS for the clinical image (image set 1), fitted model, and applied Gaussian filter.

model. The total (summed) noise is shown in Fig. 7.10(b).

The NNPS for different magnitudes of translation are shown in Fig. 7.11. Note that the magnitudes of the simulated translations are in multiples of the pixel pitch, 100μm [148]. Also, the direction of the shift (e.g. in the positive or negative x direction) and the image that is translated (LE or HE) are not important since the resulting NNPS will be equivalent. The trends seen in Fig. 7.11 are similar to those for the clinical images: combined image noise greater than the LE and HE images, change in slope, higher frequency where anatomical is similar magnitude of detector noise. The suppression of the anatomical noise at 1mm^{-1} for $T = 1000\mu$m is also clearly visible, similar to the clinical images.

The NNPS for different magnitudes of Gaussian filtration are shown in Fig. 7.12. From Fig. 7.12 it can be seen that for some magnitude of filtration there is a frequency where the anatomical noise is cancelled. As with the clinical image, the presence of the local minimum (due to cancellation) and the frequency at which it occurs is seen to vary with weight factor, w, and which image the filter is applied to (see Fig. 7.12(b)). It can be seen that the features from the model match well with those of the clinical images.

7.3.2 Impact of motion artifacts on detectability

For the detectability study two different spectra were considered: the optimal spectra that was found using the cascaded systems model and the spectra used in the Lewin *et al* study. To look at how motion artifacts reduce detectability tumors of different sizes, i.e. radii, were considered: 2mm, 2.5mm, and 5mm. The weight factor was varied to achieve

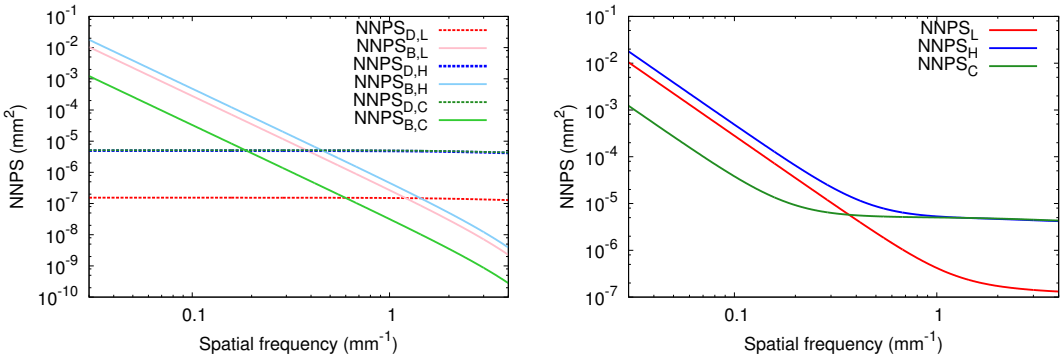

(a) (b)

Figure 7.10: (a) Different components of NNPS (along the u-axis) for the cascaded systems model. (b) Similar to (a) except the contributions have been added.

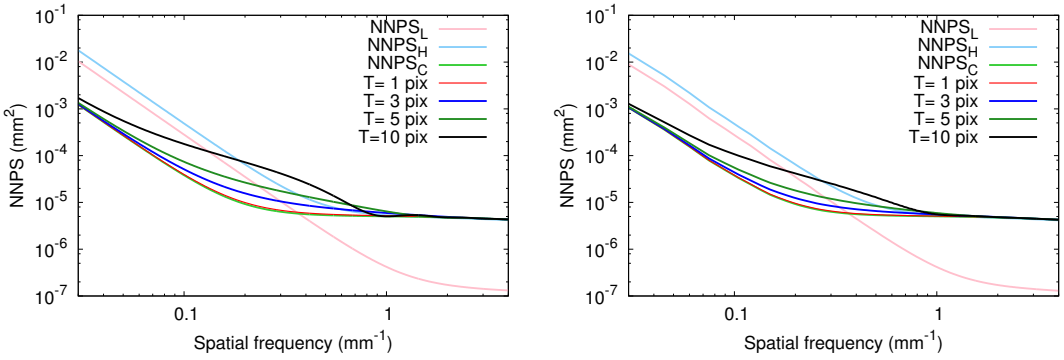

(a) (b)

Figure 7.11: (a) NNPS (total) along the u-axis for different magnitudes of translation. (b) Similar to (a) except the radially averaged NNPS (similar to the clinical images).

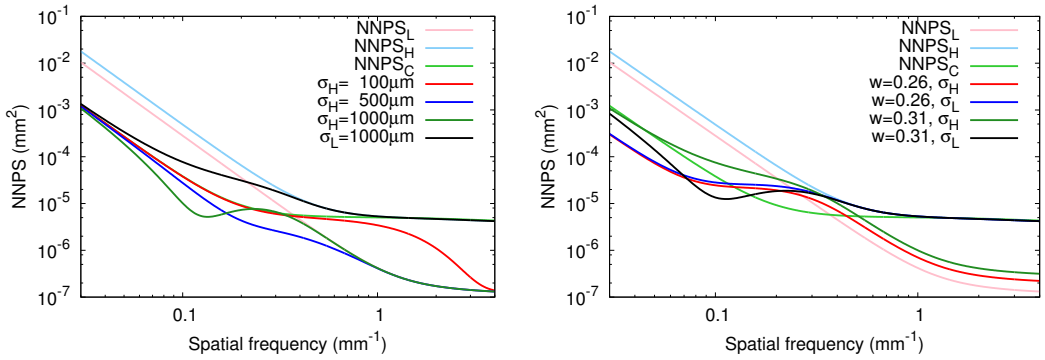

(a) (b)

Figure 7.12: (a) NNPS (total) along the u-axis for different magnitudes of Gaussian filtration. (b) NNPS for Gaussian filtration ($\sigma = 1000\mu$m applied to either LE or HE image) for different w.

the greatest performance as the amount of motion was modified. The detectability for the different cases considered was normalized, for each tumor size, to the detectability obtained without motion. The results for the two different spectra are summarized in Tables 7.2 and 7.3.

The degradation, to different extents, of the detectability for the three types of motion are seen. For significant motion the detectability is reduced to half or lower in some cases. The distributive motion applied to the HE image (as opposed to the LE image) was seen to have a greater degradation on tumor detectability, though a dissimilar effect on the anatomical noise after applying such a filter to the LE or HE glandularity could be expected given the results in the previous section. There were not many drastic differences across the tumor sizes though the larger tumor detectability did not degrade as much for the distributive motion. However the larger tumor detectability was degraded the most for the translation motion.

The degree to which the detectability is degraded was found to be dependent on the incident spectra. Aside from the differences in spectral shape, the spectra also had different dose ratios and thus the levels of quantum noise in the LE and HE images were not the same in both cases. In addition, the optimal spectra were found to better eliminate the anatomical noise, which led to a better baseline (i.e. motion-absent) detectability (approximately 2.1 times the performance for all three tumor sizes). Better suppression of the anatomical noise resulted in the detectability having a higher sensitivity to motion artifacts.

Table 7.2: Normalized detectability using optimal spectra for different amount of motion and tumor sizes. [a]Motion applied to LE image.

Tumor radius (mm)	Normalized detectability											
	Translation, T (μm)				Distributive, σ (μm)				Shear, S (μm)			
	100	300	500	1000	100	500	1000	1000[a]	100	300	500	1000
2	0.92	0.72	0.62	0.51	0.98	0.71	0.42	0.67	0.97	0.85	0.74	0.60
2.5	0.90	0.68	0.57	0.46	0.99	0.78	0.47	0.66	0.97	0.83	0.72	0.56
5	0.90	0.66	0.54	0.40	1.00	0.93	0.70	0.77	0.97	0.82	0.70	0.59

Table 7.3: Normalized detectability using Lewin *et al* study spectra for different amount of motion and tumor sizes. [a]Motion applied to LE image.

Tumor radius (mm)	Normalized detectability											
	Translation, T (μm)				Distributive, σ (μm)				Shear, S (μm)			
	100	300	500	1000	100	500	1000	1000[a]	100	300	500	1000
2	0.99	0.94	0.90	0.84	0.99	0.77	0.51	0.98	0.99	0.93	0.85	0.67
2.5	0.98	0.90	0.83	0.74	0.99	0.82	0.55	0.94	0.99	0.93	0.84	0.65
5	0.98	0.86	0.76	0.61	1.00	0.95	0.81	0.93	0.99	0.94	0.86	0.69

7.4 Discussion

The inclusion of motion in the performance analysis allows a fairer comparison between dual-exposure techniques, such as that investigated in this work, and single-exposure techniques, such as spectral separation using a thresholding photon counter [22], differential beam filtering [17], and multilayer detectors (such as that proposed in this thesis). Although the motion was applied to dual-energy images, the method presented could easily be applied to temporal subtraction CEM [10], where one image is taken prior to the injection of the contrast agent and the other image is taken after the injection. The degradation of the detectability due to the addition of motion was shown to reduce the detectability by a factor of two in some cases, which is quite significant. The incident spectra also had a considerable effect on the detectability (factor of two difference for the two different spectra considered in this study). It was shown in Section 5.9.2 that a factor of two difference in detectability (using optimized spectra) between the dual-exposure dual-energy technique and the single-exposure multilayer technique is not atypical. This suggests that accounting for the effect of motion is essential in the performance comparison of dual-exposure and single-exposure techniques.

The three filters that were considered in the model are examples of different types of motion and other types of filters emulating motion could be applied. Although shift invariant filters were considered, it is noted that the different types of motion that exist

may be more localized. For example, Carton *et al* [69] found in their contrast-enhanced digital breast tomosynthesis study that generally the greatest motion occurred in the lower portion of the breast. It is also noted that various motion correction and image registration techniques exist [149]. Such techniques have not been included in the present study though they could be used to reduce the effect of motion artifacts on image noise.

In summary, motion artifacts caused by motion between LE and HE exposures for dual-energy CEM were studied to gain a better understanding of their impact on anatomical noise and performance (i.e., tumor detection). A method to include the effect of motion using an extended cascaded systems model was presented. CEM images from a clinical study were analyzed for comparison of the model and generally good agreement was found between the model and the clinical images. The degradation of the ideal observer detectability due to the effect of three different types of motion (translation, distributive, and shear) was investigated using optimized spectra and spectra from a previous clinical study. The detectability of larger tumors was more significantly affected by translation motion and least affected by distributive motion compared to smaller tumors. Shear motion had approximately the same degradation of detectability for all tumor sizes examined. The spectra that better suppressed the anatomical noise was found to have a detectability more sensitive to the addition of motion. The results indicated that motion can have a significant effect on tumor detectability. The method presented in this chapter can be used as a tool for providing a more comprehensive performance comparison between acquisition techniques or technologies for applications involving the combination of multiple images where inter-image motion may be of concern, such as CEM.

Chapter 8

Noise reduction techniques

8.1 Introduction

It was found from the simulations in Chapter 5 that the noise in the HE image of the multilayer detector was much greater than that of the LE image, making the detector noise of the DE image limited by the HE image. Since the multilayer detector does not allow independent control of the HE and LE exposures, this is a challenging issue to address. Previously, noise reduction techniques were applied to similar DE imaging situations [150]. For this reason, noise reduction techniques were investigated to determine whether the performance of the multilayer detector could be improved.

Although the use of DE imaging leads to images with suppressed anatomical noise, the noise of the DE image is increased [151]. Noise reduction of the DE image by image processing through combination algorithms is appealing, compared to increasing the exposure to reduce noise, since there is no increase in patient dose. Several image combination noise reduction strategies have been investigated to mitigate the increase of DE image noise [152], e.g., smoothing one of the images (HE image) [136] and correlated-noise reduction of complementary DE images [153].

Noise reduction techniques have previously been modeled to estimate their effectiveness [154] and how well they compare with other techniques [21]. Though phantom studies [151] or clinical image studies [154] have been used to estimate the performance of noise reduction techniques in the presence of an anatomical background, the anatomical noise has been neglected in theoretical models. Neglecting the anatomical noise may lead to over-estimation of noise reduction effectiveness and inaccurate optimal image combination parameters.

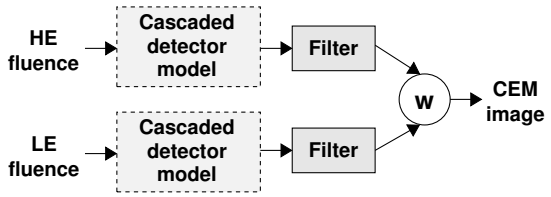

Figure 8.1: Schematic of CEM image flow.

In this work a method of including the anatomical noise in the evaluation of linear noise reduction techniques is presented. Specifically, dual-energy CEM is targeted. The image filtering of the noise reduction techniques are included in a cascaded systems model, which can then be used for noise analysis or performance analysis through detectability studies. The cascaded systems model accounts for anatomical, quantum, and electronic noise. For model verification, the model is compared with the DE image from a previous CEM clinical study [11]. The model presented may be used for a more accurate and comprehensive theoretical optimization and comparison of noise reduction techniques.

8.2 Materials and methods

8.2.1 DE image signal and noise

Figure 8.1 shows the image flow when using noise reduction techniques. The image filters are essentially the same as the 'H' filters presented in Chapter 7. As before the DE image is given by the combination of the LE and HE images [21, 22]:

$$I_{\mathrm{DE}} = I'_{\mathrm{H}} * h_{\mathrm{H}} + I'_{\mathrm{L}} * h_{\mathrm{L}} \tag{8.1}$$

where h_i is the filter for image i, $*$ denotes the convolution operator, and the prime denotes that these are altered zero mean images $(I/\langle I\rangle - 1)$ where the angle brackets denote the average of the signal over space. It should be noted that one difference of this notation from the previous chapter is that the weight factor, w, is taken as part of the noise reduction filter, h_{L}. In the case of standard weighted subtraction, Eq. (8.1) becomes $I'_{\mathrm{H}} - wI'_{\mathrm{L}}$.

The noise in the DE image, similar to the noise in the LE and HE images, is a combination of the anatomical noise, $\mathrm{NPS_B}$, and detector (quantum plus electronic) noise, $\mathrm{NPS_D}$. In the presence of image filters the detector and anatomical noise is modified. The effect of the image filters on the uncorrelated detector noise has previously been found to be [21]:

$$\mathrm{NPS}_{\mathrm{D,DE}} = \mathrm{NPS}_{\mathrm{D,L}}|H_{\mathrm{L}}|^2 + \mathrm{NPS}_{\mathrm{D,H}}|H_{\mathrm{H}}|^2 \tag{8.2}$$

where H_i is the Fourier transform of the filter h_i. Previously the anatomical noise component was ignored for noise reduction technique analysis, making the analysis incomplete. The effect of noise reduction filters on the anatomical noise of a DE image was derived in Section 7.2 and was found to be:

$$\begin{aligned} \mathrm{NPS}_{\mathrm{B,DE}} &= \mathrm{NPS}_{\mathrm{B,L}} \left|H_{\mathrm{L}}\right|^2 \mathrm{MTF}_{\mathrm{D,L}}^2 + \mathrm{NPS}_{\mathrm{B,H}} \left|H_{\mathrm{H}}\right|^2 \mathrm{MTF}_{\mathrm{D,H}}^2 \\ &\quad +2\mathrm{NPS}_{\mathrm{B,LH}}\mathrm{MTF}_{\mathrm{D,L}}\mathrm{MTF}_{\mathrm{D,H}}H_{\mathrm{L}}H_{\mathrm{H}} \end{aligned} \tag{8.3}$$

The MTF of the DE image is given by the normalized weighted sum of the LE and HE optical transfer functions (OTF), where $\mathrm{OTF}_i = \mathrm{MTF}_{D,i}H_i$ [21]:

$$\mathrm{MTF}_{DE}(u,v) = \left| \frac{k_{\mathrm{L}}\mathrm{MTF}_{\mathrm{L}}(u,v)H_{\mathrm{L}}(u,v) + k_{\mathrm{H}}\mathrm{MTF}_{H}(u,v)H_{\mathrm{H}}(u,v)}{k_{\mathrm{L}}H_{\mathrm{L}}(0,0) + k_{\mathrm{H}}H_{\mathrm{H}}(0,0)} \right|, \tag{8.4}$$

$$\tag{8.5}$$

where the weights k_{L} and k_{H} are the same as those presented in Section 5.6. The resulting DE image MTF is normalized such that at zero spatial frequency it has a magnitude of unity.

8.2.2 Noise reduction techniques

Linear noise reduction techniques may be applied by filtering the LE and HE images during image combination through the h_{L} and h_{H} filters, respectively. A generalized form of noise reduction techniques can be written as [21]:

$$\begin{aligned} I_{\mathrm{DE}} &= I'_{\mathrm{L}} * [w_{\mathrm{L}}h_{\mathrm{L,HPF}} - wh_{\mathrm{L,LPF}}] + \\ &\quad I'_{\mathrm{H}} * [h_{\mathrm{H,LPF}} - w_{\mathrm{H}}h_{\mathrm{H,HPF}}] \end{aligned} \tag{8.6}$$

where the LPF and HPF subscripts refer to low pass filters and high pass filters, respectively. The generalized equation can be shown to reduce to standard weighted subtraction (SWS):

$$I_{\mathrm{DE}} = I'_{\mathrm{H}} - wI'_{\mathrm{L}}, \tag{8.7}$$

simple smoothing of the HE image (SSH):

$$I_{\mathrm{DE}} = I'_{\mathrm{H}} * h_{\mathrm{LPF}} - wI'_{\mathrm{L}}, \tag{8.8}$$

and anti-correlated noise reduction (ACNR):

$$I_{\mathrm{DE}} = I'_{\mathrm{H}} * (\delta - w_n h_{\mathrm{HPF}}) - wI'_{\mathrm{L}} * (w_n w_c h_{\mathrm{HPF}} - w\delta) \tag{8.9}$$

where the various w variables are weight factors and δ is the delta function.

8.2.3 Single-layer clinical image comparison and multilayer study

Noise reduction techniques are applied to theoretical noise and performance analysis using the described model. The noise from the model of a single-layer detector is then compared with the noise of a clinical image from a previous [11] DE CEM study. The noise reduction techniques are then applied to a multilayer detector to determine whether any benefits in performance can be achieved.

To evaluate the performance, the ideal-observer detectability index is used, as discussed in Chapter 5. The task considered is finding a tumor (object-present/object-absent type), which is modeled using the designer nodule function [98]. The detector model is assumed to be made of a-Se, the details of which are described in the previous chapters. The spectra for the single-layer detector and dose were modeled to be the same as those in the comparison clinical study. The K anatomical noise constant from Eq. (5.72) was determined from the intersection of the anatomical noise and detector noise in the clinical images (prior to image combination). As in the previous chapter, a skewed glandularity distribution was assumed. The high pass and low pass filters were applied using Gaussian filters,

$$H_{\text{LPF}}(u,v) = \exp\left(-2\pi^2\sigma^2(u^2+v^2)\right), \tag{8.10}$$

and

$$H_{\text{HPF}}(u,v) = 1 - \exp\left(-2\pi^2\sigma^2(u^2+v^2)\right). \tag{8.11}$$

The noise power spectra of a set of clinical images (LE and HE) from a DE CEM study (the same study as that described in the previous chapter) were examined for model comparison. The images were corrected for translational motion and the noise power spectra were determined using the method described in Section 7.2.6.

For the multilayer study, the optimal Mo/Mo anode/filter combination was used with 50μm/1000μm thick top/bottom layers (see Section 5.10). The anatomical noise constant, K, found in the previous chapter was used. Since it is a study of noise reduction, a lower dose than used in simulations of the previous chapters was used. For the multilayer study the dose was halved (to 0.71mGy).

8.3 Results

8.3.1 Single-layer detector noise reduction analysis

The enhancement of CEM signal and noise properties using noise reduction techniques is first examined without considering the anatomical noise. An ACNR technique is used [154],

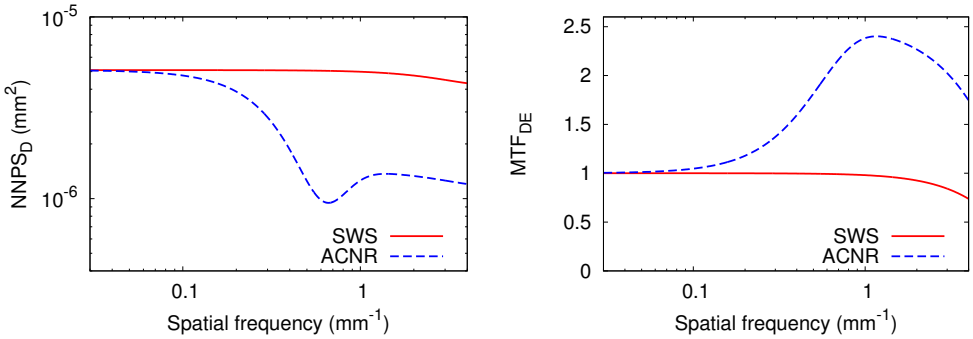

(a) (b)

Figure 8.2: (a) NNPS, not considering anatomical noise, and (b) MTF.

considering $\sigma = 400\mu$m, 3mg/ml iodine contrast agent concentration, and a 2mm radius tumor. Favorable performance (based on d') led to $w_c = 0.8$ and $w_n = 1$ ACNR parameters. The SWS weight factor was chosen to match the one that reduced anatomical noise the most in the clinical image, $w = 0.19$. The detectability index was improved from 19.7 to 27.6 (a 40 percent increase) when using ACNR. Improvements in both the NPS and MTF were observed when using ACNR, as shown in Fig. 8.2.

When the anatomical noise is taken into account, it was found that the noise reduction technique is no longer helpful since it led to an increase in anatomical noise compared to SWS (see Fig. 8.3(a)). The detectability index was found to decrease from 7.0 to 4.9 (30 percent decrease). The noise reduction parameters were refined taking into account the anatomical noise and it was found that $w_c = 0.1$ and $w_n = 1$ led to favorable detectability, however only a marginal improvement was found. The detectability index increased from 7.0 to 7.4, an increase of 6 percent. The NPS using the refined ACNR parameters are shown in Fig. 8.3(b). There is a drastic difference between the NPS using the different noise reduction parameters. With the refined parameters it was found that both the detector noise and anatomical noise may be reduced from their SWS counterpart, though the anatomical noise to a lesser extent. The results demonstrate the impact and importance of the inclusion of anatomical noise in noise reduction analysis.

Clinical images were filtered using the same ACNR filters as those used for the model. The resulting NNPS for the DE CEM image is shown in Fig. 8.4. The results match well with those from the model, indicating that the anatomical noise is increased when using ACNR with $w_c = 0.8$ and the total noise is decreased compared to that of SWS when using ACNR with $w_c = 0.1$.

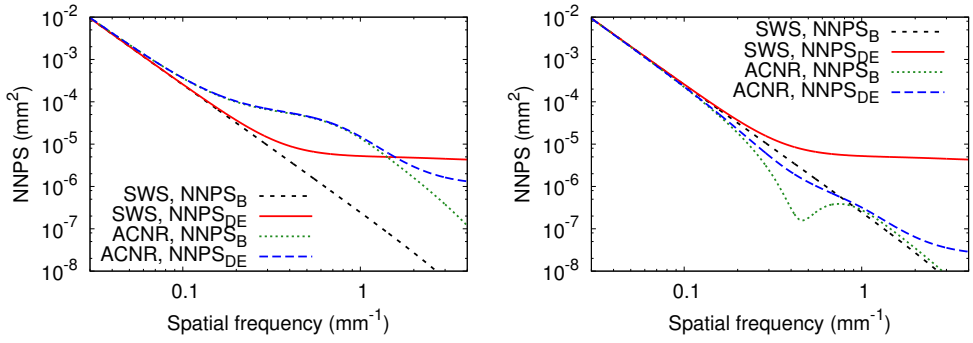

(a) (b)

Figure 8.3: NNPS, when considering anatomical noise, for (a) $w_c = 0.8$ and (b) $w_c = 0.1$.

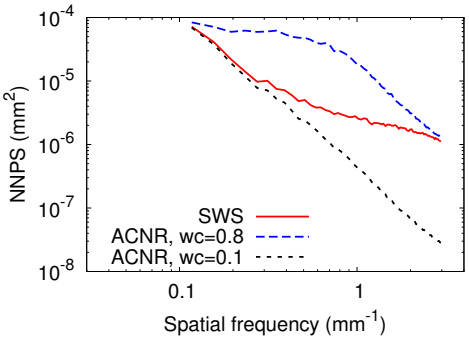

Figure 8.4: NNPS of DE clinical image using different noise reduction parameters.

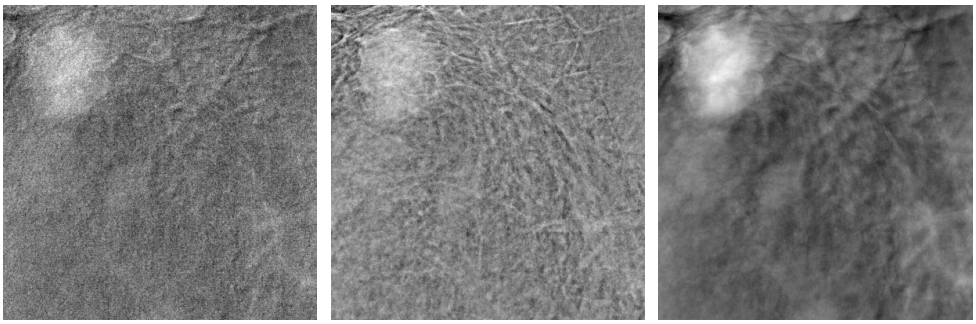

(a) (b) (c)

Figure 8.5: Clinical image when applying SWS, ACNR ($w_c = 0.8$), and ACNR ($w_c = 0.1$) noise reduction techniques.

The noise reduction technique was applied to a DE CEM clinical image with a tumor for qualitative verification of the technique. A portion of the image is shown in Fig. 8.5. Similar to what was observed from the NPS plots, the anatomical noise has a significant presence and is increased compared to the SWS image when using $w_c = 0.8$. Both the detector and anatomical noise are reduced when $w_c = 0.1$. The qualitative characteristics are observed to agree well with the model findings. The detectability will however depend on the task of interest.

8.3.2 Multilayer detector noise reduction analysis

Previously it was found the noise of HE image is much greater than that of the LE image. Since the LE and HE beams are not controlled independently, it is difficult to reduce the noise of the HE image. Here we examine the use of low-pass filter for reducing the noise in the HE image (referred to as SSH in Section 8.2), similar to what was done in previous DE studies [136].

The SSH method ($\sigma = 400\mu$m) was applied to the multilayer CEM image to determine its potential for noise reduction. Though it was found to reduce the detector noise (Fig. 8.6(a)), there was a significant drop in MTF for a 2.5 mm tumor (Fig. 8.6(b)). Such a drop in MTF had previously been observed in DE imaging [21], where its presence depends on the material being imaged and the image combination weighting. The task function of the 2.5 mm tumor is shown in Fig. 8.7 where it can be seen that the frequencies of interest lie in the same spatial frequencies as the drop in MTF, making the SSH technique unfavorable.

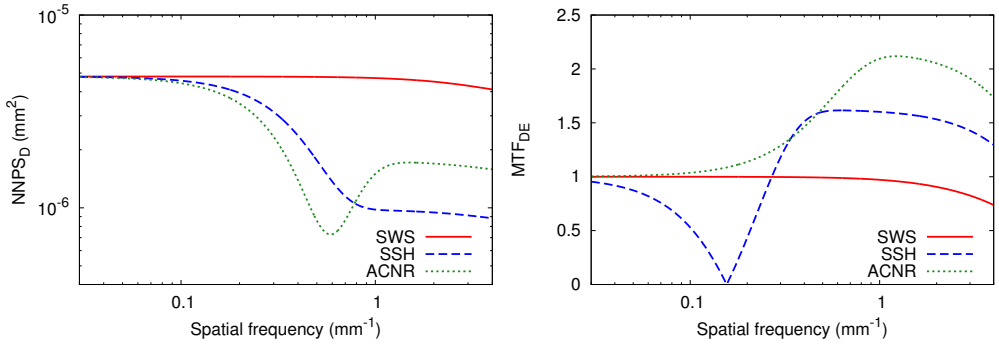

(a) (b)

Figure 8.6: DE (a) MTF and (b) $\mathrm{NNPS_D}$ for SSH and ACNR noise reduction techniques ($\sigma = 400\mu$m).

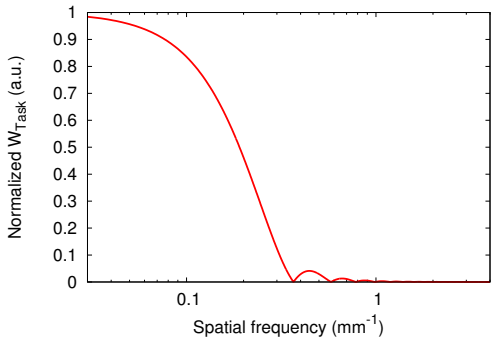

Figure 8.7: Normalized task function for object absent/object present hypotheses of a 2.5mm tumor.

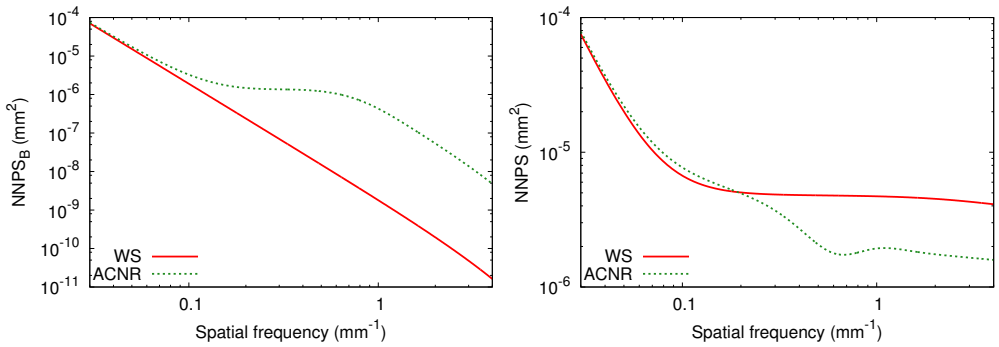

(a) (b)

Figure 8.8: (a) $\mathrm{NNPS_B}$ and (b) total NNPS using noise reduction techniques ($\sigma = 400\mu$m).

Similar reductions in detector noise were found to be achievable using the ACNR method (Fig. 8.6(a)) with $w_c = 0.8$ and $w_n = 1.0$. A benefit of using the ACNR method is that no decrease in MTF was found; on the contrary, the MTF was actually improved. Such an increase in the DE MTF was previously reported for DE chest imaging [21]. From Section 8.3.1 it was found that the anatomical noise plays a big role in how effective the noise reduction technique will be. The effect of the ACNR method on anatomical noise is shown in Fig. 8.8(a), while the total CEM image noise, including anatomical and detector noise, is shown in Fig. 8.8(b). The detectability of the 2.5 mm tumor using the SWS, SSH, and ACNR methods was found to be 15.8, 13.6, and 17.5, respectively. Notice that using the SSH method actually led to a lower detectability.

8.4 Discussion

Previous theoretical noise reduction technique studies ignored the anatomical noise. A method was presented in this chapter to include the anatomical noise in the analysis using a cascaded systems approach. From the results presented, it was found that the inclusion of the anatomical noise in the analysis is imperative for a comprehensive evaluation of noise reduction techniques and technique comparison. To validate the proposed model, the model results were compared with clinical image data and good agreement was found. Depending on the task, the noise reduction technique could be tuned and evaluated without the need of, or prior to, more complex phantom studies.

The SSH and ACNR methods were applied to the multilayer CEM image. Though the SSH method was found to impair the image quality (through the MTF), the ACNR method was found to be beneficial, and a somewhat marginal improvement was found ($\sim$ 11 percent increase in detectability) over the standard weighted subtraction method. Such an increase was also found for the single-layer detector (6 percent increase using the ACNR method), therefore it is not expected that either detector will benefit much greater than the other using noise reduction techniques. Though only the SSH and ACNR methods were applied here, it is possible the generalized form (Eq. 8.6) could be used to further optimize the noise reduction.

Chapter 9

Summary, conclusions and future considerations

9.1 Summary

A major difficulty in breast cancer detection is the spatial variation of breast tissue (both adipose and glandular) that causes anatomical noise to appear in the image. CEM can alleviate this difficulty by subtraction of the anatomical noise in the combination of two subtracted images. Since CEM requires multiple images, if the images are taken at different points in time, motion artifacts may appear in the combined image. Such artifacts could be avoided with the use of a single-exposure CEM technology.

This thesis proposed a multilayer detector with energy discriminating capabilities for medical imaging applications. The multilayer detector was designed for single-exposure CEM using an iodinated contrast agent. Unlike previous multilayer studies, none of which focused on targeting CEM, this study used a large area active matrix flat panel detector. Amorphous selenium was chosen as the x-ray conversion material due to its appealing properties for imaging in the CEM x-ray energy range. The main benefit of the detector is that it is a single-exposure technology, meaning there are no motion artifacts in the combined image. Besides this advantage there are several others that warrant mentions. The multilayer design described in the thesis leverages existing flat panel a-Se technology (the same as that used for mammography), meaning it could be easily implemented without many modifications. A CEM system equipped with a multilayer detector would not require kVp switching, multiple anodes (for providing different spectra characteristics if necessary), or filter switching, as would be required for a dual-exposure dual-energy method using a

single-layer detector. The cost of the detector component of such a system would however increase due to the use of two stacked flat panel detectors.

Other proposed single-exposure CEM methods use a slot scanning detector and either acquire the images by differential filtering or spectral separation using thresholding. The advantage of slot scanning detectors is that they are quantum noise limited and have increased scatter rejection, however there is increased loading on the x-ray tube (meaning more frequent tube replacement) and a longer scan time. The longer scan time in itself can lead to motion artifacts in the image (from one side of the object to the other in the scanning direction). In addition, an ideal electronic threshold level for spectrum separation is difficult to achieve.

Dual-exposure CEM techniques, both temporal and dual-energy subtraction, have the benefit that the existing mammography infrastructure (conventional single-layer mammography detector) may be used with slight modifications to the mammography unit (if possible). The extended time between images makes temporal subtraction prone to significant motion artifacts. Dual-energy subtraction is also prone to motion artifacts, though to a lesser degree than temporal subtraction. Aside from artifacts due to motion, image lag can also lead to artifacts in the combined image if the two images are taken in a short succession time period. As mentioned above, dual-energy subtraction also requires some or all of the following: x-ray tube kVp switching, two different x-ray tubes or multiple anodes, and filter switching.

Four main components were discussed in the thesis: a theoretical system optimization study, an experimental study, a motion artifact study, and a noise reduction study. From the theoretical system optimization study the a-Se multilayer and single-layer detectors were optimized for single-exposure and dual-exposure CEM, respectively. It was found that a midfilter did not significantly improve the performance of the multilayer detector. For the multilayer detector a tube voltage of approximately 50kV was found to be optimal and spectrum splitting could be achieved by filtration (e.g. Rh, Ag filters) for W anodes, or by the inherent characteristic x-rays (e.g. Mo, Rh anodes). A top layer thickness of 50-100μm and a bottom layer thickness of 600-1000μm were found to be promising. The LE and HE spectra for the single-layer detector were found to be optimal at $\sim$ 33kVp and $\sim$ 50kVp, respectively, depending on the anode, detector thickness, and filter material. A conversion layer thickness of 600-1000μm was found to be promising. The difference in performance of the multilayer and single layer detectors varied depending on the conditions (e.g. dose, tumor size, and contrast agent concentration). The multilayer detector had lessened contrast due to poorer spectral separation (overlap of LE and HE spectra). Also, since it was not possible to independently control the multilayer LE and HE spectra, the beam intensities were not optimal and the HE image suffered from significant quantum

noise. Using a 2.5mm radius tumor with 1.5mg/ml contrast agent concentration and 1.42mGy mean glandular dose as a point of reference, the single-layer detector was found to have a detectability 2.4 times that of the multilayer detector.

In the experimental study, prototype single-pixel single-layer and multilayer detectors were tested and the experimental results were used to validate the models. The spectra was optimized based on the available x-ray unit, filters, and detector thicknesses. The contrast of an iodinated contrast agent in the presence of a breast phantom was measured. Good agreement was found between the experimental results and theoretical models.

In the motion artifact study, a model was presented to take into account the effect of motion in CEM image noise and performance. Clinical images were used for model verification and good agreement was found between the models and clinical images. Three types of motion were considered to estimate the effect of motion on performance. It was found that in the presence of motion, the detectability may be reduced to less than half of the motion-absent detectability (2.5mm radius tumor with 3mg/ml contrast agent concentration and 1.42mGy mean glandular dose). The degraded performance, due to motion artifacts, of the single-layer detector is comparable to the performance of the multilayer detector.

In the noise reduction study, a model was presented that takes the anatomical noise into account when evaluating noise reduction techniques. Clinical images were used for model verification and good agreement was found. It was found that including the anatomical noise in the analysis is essential for accurate estimation of the impact of noise reduction techniques on dual-energy image noise. Image noise reduction was found to be beneficial for both the single-layer and multilayer detectors using an anti-correlated noise technique, though the improvements were found to be minor (< 12 percent improvement in detectability for both detectors). From the results, it is not expected that either detector will benefit more greatly than the other from noise reduction techniques.

In summary, this thesis outlines the methodology and presents the tools for dual-energy system design and image combination evaluation, whether it be a single-layer detector or multilayer detector. A method to include the effect of motion in dual-exposure single-layer detector noise and performance analysis is also presented. The models presented were validated using experimental results of prototype detectors and clinical dual-energy images.

9.2 Conclusions

A multilayer energy discriminating detector was investigated to improve the performance of dual-energy imaging, specifically aimed at CEM. Although it is known that the spectral overlap in a multilayer detector degrades the performance compared to that of a single-layer detector, the benefit of the multilayer detector is the simultaneous acquisition of the LE and HE exposures, which eliminates motion artifacts. From the analysis in the thesis and under the described assumptions and model limitations, it was found that the degradation of the multilayer detector performance (i.e., tumor detection) due to spectral overlap and quantum noise was comparable to the degradation of performance due to motion artifacts that may be expected in CEM. Therefore, no significant benefit of using the multilayer detector was found. To reduce the effect of quantum noise on the multilayer detector performance, noise reduction techniques were investigated however no significant performance improvement was found. It may be possible to reduce the effect of spectral overlap using a similar technique as that proposed by Alvarez [89] however this method would require two rapid exposures in succession and corresponding readout and biasing or erasing scheme.

9.3 Future considerations

The proposed multilayer detector was used in the conventional, single projection view methodology. Though it was not investigated, the multilayer detector could also be used for contrast-enhanced tomosynthesis where multiple projection views are taken to obtain a three-dimensional image. The detector could be used as is, similar to how conventional mammography detectors are used for tomosynthesis. However, since there is an increased number of images with tomosynthesis, the dose per image is lower than a conventional mammogram, and thus (detector) noise is problematic. This is especially true for contrast enhanced tomosynthesis since for each projection view, two images must be taken (one for the LE image and another for the HE image), meaning the number of images is doubled compared to that of conventional tomosynthesis. Contrast enhanced tomosynthesis has been investigated by several groups using the dual-energy temporal subtraction methods with a single-layer detector [127, 69, 155]. Another important point that should be considered is how to use the multilayer detector in standard mammography mode. Since there are two detecting layers, it is possible that the signals be added (or some other optimized combination), or used separately for viewing.

The models presented could be extended in several ways. The observer used in the

performance analysis was the ideal observer, which takes into account the information from all frequencies of the signal and noise. Human observers have limitations and some of these limitations could included in the analysis by using observers models that more closely models the human observer, e.g. non-prewhitening observer [156]. Another extension could be the inclusion of scatter in the analysis. In the current model it was assumed that the scatter grid effectively eliminated all scatter radiation. If however the detector were to be used for tomosynthesis, the system may not be equipped with a scatter grid (to avoid attenuating x-rays coming from source that is titled at an angle). The cascaded system model could be extended to include the low frequency effect of scatter [123, 157, 158]. From a noise reduction standpoint, the generalized noise reduction form [21] may be used to optimize performance, as only simple smoothing of the HE image and anti-correlated noise reduction techniques were tested.

Although the large area flat panel multilayer detector was tailored to target K-edge imaging, it could also be applied to other dual-energy applications (e.g. dual-energy chest imaging, dual-energy microcalcification imaging [38, 37], dual-energy bone density quantification [159], and dual-energy breast density quantification [160]), especially those requiring minimized motion artifacts for large area images. Aside from the multilayer detector, the models presented could also be applied to other dual-energy or dual-exposure applications. The motion artifact models could be applied to temporal subtraction where the magnitude of the motion artifacts is expected to be greater due to the larger inter-exposure time.

References

[1] "American Cancer Society. Breast cancer facts and figures 2009-2010. Atlanta, Ga: American Cancer Society," 2010. 1

[2] M. A. Helvie, "Digital mammography imaging: Breast tomosynthesis and advanced applications," *Radiologic Clinics of North America*, vol. 48, pp. 917 – 929, Sept. 2010. 2

[3] J. Boone, A. Kwan, K. Yang, G. Burkett, K. Lindfors, and T. Nelson, "Computed tomography for imaging the breast," *Journal of Mammary Gland Biology and Neoplasia*, vol. 11, pp. 103–111, Apr. 2006. 2

[4] Y. Wu, S. L. Bowen, K. Yang, N. Packard, L. Fu, G. B. Jr, J. Qi, J. M. Boone, S. R. Cherry, and R. D. Badawi, "PET characteristics of a dedicated breast PET/CT scanner prototype," *Physics in Medicine and Biology*, vol. 54, pp. 4273–4287, July 2009. 2

[5] C. Dromain, F. Thibault, F. Diekmann, E. Fallenberg, R. Jong, M. Koomen, R. E. Hendrick, A. Tardivon, and A. Toledano, "Dual-energy contrast-enhanced digital mammography: initial clinical results of a multireader, multicase study," *Breast Cancer Research*, vol. 14, no. 3, p. R94, 2012. 2, 4

[6] E. D. Pisano and M. J. Yaffe, "Digital mammography," *Radiology*, vol. 234, pp. 253–262, Feb. 2005. 3, 4, 23

[7] R. E. Alvarez and A. Macovski, "Energy-selective reconstructions in X-ray computerised tomography," *Physics in Medicine and Biology*, vol. 21, pp. 733–744, Sept. 1976. 3, 16

[8] G. T. Barnes, R. A. Sones, M. M. Tesic, D. R. Morgan, and J. N. Sanders, "Detector for dual-energy digital radiography," *Radiology*, vol. 156, pp. 537–540, Aug. 1985. 3, 26

[9] K. Herrlin, C. Tillman, M. Grätz, C. Olsson, H. Pettersson, G. Svahn, C.-G. Wahlström, and S. Svanberg, "Contrast-enhanced radiography by differential absorption, using a laser-produced x-ray source," *Investigative Radiology*, vol. 32, pp. 306–310, May 1997. 3

[10] R. A. Jong, M. J. Yaffe, M. Skarpathiotakis, R. S. Shumak, N. M. Danjoux, A. Gunesekara, and D. B. Plewes, "Contrast-enhanced digital mammography: Initial clinical experience," *Radiology*, vol. 228, pp. 842–850, Sept. 2003. 3, 22, 88, 99, 107

[11] J. M. Lewin, P. K. Isaacs, V. Vance, and F. J. Larke, "Dual-energy contrast-enhanced digital subtraction mammography: Feasibility," *Radiology*, vol. 229, pp. 261–268, Oct. 2003. 3, 4, 23, 61, 82, 89, 98, 110, 112

[12] S. C. Chen, A.-K. Carton, M. Albert, E. F. Conant, M. D. Schnall, and A. D. A. Maidment, "Initial clinical experience with contrast-enhanced digital breast tomosynthesis," *Academic Radiology*, vol. 14, pp. 229–238, Feb. 2007. 3, 22

[13] I. Rosado-Méndez, B. A. Palma, and M. E. Brandan, "Analytical optimization of digital subtraction mammography with contrast medium using a commercial unit," *Medical Physics*, vol. 35, pp. 5544–5557, Dec. 2008. 3, 22

[14] M. Saito, "Dual-energy approach to contrast-enhanced mammography using the balanced filter method: Spectral optimization and preliminary phantom measurement," *Medical Physics*, vol. 34, pp. 4236–4246, Nov. 2007. 3, 24

[15] N. Allec and K. S. Karim, "A balanced filterless K-edge energy window multilayer detector for dual energy computed tomography," *Proceedings SPIE*, vol. 7622, p. 76224, Feb. 2010. 3, 29

[16] H. Bornefalk, J. M. Lewin, M. Danielsson, and M. Lundqvist, "Single-shot dual-energy subtraction mammography with electronic spectrum splitting: Feasibility," *European Journal of Radiology*, vol. 60, pp. 275 – 278, Nov. 2006. 3, 4, 78

[17] A.-K. Carton, C. Ullberg, K. Lindman, R. Acciavatti, T. Francke, and A. D. A. Maidment, "Optimization of a dual-energy contrast-enhanced technique for a photon-counting digital breast tomosynthesis system: I. A theoretical model," *Medical Physics*, vol. 37, pp. 5896–5907, Nov. 2010. 3, 24, 25, 75, 76, 107

[18] M. Marziani, A. Taibi, A. Tuffanelli, and M. Gambaccini, "Dual-energy tissue cancellation in mammography with quasi-monochromatic x-rays," *Physics in Medicine and Biology*, vol. 47, pp. 305–313, Jan. 2002. 3

[19] L. A. Lehmann, R. E. Alvarez, A. Macovski, W. R. Brody, N. J. Pelc, S. J. Riederer, and A. L. Hall, "Generalized image combinations in dual kVp digital radiography," *Medical Physics*, vol. 8, pp. 659–667, Sept. 1981. 3, 16

[20] S. Puong, X. Bouchevreau, F. Patoureaux, R. Iordache, and S. Muller, "Dual-energy contrast enhanced digital mammography using a new approach for breast tissue canceling," *Proceedings SPIE*, vol. 6510, p. 65102H, Feb. 2007. 3, 16, 75

[21] S. Richard and J. H. Siewerdsen, "Cascaded systems analysis of noise reduction algorithms in dual-energy imaging," *Medical Physics*, vol. 35, pp. 586–601, Feb. 2008. 3, 16, 53, 59, 91, 92, 109, 110, 111, 115, 117, 123

[22] E. Fredenberg, M. Hemmendorff, B. Cederström, M. Aslund, and M. Danielsson, "Contrast-enhanced spectral mammography with a photon-counting detector," *Medical Physics*, vol. 37, pp. 2017–2029, May 2010. 3, 16, 37, 54, 57, 58, 59, 76, 78, 81, 90, 93, 97, 107, 110

[23] C. Dromain, C. Balleyguier, G. Adler, J. R. Garbay, and S. Delaloge, "Contrast-enhanced digital mammography," *European Journal of Radiology*, vol. 69, pp. 34–42, Jan. 2009. 4, 22, 23

[24] L. T. Niklason, D. B. Kopans, and L. M. Hamberg, "Digital breast imaging: tomosynthesis and digital subtraction mammography," *Breast Disease*, vol. 10, no. 3,4, pp. 151–164, 1998. 4

[25] C. D. Arvanitis and R. Speller, "Quantitative contrast-enhanced mammography for contrast medium kinetics studies," *Physics in Medicine and Biology*, vol. 54, pp. 6041–6064, Oct. 2009. 4

[26] D. Gur, L. P. Wallace, A. H. Klym, L. A. Hardesty, G. S. Abrams, R. Shah, and J. H. Sumkin, "Trends in recall, biopsy, and positive biopsy rates for screening mammography in an academic practice1," *Radiology*, vol. 235, pp. 396–401, May 2005. 4

[27] N. D. Prionas, K. K. Lindfors, S. Ray, S.-Y. Huang, L. A. Beckett, W. L. Monsky, and J. M. Boone, "Contrast-enhanced Dedicated Breast CT: Initial Clinical Experience," *Radiology*, vol. 256, pp. 714–723, Sept. 2010. 4

[28] M. Skarpathiotakis, M. J. Yaffe, A. K. Bloomquist, D. Rico, S. Muller, A. Rick, and F. Jeunehomme, "Development of contrast digital mammography," *Medical Physics*, vol. 29, pp. 2419–2426, Oct. 2002. 4, 22

[29] A.-K. Carton, S. C. Gavenonis, J. A. Currivan, E. F. Conant, M. D. Schnall, and A. D. A. Maidment, "Dual-energy contrast-enhanced digital breast tomosynthesis a feasibility study," *British Journal of Radiology*, vol. 83, pp. 344–350, Apr. 2010. 4

[30] A. Karellas and S. Vedantham, "Breast cancer imaging: A perspective for the next decade," *Medical Physics*, vol. 35, pp. 4878–4897, Nov. 2008. 4, 21

[31] S. Richard and J. H. Siewerdsen, "Optimization of dual-energy imaging systems using generalized NEQ and imaging task," *Medical Physics*, vol. 34, pp. 127–139, Jan. 2007. 4, 29, 58, 88

[32] B. J. Heismann, S. Wirth, S. Janssen, and Q. Spreiter, "Technology and image results of a spectral CT system," *Proceedings SPIE*, vol. 5368, pp. 52–59, Feb. 2004. 4, 29, 31

[33] R. Carmi, G. Naveh, and A. Altman, "Material separation with dual-layer CT," *Nuclear Science Symposium Conference Record, IEEE*, vol. 4, pp. 1876–1878, Oct. 2005. 4, 29

[34] D. M. Gauntt and G. T. Barnes, "X-ray tube potential, filtration, and detector considerations in dual-energy chest radiography," *Medical Physics*, vol. 21, pp. 203–218, Feb. 1994. 4, 28, 31

[35] R. D. R. Macdonald, "Design and implementation of a dual-energy x-ray imaging system for organic material detection in an airport security application," in *Proceedings SPIE*, vol. 4301, pp. 31–41, Jan. 2001. 4, 29

[36] H. Fujita, S. Morimi, M. Yamaguchi, H. Fukuda, and K. Murase, "Effectiveness of the single-shot dual-energy subtraction technique for portal images," *Journal of Applied Clinical Medical Physics*, vol. 12, no. 4, pp. 24–33, 2011. 4

[37] J. M. Boone, G. S. Shaber, and M. Tecotzky, "Dual-energy mammography: A detector analysis," *Medical Physics*, vol. 17, pp. 665–675, July 1990. 4, 27, 62, 63, 123

[38] D. P. Chakraborty and G. T. Barnes, "An energy sensitive cassette for dual-energy mammography," *Medical Physics*, vol. 16, pp. 7–13, Jan. 1989. 4, 27, 123

[39] H. E. Johns and J. R. Cunningham, *The Physics of Radiology*. Thomas, Springfield, IL, Fourth ed., 1983. 6, 10, 51

[40] "NIST X-ray Transition Energies Database." `http://www.nist.gov/physlab/data/xraytrans/index.cfm`. 7

[41] K. Cranley, B. J. Gilmore, G. W. A. Fogarty, and L. Desponds, "Catalogue of diagnostic x-ray spectra and other data," Sept. 1997. IPEM Report No. 78, York. x, 9

[42] L. Storm and H. I. Israel, "Photon cross sections from 1 keV to 100 MeV for elements Z=1 to Z=100," *Atomic Data and Nuclear Data Tables*, vol. 7, pp. 565–681, June 1970. ix, 10, 41

[43] F. Salvat, J. Fernandez-Varea, and J. Sempau, "PENELOPE-2006: A code system for Monte Carlo simulation of electron and photon transport," in *Workshop proceedings, Organisation for economic co-operation and development*, July 2006. ix, x, xi, 11, 13, 22, 51, 52

[44] S. Vedantham, A. Karellas, S. Suryanarayanan, D. Albagli, S. Han, E. J. Tkaczyk, C. E. Landberg, B. Opsahl-Ong, P. R. Granfors, I. Levis, C. J. D'Orsi, and R. E. Hendrick, "Full breast digital mammography with an amorphous silicon-based flat panel detector: Physical characteristics of a clinical prototype," *Medical Physics*, vol. 27, pp. 558–567, Mar. 2000. 12

[45] N. Allec, A. H. Goldan, K. Wang, F. Chen, and K. S. Karim, "Amorphous silicon p-i-n photodetector with frisch grid for high-speed medical imaging," *Proceedings SPIE*, vol. 7622, p. 76223X, Feb. 2010. 12

[46] S. Suryanarayanan, A. Karellas, S. Vedantham, and S. K. Onishi, "High-resolution imager for digital mammography: physical characterization of a prototype sensor," *Physics in Medicine and Biology*, vol. 50, pp. 3957–3969, Sept. 2005. 12

[47] S. Abbaszadeh, N. Allec, K. Wang, and K. S. Karim, "Low dark-current lateral amorphous-selenium metal-semiconductor-metal photodetector," *Electron Device Letters, IEEE*, vol. 32, pp. 1263–1265, Sept. 2011. 12

[48] S. Abbaszadeh, S. H. Majid, N. Allec, and K. S. Karim, "Amorphous selenium photodetector on a flexible substrate for indirect conversion medical imaging," *Proceedings SPIE*, vol. 8313, p. 83135X, Feb. 2012. 12

[49] S. Abbaszadeh, N. Allec, S. Ghanbarzadeh, U. Shafique, and K. S. Karim, "Investigation of hole-blocking contacts for high-conversion-gain amorphous selenium detectors

for x-ray imaging," *Transactions on Electron Devices, IEEE*, vol. 59, pp. 2403–2409, Sept. 2012. 12, 33

[50] F. Chen, K. Wang, Y. Fang, N. Allec, G. Belev, S. Kasap, and K. S. Karim, "Direct-conversion x-ray detector using lateral amorphous selenium structure," *Sensors Journal, IEEE*, vol. 11, pp. 505–509, Feb. 2011. 12

[51] K. Wang, F. Chen, N. Allec, F. Yuan, G. Belev, S. Kasap, and K. S. Karim, "Amorphous-selenium-based three-terminal x-ray detector with a gate," *Electron Device Letters, IEEE*, vol. 32, pp. 782–784, June 2011. 12

[52] M. Z. Kabir, *Modeling of X-ray photoconductors for X-ray image detectors*. PhD thesis, Dept. of Electrical Engineering, University of Saskatchewan, Aug. 2005. ix, 13

[53] M. Lundqvist, B. Cederstrom, V. Chmill, M. Danielsson, and B. Hasegawa, "Evaluation of a photon-counting x-ray imaging system," *Transactions on Nuclear Science, IEEE*, vol. 48, pp. 1530 –1536, Aug. 2001. 14, 15

[54] K.-W. Shin, K. Wang, N. Allec, Y. Fang, and K. S. Karim, "Novel silicon x-ray detector with tft readout," *Proceedings SPIE*, vol. 8313, p. 83135R, Feb. 2012. 14

[55] N. Safavian, M. Yazdandoost, D. Wu, M. H. Izadi, K. S. Karim, and J. A. Rowlands, "Investigation of gain non-uniformities in the two tft current programmed amorphous silicon active pixel sensor for fluoroscopy, chest radiography, and mammography tomosynthesis applications," *Proceedings SPIE*, vol. 7622, p. 76221N, Feb. 2010. 14

[56] K. S. Karim, *Pixel architectures for digital imaging using amorphous silicon technology*. PhD thesis, Dept. of Electrical and Computer Engineering, University of Waterloo, 2002. x, 15

[57] S. N. Ahmed, *Physics & Engineering of Radiation Detection*. Academic Press Inc., London, 2007. x, 15

[58] B. Jacobson, "Dichromatic absorption radiography. dichromography," *Acta Radiologica*, vol. 39, no. 6, pp. 437–452, 1953. 16

[59] H. Bornefalk, *Computer-aided Detection and Novel Mammography Imaging Techniques*. PhD thesis, Dept. of Physics, Royal Institute of Technology, Stockholm, Sweden, Mar. 2006. 17, 24, 61, 75

[60] J. C. Dainty and R. Shaw, *Image Science: Principles, Analysis and Evaluation of Photographic-Type Imaging Processes*. Academic Press Inc., New York, New York, 1974. 17, 91

[61] J. Beutel, H. Kundel, and R. V. Metter, *Handbook of Medical Imaging: Physics and Psychophysics*. SPIE Press, 2000. 17

[62] H. H. Barrett and K. J. Myers, *Foundations of Image Science*. John Wiley & Sons, Inc., Hoboken, New Jersey, 2004. 17, 90, 92

[63] J. T. Bushberg, J. A. Seibert, E. M. Leidholdt, and J. M. Boone, *The Essential Physics of Medical Imaging*. Lippincott Williams & Wilkins, Third ed., 2012. 17

[64] R. M. Nishikawa, "The fundamentals of MTF, Wiener spectra, and DQE," *41st Annual Meeting of the American Association of Physicists in Medicine*, 1999. x, 18

[65] "7. Measurement of image quality in mammography," *Journal of the ICRU*, vol. 9, pp. 65–75, Dec. 2009. 19

[66] J. Yao and H. H. Barrett, "Predicting human performance by a channelized hotelling observer model," *Proceedings SPIE*, vol. 1768, pp. 161–168, July 1992. 19

[67] J. M. Boone, "Glandular breast dose for monoenergetic and high-energy x-ray beams: Monte Carlo assessment," *Radiology*, vol. 213, pp. 23–37, Oct. 1999. xi, 22, 51

[68] M. J. Berger, J. H. Hubbell, S. M. Seltzer, J. Chang, J. S. Coursey, R. Sukumar, and D. S. Zucker, "XCOM: Photon Cross Section Database (version 1.4)," 2009. National Institute of Standards and Technology, Gaithersburg, MD. xi, 22

[69] A.-K. Carton, J. Li, M. Albert, S. Chen, and A. D. A. Maidment, "Quantification for contrast-enhanced digital breast tomosynthesis," *Proceedings SPIE*, vol. 6142, p. 61420D, Feb. 2006. 22, 52, 88, 99, 108, 122

[70] P. A. Ross, "A new method of spectroscopy for faint X-radiations," *Journal of the Optical Society of America*, vol. 16, pp. 433–436, Nov. 1928. 23, 29

[71] M. Varjonen, *Three-dimensional (3D) digital breast tomosynthesis (DBT) in the early diagnosis and detection of breast cancer*. PhD thesis, Tampere University of Technology publications 594, May 2006. 24, 88

[72] A. K. Bloomquist, M. J. Yaffe, G. E. Mawdsley, D. M. Hunter, and D. J. Beideck, "Lag and ghosting in a clinical flat-panel selenium digital mammography system," *Medical Physics*, vol. 33, pp. 2998–3005, Aug. 2006. 24

[73] E. Fredenberg, *Spectral Mammography with X-ray Optics and a Photon-Counting Detector*. PhD thesis, Royal Institute of Technology (KTH), Stockholm, Sweden, Dec. 2009. 24

[74] H. Bornefalk, M. Hemmendorff, and T. Hjärn, "Contrast-enhanced dual-energy mammography using a scanned multislit system: evaluation of a differential beam filtering technique," *Journal of Electronic Imaging*, vol. 16, p. 023006, Apr. 2007. 24

[75] M. J. Yaffe, "Digital mammography–detector considerations and new applications," *Nuclear Instruments and Methods in Physics Research Section A: Accelerators, Spectrometers, Detectors and Associated Equipment*, vol. 471, pp. 6–11, Sept. 2001. 25, 76

[76] R. E. Alvarez and A. Macovski, "X-ray spectral decomposition imaging system," 1977. U.S. Patent 4 029 963. 26

[77] R. A. Brooks and G. D. Chiro, "Split-detector computed tomography: A preliminary report," *Radiology*, vol. 126, pp. 255–257, Jan. 1978. 26

[78] D. J. Drost and A. Fenster, "Experimental dual xenon detectors for quantitative CT and spectral artifact correction," *Medical Physics*, vol. 7, pp. 101–107, Mar. 1980. 26

[79] D. R. Morgan, R. A. Sones, and G. T. Barnes, "Performance characteristics of a dual-energy detector for digital scan projection radiography," *Medical Physics*, vol. 14, pp. 728–735, Sept. 1987. 26

[80] H. Takeuchi, K.-S. Chuang, and H. K. Huang, "Dual energy imaging in projection radiography," *Proceedings SPIE*, vol. 626, pp. 39–48, June 1986. 27

[81] T. Ishigaki, S. Sakuma, Y. Horikawa, M. Ikeda, and H. Yamaguchi, "One-shot dual-energy subtraction imaging.," *Radiology*, vol. 161, pp. 271–273, Oct. 1986. 27

[82] T. Ishigaki, S. Sakuma, and M. Ikeda, "One-shot dual-energy subtraction chest imaging with computed radiography: clinical evaluation of film images.," *Radiology*, vol. 168, pp. 67–72, July 1988. 27

[83] R. A. Sones and G. T. Barnes, "Noise correlations in images acquired simultaneously with a dual-energy sandwich detector," *Medical Physics*, vol. 16, pp. 858–861, Nov. 1989. 27

[84] J.-T. Ho, R. A. Kruger, and J. A. Sorenson, "Comparison of dual and single exposure techniques in dual-energy chest radiography," *Medical Physics*, vol. 16, pp. 202–208, Mar. 1989. 27

[85] M. Ohki, "Single exposure dual energy imaging in intra-oral radiography," *Oral Radiology*, vol. 7, pp. 31–40, Dec. 1991. 28, 62

[86] D. L. Ergun, C. A. Mistretta, D. E. Brown, R. T. Bystrianyk, W. K. Sze, F. Kelcz, and D. P. Naidich, "Single-exposure dual-energy computed radiography: improved detection and processing.," *Radiology*, vol. 174, pp. 243–249, Jan. 1990. 28

[87] F. Kelcz, F. E. Zink, W. W. Peppler, D. G. Kruger, D. L. Ergun, and C. A. Mistretta, "Conventional chest radiography vs dual-energy computed radiography in the detection and characterization of pulmonary nodules," *American Journal of Roentgenology*, vol. 162, pp. 271–8, Feb. 1994. 28

[88] B. K. Stewart and H. K. Huang, "Single-exposure dual-energy computed radiography," *Medical Physics*, vol. 17, pp. 866–875, Sept. 1990. 28, 62, 77

[89] R. E. Alvarez, "Active energy selective image detector for dual-energy computed radiography," *Medical Physics*, vol. 23, pp. 1739–1748, Oct. 1996. 28, 122

[90] S. Kappler, M. Grasruck, D. Niederlöhner, M. Strassburg, and S. Wirth, "Dual-energy performance of dual kVp in comparison to dual-layer and quantum-counting CT system concepts," in *Proceedings SPIE*, vol. 7258, p. 725842, Feb. 2009. 29

[91] S. Kappler and S. Wirth, "Comparison of dual-kvp and dual-layer ct in simulations and real ct system measurements," in *Nuclear Science Symposium Conference Record, 2008. NSS '08. IEEE*, pp. 4828–4831, Oct. 2008. 29

[92] K. H. Kim, I. S. Jun, and Y. S. Eun, "New sandwich type detector module and its characteristics for dual x-ray baggage inspection system," in *Nuclear Science Symposium Conference Record, 2007. NSS '07. IEEE*, vol. 2, pp. 1191–1194, Oct. 2007. 29

[93] D. S. Rigie, D. Modgil, P. Vargas, S. Wang, and P. J. La Riviere, "Basis element decomposition with spectral microct using multi-layered, multi-colored scintillators,"

in *Nuclear Science Symposium Conference Record, 2012. NSS '12. IEEE*, Nov. 2012. 30

[94] L. Li, P. Jiao, Z. Chen, and L. Zhang, "Dual-energy ct reconstruction based on dictionary learning and total variation constraint," in *Nuclear Science Symposium Conference Record, 2012. NSS '12. IEEE*, Nov. 2012. 30

[95] S. Abbaszadeh, K. Rom, O. Bubon, B. A. Weinstein, K. S. Karim, J. A. Rowlands, and A. Reznik, "The effect of the substrate on transient photodarkening in stabilized amorphous selenium," *Journal of Non-Crystalline Solids*, vol. 358, pp. 2389–2392, Sept. 2012. 33

[96] S. Richard, J. H. Siewerdsen, D. A. Jaffray, D. J. Moseley, and B. Bakhtiar, "Generalized DQE analysis of radiographic and dual-energy imaging using flat-panel detectors," *Medical Physics*, vol. 32, pp. 1397–1413, May 2005. 34, 89, 90

[97] A. E. Burgess, "Bach, breasts, and power-law processes," *Proceedings SPIE*, vol. 4324, pp. 103–113, Feb. 2001. 37, 59

[98] A. E. Burgess, F. L. Jacobson, and P. F. Judy, "Human observer detection experiments with mammograms and power-law noise," *Medical Physics*, vol. 28, pp. 419–437, Apr. 2001. 37, 59, 60, 61, 112

[99] I. A. Cunningham, *Handbook of Medical Imaging: Physics and Psychophysics*. SPIE Press, 2000. ch.2: Applied Linear-Systems Theory. 38

[100] Y. Fang, A. Badal, N. Allec, K. S. Karim, and A. Badano, "Monte carlo simulation of amorphous selenium imaging detectors," *Proceedings SPIE*, vol. 7622, p. 762214, Feb. 2010. 38

[101] Y. Fang, A. Badal, N. Allec, K. S. Karim, and A. Badano, "Spatiotemporal monte carlo transport methods in x-ray semiconductor detectors: Application to pulse-height spectroscopy in a-Se," *Medical Physics*, vol. 39, no. 1, pp. 308–319, 2012. 38

[102] M. Z. Kabir, M. W. Rahman, and W. Y. Shen, "Modelling of detective quantum efficiency of direct conversion x-ray imaging detectors incorporating charge carrier trapping and k-fluorescence," *IET Circuits, Devices & Systems*, vol. 5, pp. 222–231, May 2011. 38

[103] M. Rabbani, R. Shaw, and R. V. Metter, "Detective quantum efficiency of imaging systems with amplifying and scattering mechanisms," *Journal of the Optical Society of America A*, vol. 4, pp. 895–901, May 1987. 38, 39

[104] W. Zhao, W. G. Ji, and J. A. Rowlands, "Effects of characteristic x rays on the noise power spectra and detective quantum efficiency of photoconductive x-ray detectors," *Medical Physics*, vol. 28, pp. 2039–2049, Oct. 2001. ix, 41, 48

[105] M. Z. Kabir and S. O. Kasap, "DQE of photoconductive x-ray image detectors: application to a-Se," *Journal of Physics D: Applied Physics*, vol. 35, pp. 2735–2743, Nov. 2002. ix, 40, 41, 44, 45, 46

[106] I. M. Blevis, D. C. Hunt, and J. A. Rowlands, "Measurement of x-ray photogeneration in amorphous selenium," *Journal of Applied Physics*, vol. 85, pp. 7958–7963, June 1999. 41

[107] M. Yunus, "Monte Carlo modeling of the sensitivity of X-ray photoconductors," Master's thesis, Dept. of Electrical Engineering, University of Saskatchewan, Apr. 2005. 41

[108] D. R. Dance and G. J. Day, "Escape probabilities for fluorescent x-rays," *Physics in Medicine and Biology*, vol. 30, pp. 259–262, Mar. 1985. 42

[109] W. Zhao and J. A. Rowlands, "Digital radiology using active matrix readout of amorphous selenium: Theoretical analysis of detective quantum efficiency," *Medical Physics*, vol. 24, pp. 1819–1833, Dec. 1997. 42

[110] R. Fahrig, J. A. Rowlands, and M. J. Yaffe, "X-ray imaging with amorphous selenium: Detective quantum efficiency of photoconductive receptors for digital mammography," *Medical Physics*, vol. 22, pp. 153–160, Feb. 1995. 42, 43

[111] G. F. Knoll, *Radiation Detection and Measurement*. John Wiley & Sons, Toronto, 1979. 43

[112] H.-P. Chan and K. Doi, "Energy and angular dependence of x-ray absorption and its effect on radiographic response in screen-film systems," *Physics in Medicine and Biology*, vol. 28, pp. 565–579, May 1983. 48, 49

[113] W. Que and J. A. Rowlands, "X-ray imaging using amorphous selenium: Inherent spatial resolution," *Medical Physics*, vol. 22, pp. 365–374, Apr. 1995. 48

[114] D. R. Dance, "Monte-Carlo calculation of conversion factors for the estimation of mean glandular breast dose," *Physics in Medicine and Biology*, vol. 35, no. 9, pp. 1211–1219, 1990. 51

[115] S. C. Thacker and S. J. Glick, "Normalized glandular dose (DgN) coefficients for flat-panel CT breast imaging," *Physics in Medicine and Biology*, vol. 49, pp. 5433–5444, Dec. 2004. xi, 51

[116] G. R. Hammerstein, D. W. Miller, D. R. White, M. E. Masterson, H. Q. Woodard, and J. S. Laughlin, "Absorbed radiation dose in mammography," *Radiology*, vol. 130, pp. 485–491, Feb. 1979. 52

[117] J. M. Boone, T. R. Fewell, and R. J. Jennings, "Molybdenum, rhodium, and tungsten anode spectral models using interpolating polynomials with application to mammography," *Medical Physics*, vol. 24, pp. 1863–1874, Dec. 1997. 52

[118] D. M. Tucker, G. T. Barnes, and X. Wu, "Molybdenum target x-ray spectra: A semiempirical model," *Medical Physics*, vol. 18, pp. 402–407, May 1991. 52

[119] D. M. Tucker, G. T. Barnes, and D. P. Chakraborty, "Semiempirical model for generating tungsten target x-ray spectra," *Medical Physics*, vol. 18, pp. 211–218, Mar. 1991. 52

[120] M. J. Flynn, C. Dodge, D. J. Peck, and A. Swinford, "Optimal radiographic techniques for digital mammograms obtained with an amorphous selenium detector," *Proceedings SPIE*, vol. 5030, pp. 147–156, Feb. 2003. 52, 53, 63

[121] M. A. Kafi, N. Maalej, and A. Naqvi, "Scatter dose calculation for anti-scatter linear grids in mammography," *Applied Radiation and Isotopes*, vol. 67, pp. 1837 – 1841, Oct. 2009. 53

[122] P. S. Rezentes, A. de Almeida, and G. T. Barnes, "Mammography grid performance," *Radiology*, vol. 210, no. 1, pp. 227–232, 1999. 53

[123] I. S. Kyprianou, S. Rudin, D. R. Bednarek, and K. R. Hoffmann, "Generalizing the MTF and DQE to include x-ray scatter and focal spot unsharpness: Application to a new microangiographic system," *Medical Physics*, vol. 32, pp. 613–626, Feb. 2005. 53, 123

[124] E. Fredenberg, M. Lundqvist, M. A. slund, M. Hemmendorff, B. Cederström, and M. Danielsson, "A photon-counting detector for dual-energy breast tomosynthesis," *Proceedings SPIE*, vol. 7258, p. 72581J, Feb. 2009. 53

[125] M. Danielsson, H. Bornefalk, B. Cederstroem, V. Chmill, B. H. Hasegawa, M. Lundqvist, D. R. Nygren, and T. Tabar, "Dose-efficient system for digital mammography," *Proceedings SPIE*, vol. 3977, pp. 239–249, Feb. 2000. 55

[126] S. Richard, *Optimization of imaging performance and conspicuity in dual-energy x-ray radiography.* PhD thesis, University of Toronto, Toronto, Canada, 2008. 58

[127] S. Puong, X. Bouchevreau, N. Duchateau, R. Iordache, and S. Muller, "Optimization of beam parameters and iodine quantification in dual-energy contrast enhanced digital breast tomosynthesis," *Proceedings SPIE*, vol. 6913, p. 69130Z, Feb. 2008. 75, 122

[128] P. Grybos, *Circuits at the Nanoscale: Communications, Imaging, Sensing.* CRC Press, 2008. ch.30: Detector interface circuits for x-ray imaging. 76

[129] S. Kasap, J. B. Frey, G. Belev, O. Tousignant, H. Mani, L. Laperriere, A. Reznik, and J. A. Rowlands, "Amorphous selenium and its alloys from early xeroradiography to high resolution x-ray image detectors and ultrasensitive imaging tubes," *Physica Status Solidi (b)*, vol. 246, pp. 1794–1805, Aug. 2009. 78, 82

[130] S. O. Kasap and J. A. Rowlands, "Direct-conversion flat-panel x-ray image detectors," *Circuits, Devices and Systems, IEE Proceedings*, vol. 149, pp. 85–96, Apr. 2002. 78

[131] B. T. Polischuk, P. Leblanc, M. Choquette, Z. A. Shukri, and H. M. Rougeot, "Direct conversion digital x-ray detector with inherent high voltage protection for static and dynamic imaging," Mar. 2002. U.S. Patent 6 353 229. 78

[132] M. L. Hill, J. G. Mainprize, R. A. Jong, and M. J. Yaffe, "Design and validation of a mathematical breast phantom for contrast-enhanced digital mammography," *Proceedings SPIE*, vol. 7961, p. 79615E, Feb. 2011. 88, 98, 99

[133] H. Bornefalk and M. Lundqvist, "Dual-energy imaging using a photon counting detector with electronic spectrum-splitting," *Proceedings SPIE*, vol. 6142, p. 61421H, Feb. 2006. 88, 96

[134] R. E. Alvarez, J. A. Seibert, and S. K. Thompson, "Comparison of dual energy detector system performance," *Medical Physics*, vol. 31, no. 3, pp. 556–565, 2004. 89

[135] E. Fredenberg, B. Svensson, M. Danielsson, B. Lazzari, and B. Cederstrom, "Optimization of mammography with respect to anatomical noise," *Proceedings SPIE*, vol. 7961, no. 1, p. 796112, 2011. 90

[136] P. C. Johns and M. J. Yaffe, "Theoretical optimization of dual-energy x-ray imaging with application to mammography," *Medical Physics*, vol. 12, pp. 289–296, May 1985. 91, 109, 115

[137] K. J. Myers, J. P. Rolland, H. H. Barrett, and R. F. Wagner, "Aperture optimization for emission imaging: effect of a spatially varying background," *Journal of the Optical Society of America A*, vol. 7, pp. 1279–1293, Jul 1990. 91

[138] H. H. Barrett, "Objective assessment of image quality: effects of quantum noise and object variability," *Journal of the Optical Society of America A*, vol. 7, pp. 1266–1278, Jul 1990. 91

[139] A. Papoulis, *Probability, Random Variables, and Stochastic Processes*. McGraw-Hill, New York, 1965. 92, 94

[140] C. E. Metz and K. Doi, "Transfer function analysis of radiographic imaging systems," *Physics in Medicine and Biology*, vol. 24, pp. 1079–1106, Nov. 1979. 92, 94

[141] J. Yao and I. A. Cunningham, "Parallel cascades: New ways to describe noise transfer in medical imaging systems," *Medical Physics*, vol. 28, pp. 2020–2038, Oct. 2001. 94

[142] O. Hadar, I. Dror, and N. S. Kopeika, "Image resolution limits resulting from mechanical vibrations. part iv: real-time numerical calculation of optical transfer functions and experimental verification," *Optical Engineering*, vol. 33, pp. 566–578, Feb. 1994. 95, 96

[143] D. Arbel, O. Hadar, and N. S. Kopeika, "Medical image restoration of dynamic lungs using optical transfer function of lung motion," *Journal of Biomedical Optics*, vol. 6, pp. 193–199, Apr. 2001. 95

[144] Q. Xu, K. Yuan, and D. Ye, "Respiratory motion blur identification and reduction in ungated thoracic PET imaging," *Physics in Medicine and Biology*, vol. 56, pp. 4481–4498, July 2011. 95

[145] J. T. Dobbins, III, E. Samei, N. T. Ranger, and Y. Chen, "Intercomparison of methods for image quality characterization: II. Noise power spectrum," *Medical Physics*, vol. 33, pp. 1466–1475, May 2006. 98

[146] Z. Zhou, F. Gao, H. Zhao, and L. Zhang, "Techniques to improve the accuracy of noise power spectrum measurements in digital x-ray imaging based on background trends removal," *Medical Physics*, vol. 38, pp. 1600–1610, Mar. 2011. 98

[147] D. B. Percival and A. T. Walden, *Spectral Analysis for Physical Applications: Multitaper and Conventional Univariate Techniques*. Cambridge University Press, Cambridge, 1993. 98

[148] M. Albert and A. D. A. Maidment, "Linear response theory for detectors consisting of discrete arrays," *Medical Physics*, vol. 27, pp. 2417–2434, Oct. 2000. 104

[149] J. B. A. Maintz and M. A. Viergever, "A survey of medical image registration," *Medical Image Analysis*, vol. 2, pp. 1–36, Mar. 1998. 108

[150] P. C. Johns and M. J. Yaffe, "X-ray characterisation of normal and neoplastic breast tissues," *Physics in Medicine and Biology*, vol. 32, pp. 675–695, June 1987. 109

[151] S. C. Kappadath and C. C. Shaw, "Dual-energy digital mammography for calcification imaging: noise reduction techniques," *Physics in Medicine and Biology*, vol. 53, pp. 5421–5443, Oct. 2008. 109

[152] R. J. Warp and J. T. Dobbins, "Quantitative evaluation of noise reduction strategies in dual-energy imaging," *Medical Physics*, vol. 30, pp. 190–198, Feb. 2003. 109

[153] W. Kalender, E. Klotz, and L. Kostaridou, "An algorithm for noise suppression in dual energy ct material density images," *Transactions on Medical Imaging, IEEE*, vol. 7, pp. 218–224, Sept. 1988. 109

[154] C. H. McCollough, M. S. V. Lysel, W. W. Peppler, and C. A. Mistretta, "A correlated noise reduction algorithm for dual-energy digital subtraction angiography," *Medical Physics*, vol. 16, pp. 873–880, Nov. 1989. 109, 112

[155] E. Samei and R. S. Saunders Jr, "Dual-energy contrast-enhanced breast tomosynthesis: optimization of beam quality for dose and image quality," *Physics in Medicine and Biology*, vol. 56, pp. 6359–6378, Oct. 2011. 122

[156] H. H. Barrett, J. Yao, J. P. Rolland, and K. J. Myers, "Model observers for assessment of image quality," *Proceedings of the National Academy of Sciences*, vol. 90, pp. 9758–9765, Nov. 1993. 123

[157] C.-G. Shaw and D. B. Plewes, "Effects of scattered radiation and veiling glare in dual-energy tissue–bone imaging: A theoretical analysis," *Medical Physics*, vol. 14, pp. 956–967, Nov. 1987. 123

[158] F. C. Wagner, A. Macovski, and D. C. Nishimura, "Dual-energy x-ray projection imaging: Two sampling schemes for the correction of scattered radiation," *Medical Physics*, vol. 15, pp. 732–748, Sept. 1988. 123

[159] S. Boonen, J. Nijs, H. Borghs, H. Peeters, D. Vanderschueren, and F. P. Luyten, "Identifying postmenopausal women with osteoporosis by calcaneal ultrasound, metacarpal digital x-ray radiogrammetry and phalangeal radiographic absorptiometry: a comparative study," *Osteoporosis International*, vol. 16, pp. 93–100, Jan. 2005. 123

[160] J. L. Ducote and S. Molloi, "Quantification of breast density with dual energy mammography: A simulation study," *Medical Physics*, vol. 35, pp. 5411–5418, Dec. 2008. 123